NUMERICAL AND EXPERIMENTAL STUDY OF PACEMAKER SAFETY UNDER MRI

A Dissertation

Presented to

the Faculty of the Department of Electrical and Computer Engineering

University of Houston

In Partial Fulfillment

of the Requirements for the Degree

Doctor of Philosophy

in Electrical Engineering

by

Shi Feng

December 2014

NUMERICAL AND EXPERIMENTAL STUDY OF PACEMAKER SAFETY UNDER MRI

_____

Shi Feng

Approved:

_____

Chairman of the Committee
Ji Chen, Professor,
Electrical and Computer Engineering

Committee Members:

_____

David Jackson, Professor
Electrical and Computer Engineering

_____

Donald Wilton, Professor Emeritus
Electrical and Computer Engineering

_____

George Zouridakis, Professor
Engineering Technology

_____

Wolfgang Kainz, Senior Principal Scientist
U.S. Food and Drug Administration

_____

Suresh K. Khator, Associate Dean,
Cullen College of Engineering

_____

Badrinath Roysam, Professor and Chairman
Electrical and Computer Engineering

Acknowledgements

I am deeply grateful to my thesis advisor, Dr. Ji Chen, for his continuous research supervision, encouragement, and valuable suggestions. Without his assistance, my research would have been impossible. As advisor, mentor and friend, his influence and guidance will have a lasting effect on my career and my life.

I would like to express my sincere gratitude to the members of my advisory committee: Dr. David Jackson, Dr. Donald Wilton, Dr. George Zouridakis, and Dr. Wolfgang Kainz for their assistance and constructive criticism.

I would like to express gratitude for Dr. Stuart Long, Dr. Ben Jansen, Dr Han Le, Dr. Haluk Ogmen, Dr. Bhavin Sheth, Dr. Zhu Han, and Dr. Pauline Markenscoff for their lectures and instruction.

I would like to thank the research sponsorship from Biotronik and support from the MRI team: Dr. Krishna Kurpad, Dr. Ke Feng, Dr. Rui Qiang, Dr. Paul Stadnik, and Dr. Java Von Arx.

I would like to thank the past and present members of our research group: Dr. Minshen Wang, Dr. Jianxiang Shen, Dr. Zubiao Xiong, Dr Yan Liu, Dr. Cong Gao, Mr. Qingyan Wang, Ms. Xichen Guo, Ms. Qi Zeng, Mr. Lintong Li, Mr. Jingsheng Liu, Dr. Janfeng Zheng, Mr. Xiyao Xin, Mr. Xin Huang, Mr. Dawei Li, Ms. Xinyu Liu, Mr. Yanxiang Yu, and Ms. Mengna Yang for their assistance, encouragement, and support. It has been a great pleasure to work with them.

I would also like to thank Professor Dr. Yu Liu. Without her recommendation, I would not have the opportunity to study at the University of Houston.

Last, but not the least, I would like to thank my parents, Xionghui Feng and Hong Shi, and all other family members for their encouragement and confidence in me. Also I like to thank Uncle James Liu and his family for their help and support.

NUMERICAL AND EXPERIMENTAL STUDY OF PACEMAKER SAFETY UNDER MRI

An Abstract

of a

Dissertation

Presented to

the Faculty of the Department of Electrical and Computer Engineering

University of Houston

In Partial Fulfillment

of the Requirements for the Degree

Doctor of Philosophy

in Electrical Engineering

by

Shi Feng

December 2014

Abstract

Pacemaker safety issues with MRI (Magnetic Resonance Imaging) are discussed in this thesis. In order to analyze the electromagnetic compatibility issue of pacemaker/defibrillator with MRI RF (radio frequency) coil and human body model, novel techniques for the evaluation of MRI-induced heating or induced voltage in the vicinity of implanted metallic lead have been developed based on the reciprocity theorem. The measurement configurations have been described in detail. The technique was validated in both numerical and experimental studies on different lead structures. More than one hundred transfer functions of real practical pacemakers are measured, and hundreds of validation tests were performed on those transfer functions. In addition, the effects of human body/phantom were also discussed based on the measured transfer functions and human body simulations.

This approach allows one to decouple the micro-scale metallic lead simulation/measurement from the macro-level phantom human simulations within the MRI scanners. Consequently, the estimation of MRI-induced heating on an implanted lead, and the induced voltage on the pacemaker device can be greatly simplified. The analysis about the pacemaker safety issue will become very efficient. In addition, this method clearly explains the induced lead heating mechanism during MRI procedures.

Table of Contents

Acknowledgements v

Abstract viii

Table of Contents ix

List of Figures xi

List of Tables xvii

Chapter 1 Introduction 1

Chapter 2 Methodology 4

2.1 Introduction of Pacemaker Transfer Function 4

2.2 Pacemaker EMC Safety Analysis Procedure Using the Transfer function 5

2.3 Transfer Function Estimation Approach 6

2.3.1 Direct Estimation of the Transfer Function 6

2.3.2 Using the Reciprocity Theorem to Estimate the Induced Voltage Transfer Function 8

2.3.3 Using the Reciprocity Theorem to Estimate the Heating Transfer Function 13

2.3.4 Fast Transfer Function Estimation 16

2.4 Numerical Modeling of the MRI RF Coil and Phantom 20

2.5 Measurement Settings 24

2.5.1 Transfer Function Measurement 24

2.5.2 RF Coil and Control System Operation 33

2.5.3 Induced Voltage Measurement 37

2.5.4 Thermal Measurement 40

Chapter 3 Numerical and Experimental Results 43

3.1 Induced Electric Field Transfer Functions of Thin Wire Leads 43

3.2 Induced Voltage Transfer Functions of Coaxial Lead and 4-Wire Lead 51

3.3 Transfer Functions of Practical Pacemaker/Defibrillator Leads 57

3.4 Validation Results of Practical Leads Transfer Functions 64

3.5 Fast Transfer Function Estimation Result 75

Chapter 4 Human Body and Phantom Effect Study 85

4.1 Transfer Function Used in This Study 85

4.2 Incident Electrical Field Along Lead Paths of Three States 87

4.3 Temperature Rise Results and Discussion 93

Chapter 5 Conclusions and Future Work 95

5.1 Conclusion 95

5.2 Future Work 96

References 98

List of Figures

Fig. 2–1 The procedure of voltage/temperature prediction using transfer function. ..5

Fig. 2–2 A localized electrical field added on the lead to directly measure the transfer function. 7

Fig. 2–3 The pacemaker system is modeled by device CAN impedance and two conduct leads. The conduct lead is insulated from the medium except for a short segment at the distal end (the end plugged in human heart muscle). 8

Fig. 2–4 Two sets of sources are applied to the pacemaker system individually. 10

Fig. 2–5 Two sets of new sources are applied to the pacemaker system individually.12

Fig. 2–6 An infinitesimal dipole is added next to the lead distal end as the second excitation to apply the reciprocity.....15

Fig. 2–7 The orthogonalized bases to represent the transfer function. 19

Fig. 2–8 1.5 T MRI RF coil model in SEMCAD. 20

Fig. 2–9 The ASTM phantom dimension in mm. 22

Fig. 2–10 The incident electric field distribution in dB in the vertical center plane. 24

Fig. 2–11 The dimension of the current probe from Pearson electronics. 25

Fig. 2–12 NI PXIe-5360 vector network analyzer with NI PXIe-1082 PXI Express Chassis. 25

Fig. 2–13 The modified device CAN with a SMA connector. 26

Fig. 2–14 Induced voltage transfer function measurement configuration. 26

Fig. 2–15 A simple balun made by coaxial cable and magnetic core. 29

Fig. 2–16 The dipole excitation built by a semi-rigid coaxial cable covered by lossy material. 31

Fig. 2–17 The heating transfer function measurement configuration. 32

Fig. 2–18 The 1.5 T MRI RF coil and the control console. 34

Fig. 2–19 A screen shot from the RF coil control console shows the magnitude and the spectrum of the sinc2 signal envelop. 34

Fig. 2–20 The I/Q feed of the MRI RF coil. 35

Fig. 2–21 The shielding room made by ETS-Lindgren. 35

Fig. 2–22 The easy4 H-field probe. 37

Fig. 2–23 The phantom loaded in the MRI RF coil. 37

Fig. 2–24 A pacemaker device CAN in the phantom is connected through a simple balun. 39

Fig. 2–25 A copper sheet is fixed on a certain place on the RF coil shield. 39

Fig. 2–26 Mixed gelled saline in the rectangular ASTM phantom 40

Fig. 2–27 The thermometer with four channels from Neoptix. 41

Fig. 2–28 A temperature probe is tied to a lead distal end to measure the temperature rise. 42

Fig. 3–1 The measured and simulated transfer functions of a 42 cm thin wire. 45

Fig. 3–2 (a) The relative error of the measured transfer function magnitude and (b) the phase difference between measured and simulated transfer function. 46

Fig. 3–3 The simulated transfer function on the straight thin wire leads for four different lengths. 47

Fig. 3–4 The straight leads are put into the phantom at three positions (distance to the left border: P1 = 4.5 cm, P2 = 12 cm and P3 = 19.5 cm). 48

Fig. 3–5 The straight leads are put into the phantom at three positions (distance to the left border: P1 = 4.5 cm, P2 = 12 cm and P3 = 19.5 cm).....50
Fig. 3–6 Illustration of nine different trajectories for validation test (distance to the left border: S1, L1 and U1 are 2 cm; S2, L2 and U2 are 6 cm; S3, L3 and U3 are 10 cm.....51
Fig. 3–7 The geometry and connector for the four-wire cable. 53
Fig. 3–8 The transfer function of the four-wire cable.....54
Fig. 3–9 The comparison between induced voltage from direct measurement and induced voltage predicted from transfer function for the four-wire cable. 54
Fig. 3–10 The coax cable covered by a waterproof tape. 55
Fig. 3–11 The transfer function of the coax cable. 56
Fig. 3–12 The comparison between induced voltage from direct measurement and induced voltage predicted from transfer function for the coax. 57
Fig. 3–13 A set of 60 cm pacemaker lead transfer functions.....58
Fig. 3–14 A set of 53 cm pacemaker lead transfer functions.....59
Fig. 3–15 A set of 65 cm lead transfer functions.....60
Fig. 3–16 Two leads are laid parallel during the measurement. 62
Fig. 3–17 Two dual leads 65 cm transfer functions with different short lead length.63
Fig. 3–18 Two dual leads 65 cm transfer functions with different short lead length.64
Fig. 3–19 Illustration of the U-shaped and L-shaped lead paths in the patient's body.65
Fig. 3–20 Illustration of the fold-back path configurations in circular phantom for validation. 70

Fig. 3–21 Illustration of correlation between predicted (modeling) induced voltage and measured induced voltage. 73
Fig. 3–22 Histogram plot of relative error between predicted voltage and measured voltage. 74
Fig. 3–23 The relative error of predicted induced voltage decreases as the magnitude of the induced voltage increases. 74
Fig. 3–24 Comparison of solved and measured transfer function 1 using exactly calculated induced voltage and S L U lead path. 76
Fig. 3–25 Comparison of solved and measured transfer function 2 using exactly calculated induced voltage and S L U lead path. 77
Fig. 3–26 Comparison of solved and measured transfer function 1 using calculated induced voltage with 1% random error. 78
Fig. 3–27 Comparison of solved and measured transfer function 2 using calculated induced voltage with 1% random error. 79
Fig. 3–28 Eight lead trajectories with low correlated incident fields are used to solve transfer function from inaccurate induced voltage. 80
Fig. 3–29 Comparison of solved and measured transfer function 1 using calculated induced voltage on optimized trajectories with 20% random error. 82
Fig. 3–30 Comparison of solved and measured transfer function 2 using calculated induced voltage on optimized trajectories with 20% random error. 83
Fig. 3–31 Comparison of measured transfer function and solved transfer function from measured induced voltage. 84
Fig. 4–1 Transfer function (a) magnitude and (b) phase of the lead all in the saline. 86

Fig. 4–2 Transfer function (a) magnitude and (b) phase of the lead partial in and partial out of the saline. 86

Fig. 4–3 Transfer function (a) magnitude and (b) phase of the lead all out of the saline. 86

Fig. 4–4 Lead paths with adult male body model: (a) the over view; (b) all “in” lead path; (c) partially in, partially out lead path; (d) all “out” lead path. 87

Fig. 4–5 Lead paths with boy body model: (a) the over view; (b) all “in” lead path; (c) partially in, partially out lead path; (d) all “out” lead path. 88

Fig. 4–6 Lead paths with phantom model in (a) the side view and (b) the front view. 89

Fig. 4–7 Tangential incident field (a) magnitude and (b) phase along the lead path all in the adult male left chest. 89

Fig. 4–8 Tangential incident field (a) magnitude and (b) phase along the lead path partially in and partially out of the adult male left chest. 90

Fig. 4–9 Tangential incident field (a) magnitude and (b) phase along the lead path all out of the adult male left chest. 90

Fig. 4–10 Tangential incident field (a) magnitude and (b) phase along the lead path all in the boy left chest. 90

Fig. 4–11 Tangential incident field (a) magnitude and (b) phase along the lead path partially in and partially out of the boy left chest. 91

Fig. 4–12 Tangential incident field (a) magnitude and (b) phase along the lead path all out of the boy left chest. 91

Fig. 4–13 Tangential incident field (a) magnitude and (b) phase along the lead path all in the ASTM phantom with different sizes. 91

Fig. 4–14 Tangential incident field (a) magnitude and (b) phase along the lead path partially in and partially out of the ASTM phantom with different sizes. 92

Fig. 4–15 Tangential incident field (a) magnitude and (b) phase along the lead all out of the ASTM phantom with different sizes. 92

List of Tables

Table 3-1 Comparison of simulated of straight line. 49

Table 3-2 Comparison of simulated $\underline{E}_{end}$ of the U-shape leads, L1 and L4.....50

Table 3-3 Predicted induced voltage of leads set 1 in ASTM phantom. 66

Table 3-4 Measured induced voltage of leads set 1 in ASTM phantom.....66

Table 3-5 Percentage error between measurement and modeling of leads set 1. 66

Table 3-6 Measured and predicted induced voltage of a complex defibrillator lead 1.67

Table 3-7 Measured and predicted induced voltage of a complex defibrillator lead 2.68

Table 3-8 Predicted induced voltage of leads set 2 in both ASTM phantom and circular phantom.....70

Table 3-9 Measured induced voltage of leads set 2 in both ASTM phantom and circular phantom.....71

Table 3-10 Percentage error between measurement and modeling of leads set 2. 72

Table 4-1 Temperature rise in adult male model. 93

Table 4-2 Temperature rise in boy model.....93

Table 4-3 Temperature rise in ASTM phantom model.....93

Chapter 1 Introduction

Magnetic resonance imaging (MRI) has become a medical standard because it is an extremely accurate method of detecting disease throughout the body. The MRI use increased by 152% from 1997 to 2007. Over 25 millions MIR scans were performed in the United States in 2007 [1]. Cardiologists and radiologists have anticipated that three out of four pacing and defibrillation patients will need an MRI scan during the lifetime of their devices. However, patients currently with implantable medical devices, such as pacemakers and defibrillators, are prohibited from undergoing MRI because of serious concerns of tissue damage due to lead tip heating, induced arrhythmias and electromagnetic compatibility (EMC) issues [2]. Every 3 minutes in the United States and every 6 minutes in Europe, a patient with a pacemaker has to forego an MRI scan [3]-[6].

During MRI scanning, the electromagnetic signals emitted by a radio frequency (RF) coil penetrate human bodies and interacts with human tissues. If a metallic lead is present within these tissues, the lead works as an antenna. The induced current will be generated due to the RF signals from MRI coil, which poses a two-part risk. First, on the pacemaker device (pacemaker CAN) end, the induced voltage due to the RF signals could high enough to break the device. A broken pacemaker device could generate abnormal pacing, which is extremely dangerous. Second, on the pacemaker distal end, the electromagnetic signal can also generate a very strong electric field and causes a significant rise in local temperature. Such a large local temperature rise could exceed the safe limits for the particular tissues [7]. In some cases, the local temperature rise can exceed 30°C causing instant tissue damage [8].

To deal with the MRI compatibility problem, many large medical equipment companies are developing MRI compatible pacemaker systems. Meanwhile, examination of these new devices becomes a problem. To estimate MRI-induced lead heating and voltage effect, various researchers have performed carefully designed experiments and simulations [9]-[28]. Experiments were primarily performed on phantom models such as the ASTM phantom [14]-[17]. Electromagnetic simulations can be carried out on detailed anatomical human models [14], [15], [18]-[21]. With the recent advances in human model development, we can now obtain electromagnetic field distributions at millimeter resolution [29]. This provides the potential of electromagnetic modeling human bodies to understand the in-vivo MRI-induced heating on the implanted medical devices. In [22], simplified deep brain stimulation leads were modeled using thin wire models. However, such a study is limited to 1 mm resolution on a head model only and it requires simulations for over two days. For other leads with sub-millimeter features, such direct modeling can be extremely challenging.

Therefore, it is difficult to directly estimate the effect of those devices. On one hand, experiment method cannot be performed on patients and the phantom experiment cannot simulate many realities such as inhomogeneity of the human body. On the other hand, even with the current state of art electromagnetic modeling algorithms, it is still computationally prohibitive to model MRI RF coil, a human subject model, and detailed pacemaker system all together because of scale differences between metallic leads and MRI RF coil. The dimensions of a typical MRI RF coil are on the order of meters, while the feature size of pacemaker leads is in the order of sub-millimeters. Thus, significant computational resources, such as computer memory, are required. In addition, even with

some super computer with memory sufficient to accommodate the entire computational domain, the time cost may be still unacceptable because the tiny mesh size in the lead model limits the time-step size in FDTD simulations. For example, if some one were to use a 0.2 mm resolution grid size to model the pacemaker lead, the maximum time-step would be in the order of 10^{-13} of a second. For an MRI system operating at 64 MHz (1.5 T) or 128MHz (3 T), millions of time steps are required before simulation convergence.

To overcome the difficulty of direct estimation, people have tried to measure the transfer function of pacemaker systems, and combined it with the incident electric field from simulation to estimate MRI compatibility of the pacemaker system. However, the efficiency and accuracy of transfer function measurement have proven unsatisfactory. My research objective is to find an approach to generate an accurate transfer function for a pacemaker system, and to analyze the pacemaker safety issue based on the measured transfer function.

In the remainder of this dissertation, a method based on the reciprocity theorem is developed to estimate transfer functions in Chapter 2. In addition to the reciprocity approach, a fast transfer function is also proposed. After the description of the method, details of transfer function measurement setting are discussed. Furthermore, many different lead structures are studied. Numerical and experimental results for those structures are provided in Chapter 3. In addition, some preliminary studies on the effects of human body and phantom size are discussed in Chapter 4. Finally, the conclusion and future work are presented in Chapter 5.

Chapter 2 Methodology

2.1 Introduction of Pacemaker Transfer Function

It is different to directly estimate the induced voltage or heating effect of the pacemaker system by means of simulation or experiment as mentioned in Chapter 1. In practical, the process is divided into several manageable steps. First, electrical field distribution in the human body is extracted from simulation. With recent advances in human model development, we can obtain electromagnetic field distributions at millimeter resolution. Second, we need to evaluate the transfer function of the pacemaker system. Finally, the objective physical quantity, such as induced voltage or induced electrical field, can be calculated as the inner product of the tangential field along certain lead trajectory and the transfer function as shown in (1)

$$X = \int \underline{E}^{inc} \cdot tf \, \underline{dl} \,, \tag{1}$$

where X is the objective physical quantity, $\underline{E}^{inc}$ is the incident electric field, and tf is the transfer function. By using the transfer function idea, the computational difficulty of modeling the large-scale human body with the tiny lead structure is overcome. In addition, using the transfer function decouples the lead characteristics from the external environment, which means the further reducing the work of safety analysis. For example, to evaluate the induced voltage for a pacemaker lead along N different trajectories, the transfer function method only requires one transfer function measurement/simulation and one phantom/human body simulation. The induced voltage can be calculated immediately along N trajectories. However, using the conventional approach, N simulations are

needed to capture the induced voltage for pacemaker lead along N trajectories. This is also only possible for a very simple lead structure.

2.2 Pacemaker EMC Safety Analysis Procedure Using the Transfer function

As discussed in the introduction, the safety issues with pacemakers and MRIs include two parts: the tissue temperature rise around the distal end (inside the human hard muscle) of the lead and the induced voltage on the device CAN. By using the transfer function, the characteristic of the pacemaker lead is decoupled from the external environment. Based on the transfer function approach, the procedure to predict the EMC of the pacemaker/defibrillator with MRI is shown in **Fig. 2–1**.

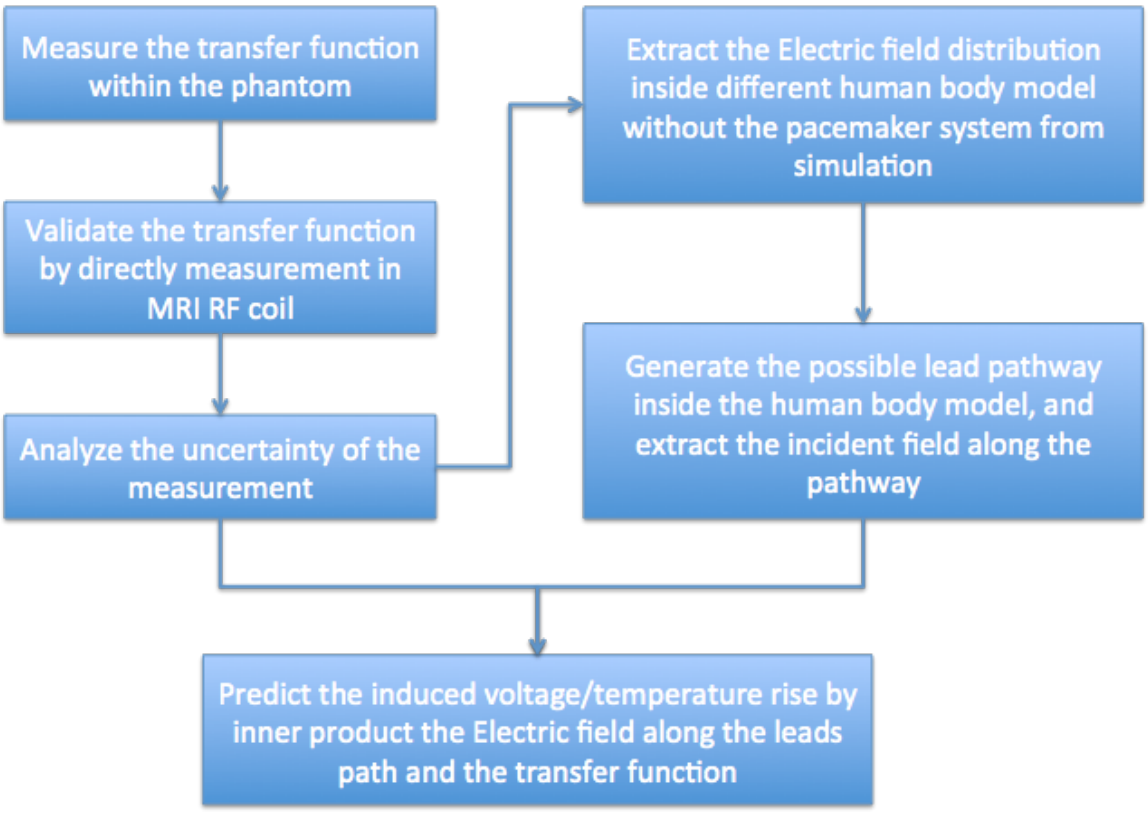

Fig. 2–1 The procedure of voltage/temperature prediction using transfer function.

The first step is to measure the transfer function of the pacemaker lead. The details of the method and the simulation/measurement setting of the transfer function will be discussed in upcoming sections. After having the transfer functions, validation tests are performed by directly measuring the induced voltage/heating on the pacemaker device in the saline/gel-filled ASTM phantom or circular phantom loaded inside the MRI RF coil. Then the uncertainty of the whole measurement is analyzed. Based on the uncertainty of the measurement, the input power of the MRI coil is set in the simulation, and the electric field along all possible leads pathways are extracted. At last, induced voltage/heating can be calculated as the inner product of the incident electric field and the transfer function.

After obtaining the predict results from the transfer function and human body model simulation, different steps for induced voltage analysis and heating analysis is performed. For the induced voltage, the worst case (highest induced voltage) or 95% worst case from all predicted voltages is found. Then, a voltage with double strength of the worst case is directly added to the device CAN. If the pacemaker still works normally, it should be safe from the induced voltage of the MRI environment. For the temperature rise, we do not know the exact limit of the heating. The blood flow reduces the heat while the transfer function is generated based on the gel with bad fluidity. As a result, the real temperature rise of the human heart muscle should be much lower than the predicted result, which should be the upper bound of the real case.

2.3 Transfer Function Estimation Approach

2.3.1 Direct Estimation of the Transfer Function

Both the magnitude and phase of the transfer function vary along the pacemaker leads. The transfer function value at a certain location is the ratio of the objective physical quantity and the incident field at that location. When the pacemaker system is placed in the MRI coil, the incident field is everywhere. However, if we need to directly measure the transfer function, we have to generate a very localized field as shown in **Fig. 2–2**. The magnitude and phase of the field should be a constant in the small region, and zero outside the region. The transfer function value of a certain point can be obtained by measuring the objective quantity when applying the localized field at the point on the lead. If we move the localized field along the lead and record the ratio of the objective quantity and the localized field, we can obtain the transfer function of the whole lead.

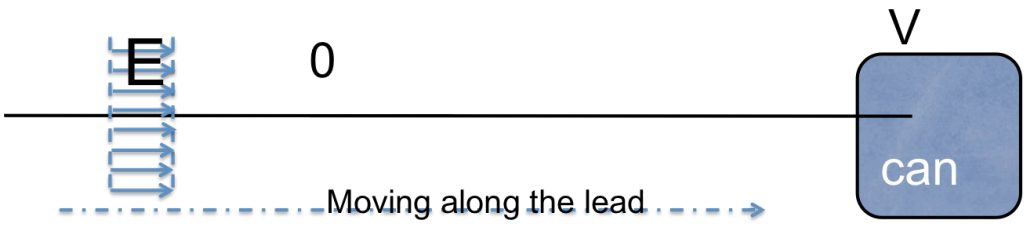

Fig. 2–2 A localized electrical field added on the lead to directly measure the transfer function.

Unfortunately, it is not efficient or even possible to directly estimate the transfer functions. On one hand, in an experiment, it is rather difficult to generate a very localized field. If the concentricity of the field cannot be guaranteed, namely applying an incident field to a relatively long segment of the lead, the transfer function obtained by direct measurement will not be accurate because it will represent an average sense transfer function. The average region depends on the region of the indent field. If a true transfer function varies very rapidly or demonstrates jump variation, the error of the measurement could be very significant, which is a very common case for practical defibrillator leads.

On the other hand, if simulation is desirable, the sub-millimeter leads structure must be modeled. This can be very time-consuming, assuming that the lead structure is even available. In very few cases, such as a temporary pacemaker, the leads structure is so simple that it can be modeled as thin wire. It may be possible to directly estimate the transfer function by simulation. However, depending on the lead length and accuracy requirement of the transfer function, dozens of simulations need to be run to obtain on transfer function because in each simulation we can only add the source (incident field) at one location that gives only one point value for the transfer function.

2.3.2 Using the Reciprocity Theorem to Estimate the Induced Voltage Transfer Function

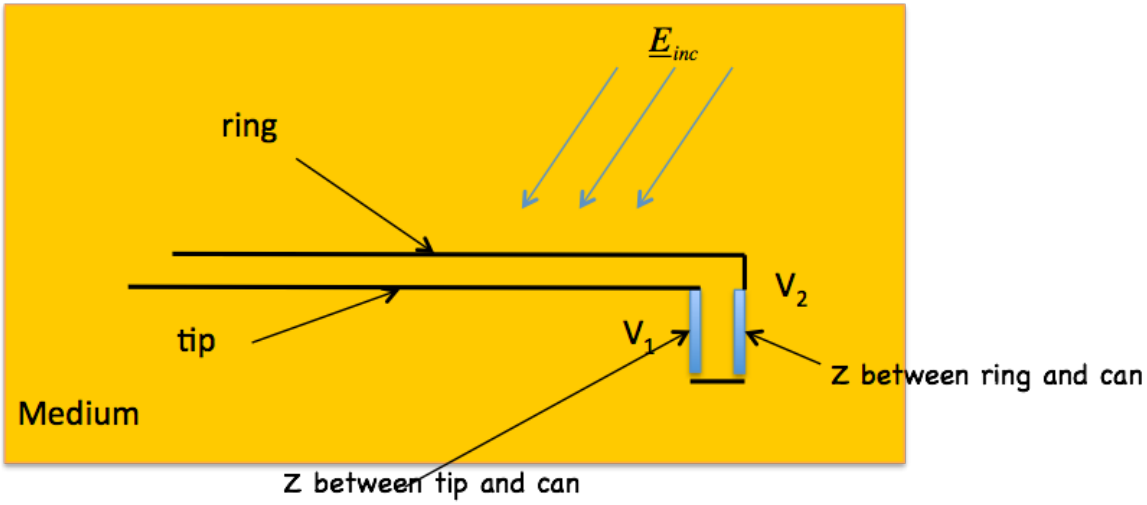

Fig. 2–3 The pacemaker system is modeled by device CAN impedance and two conduct leads. The conduct lead is insulated from the medium except for a short segment at the distal end (the end plugged in human heart muscle).

To overcome the problem of direct measurement, we propose a reversed indirect method. Instead of applying the excitation to the lead, we locate the source at the lead tip where the temperature rise occurs, or between different electros on the device CAN where the induced voltage is generated. Then, we measure the current distribution along

the lead. The equivalence of the reversed indirect method and the direct measurement is proven as follows. The whole derivation of induced voltage transfer function is shown. The idea of heating transfer function, which differs slightly, will be discussed later.

The pacemaker system includes a pacemaker device CAN and pacemaker lead. The pacemaker CAN contains a battery case and a control circuit to generate the pacing signal. A similar structure appears in various implantable devices such as defibrillators, spinal cord stimulators, and VNS (Vagus Nerve Stimulation) therapy generators. Usually, the lead consists of two conductors (tip and ring) to carry the differential pacing signal. The two conductors are connected to different electros of the CAN. The objective quantity of the induced voltage transfer function is the induced voltage between different electros or the induced voltage between the electros and the ground of the CAN (the metallic shell of the CAN). We model the pacemaker system as shown in **Fig. 2–3**, where Z is the impedance between the electros and the ground of the CAN; tip and ring are the inner and outer conductor of the lead respectively. The lead is insulated from the medium except for short segment at the end plugged into the human heart muscle (distal end).

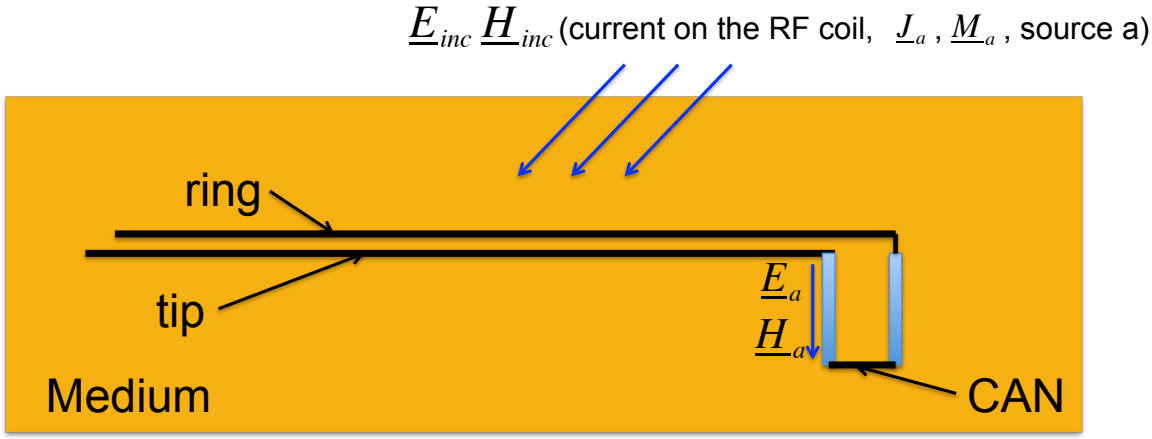

(a) The MRI RF coil is on and generates the incident fields $\underline{E}_{inc}$, $\underline{H}_{inc}$ as well as the induced field $\underline{E}_a$, $\underline{H}_a$ at the port between tip electro and shell of the CAN.

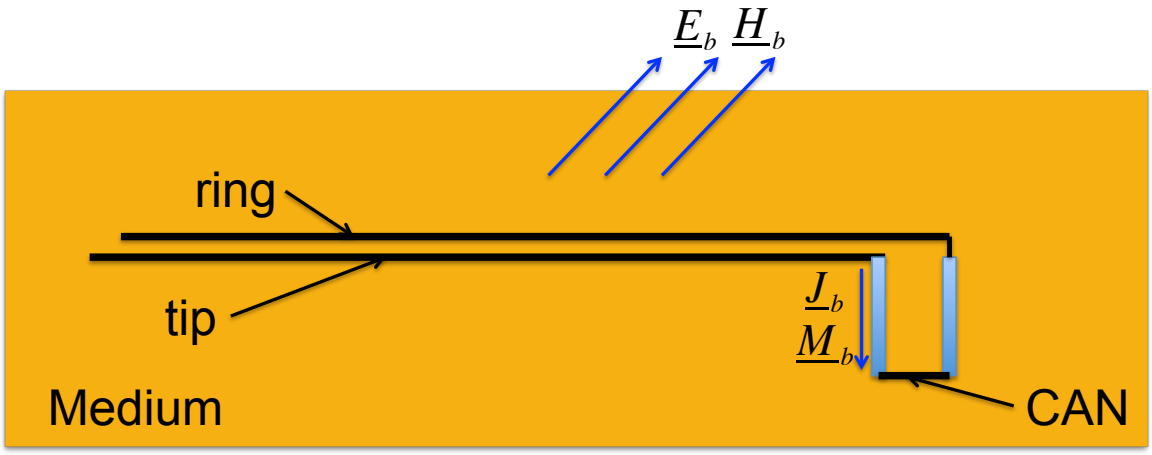

(b) Current excitation $\underline{J}_b$ and $\underline{M}_b$ are added between the tip electro and the shell of the device CAN.

Fig. 2–4 Two sets of sources are applied to the pacemaker system individually.

Instead of directly measuring the voltage on the CAN, we apply a current source to the CAN (between the tip electros and the ground of the CAN if tip to CAN induced voltage is required). By doing this, two sets of sources $\underline{J}_a$, $\underline{M}_a$ and $\underline{J}_b$, $\underline{M}_b$ are excited individually that produce $\underline{E}_a$, $\underline{H}_a$ and $\underline{E}_b$, $\underline{H}_b$ as shown in **Fig. 2–4**. The reciprocity relation between the two sets of sources and fields is

$$\int \underline{E}_a \cdot \underline{J}_b - \underline{H}_a \cdot \underline{M}_b \, dv = \int \underline{E}_b \cdot \underline{J}_a - \underline{H}_b \cdot \underline{M}_a \, dv \,, \tag{2}$$

where $\underline{J}_a$, $\underline{M}_a$ are the current flowing on the MRI RF coil, and $\underline{J}_b$, $\underline{M}_b$ are the source added on the device CAN (between the electors an the shell of the CAN). Because the induced voltage needs to be estimated, only add electrical current source is applied on the device CAN, and the second term of the integrand on the left side of the equation disappears. To connect the induced voltage and the reciprocity equation, the equation is normalized by the magnitude of the current source on both sides

$$\frac{\int \underline{E}_a \cdot \underline{J}_b \, dv}{I_b} = \frac{\int \underline{E}_b \cdot \underline{J}_a - \underline{H}_b \cdot \underline{M}_a \, dv}{I_b} \,, \tag{3}$$

where I_b is the current magnitude. If the current source is a line source, the volume integration $\int \underline{E}_a \cdot \underline{J}_b \, dv$ is reduced to a line integral $I_b \int \underline{E}_a \cdot \underline{\hat{l}} \, dl$, where $\underline{\hat{l}}$ is the unit vector along $\underline{J}_b$. Meanwhile, the induced voltage can also be represented as the line integral of the electrical field along the port (between the electros and the shell of the CAN):

$$V = \int \underline{E}_a \cdot \underline{\hat{l}} \, dl = \frac{\int \underline{E}_b \cdot \underline{J}_a - \underline{H}_b \cdot \underline{M}_a \, dv}{I_b}. \tag{4}$$

Once $\underline{E}_b$, $\underline{H}_b$ and $\underline{J}_a$, $\underline{M}_a$ are known, we can calculate the induced voltage on the port. Unfortunately, it is even more difficult to estimate those sources and fields than to directly estimate the transfer function because the evaluation of the $\underline{E}_b$ and $\underline{H}_b$ at MRI RF coil is impossible without also considering the human body.

To avoid the calculation of $\underline{E}_b$, $\underline{H}_b$, the reciprocity theorem is applied again on an equivalent source. Because the dimension of the port is about one or two cm too small compared with the lead length, and the whole system works at 64MHz, the radiation of the port can be neglected. Similarly, compared with the lead length the device CAN dimension is also electrically small. If we also ignore the radiation of the device CAN and consider the CAN effect as an uncertainty of our method later, the radiation of the pacemaker system mainly comes from the lead radiation. Namely, $\underline{E}_b$ and $\underline{H}_b$ are come from the electrical current flowing on the pacemaker lead, which is noted as source I_β since the system does not have any magnetic current. Consequently, the two sets of sources become the current on the MRI RF coil and the electrical current on the pacemaker lead as shown in **Fig. 2–5**.

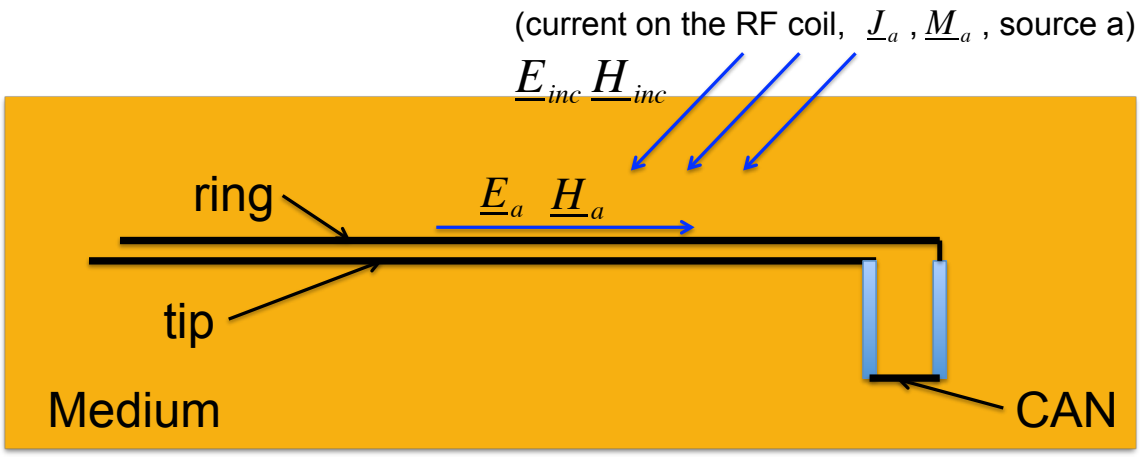

(a) The MRI RF coil is on and generates the incident fields $\underline{E}_a$, $\underline{H}_a$ along the lead.

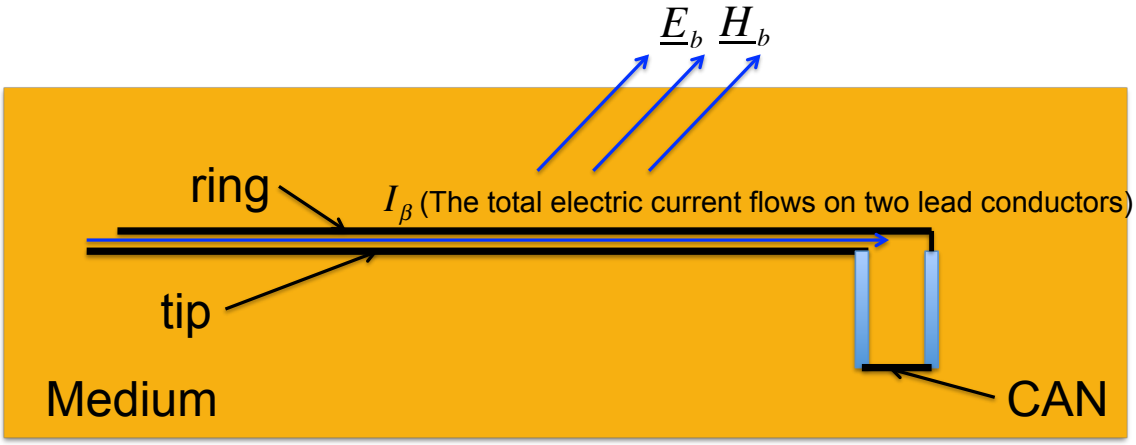

(b) Current I_β applied along the lead generates $\underline{E}_b$ and $\underline{H}_b$.

Fig. 2–5 Two sets of new sources are applied to the pacemaker system individually.

By applying the reciprocity theorem on the two sets of the new source, we obtain

$$\int \underline{E}_a \cdot I_\beta \underline{dl} = \int \underline{E}_b \cdot \underline{J}_a - \underline{H}_b \cdot \underline{M}_a \, dv \,, \tag{5}$$

where I_β is the current distribution on the lead when current excitation $\underline{J}_b$ is applied to the device CAN and $\underline{E}_a$ becomes the incident field along the lead path without the lead present. Combining equations (4) and (5), the induced voltage on the device CAN can be calculated by

$$V = \int \underline{E}_a \cdot \hat{\underline{l}}\, dl = \int \underline{E}_a \cdot \frac{I_\beta}{I_b} \underline{dl} = \int \underline{E}_a \cdot tf_v \underline{dl}\,, \tag{6}$$

where $\underline{E}_a$ is the incident electric field along the lead that can be found from a simulation without the tiny lead structure, I_β can be either calculated from simulation or measured after impressing I_b to the device CAN, and tf_v is the induced voltage transfer function that is a voltage to voltage transfer function whose value is equivalent to the normalized current distribution along the pacemaker lead as we can see in the equation (6). This transfer function can be evaluated individually without consider the human body and the MRI RF coil.

In the reciprocity approach, the transfer function can be estimated by either simulation or measurement. For a simple lead structure such as thin wire or twin leads, one simulation is sufficient to calculate the transfer function. However, in directly estimation of the transfer function, many simulations are needed depending on the resolution of the transfer function. For a complex lead structure, measurement is a much more effective because we only care about the total current on the lead regardless of the lead complexity, and the total current can be easily measured using a current probe.

2.3.3 Using the Reciprocity Theorem to Estimate the Heating Transfer Function

Unlike the induced voltage transfer function, the reciprocity theorem cannot be directly applied because the objective quantity is a thermal quantity rather than an electrical quantity. Meanwhile, all the problems of direct estimation of the transfer function remain. Therefore, we still need to reverse the problem by applying the reciprocity theorem.

The most frequently-used model for the thermal Bio-EM problem is the "Bioheat Equation" (BPE), developed in 1948 by Pennes [33]. The formula is

$$\rho c \frac{\partial T}{\partial t} = \nabla \cdot \left(k \nabla T \right) + \rho Q + \rho S - \rho_b c_b \rho \omega \left(T - T_b \right), \tag{7}$$

where k is the thermal conductivity, S is the specific absorption rate (SAR), ω is the perfusion rate, and Q is the metabolic heat generation rate. ρ is the density of the medium; ρ_b, c_b and T_b are the density, specific heat capacity and temperature of blood, respectively. The equation can be simplified for our case because the heating measurement is preformed in a gel-filled ASTM phantom in which there is no metabolic heat generation and heat transfer by blood. Thus, the equation is simplified to

$$\rho c \frac{\partial T}{\partial t} = \nabla \cdot \left(k \nabla T \right) + \rho S, \tag{8}$$

where ρ, c, k are the density of the medium, specific heat capacity and thermal conductivity, respectively.

From the simplified equation, the temperature rise at a certain time should be proportional to the local SAR, which is closely related with the electrical field. The relation between the local SAR and electrical field is

$$S = \frac{\sigma}{2\rho} |E|^2, \tag{9}$$

where E is the local electrical field. Therefore, the local temperature rise over a certain period of time is proportional to the square of the magnitude to the electrical field. this means that we can estimate the temperature rise of tissue around the lead distal end if we can estimate the electrical field at the same location. Since the electrical field is certainly

an electrical quantity, we can apply the reciprocity approach to evaluate the transfer function of the distal end electrical field.

For the induced voltage transfer function evaluation, a current source is applied to the device CAN to create a connection between the induced voltage and the electrical field along the port between the electros and the shell of the CAN. A similar source becomes a simple infinitesimal dipole here in thermal transfer function estimation, as shown in Fig. 2–6, since the objective quantity is an electric field. The lead in heating estimation can be modeled as a signal lead since the structure inside is irrelevant; we are concerned only with the total current on the lead. The rest of the derivation is almost the same and will be skipped.

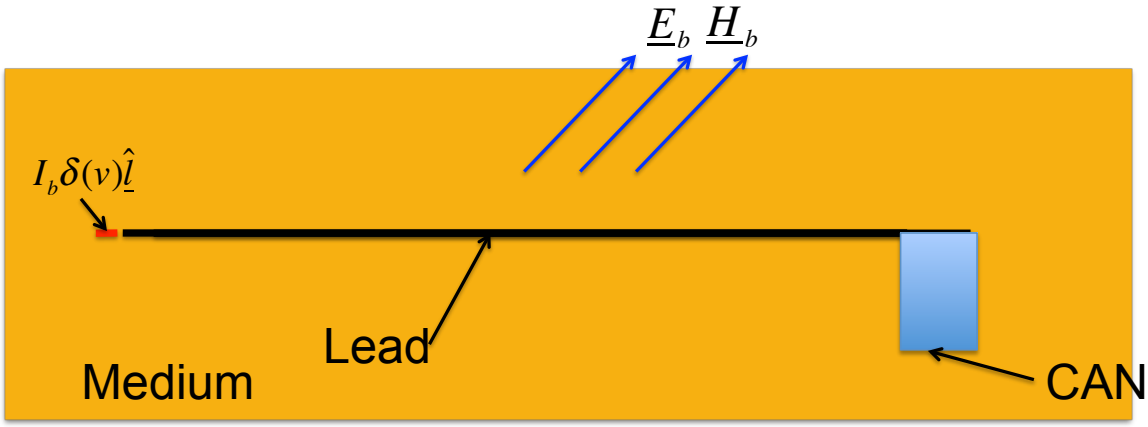

Fig. 2–6 An infinitesimal dipole is added next to the lead distal end as the second excitation to apply the reciprocity.

By applying reciprocity, the distal end electrical field transfer function of the lead is the same as the normalized current distribution on the lead after adding an electric dipole near the distal end of the lead

$$E_{end} = \int \underline{E}_{inc} \cdot \frac{I_\beta}{I_b} \hat{\underline{l}}\, dl = \int \underline{E}_{inc} \cdot tf_T \underline{dl}\,, \tag{10}$$

where E_{end} is the electrical field where the testing dipole is located due to the lead structure. The total electrical field here is the sum of E_{end} and the direct incident field at this point. What we care is the temperature rise or the induced electrical field due to the lead structure. Therefore, rather than the total field, the transfer function is used to predict the E_{end}. I_β is the total current flowing on the lead when a dipole is added at the lead distal end with dipole moment of I_b and tf_T is the heating transfer function, which is a voltage to electrical field transfer function whose value equals the ratio of I_β and I_b. This equation will be used in 3.1 in thin wire lead transfer function validation.

The equation to calculate the temperature is

$$\Delta T = \alpha \left| E_{end} \right|^2 = \alpha \left| \int \underline{E}_{inc} \cdot tf_T \, \underline{dl} \right|^2, \tag{11}$$

where α is the proportional coefficient between the square of electrical field magnitude and the temperature rise over a certain time. To determine the proportional coefficient, the temperature rise is evaluated using both direct measurement and transfer function. The details of measurement set up will be described later. The proportional coefficient is equal to the ratio of the directly measured temperature rise and the predicted temperature rise by transfer function:

$$\alpha = \frac{\Delta T_{measured}}{\Delta T_{tf}}. \tag{12}$$

2.3.4 Fast Transfer Function Estimation

The reciprocity approach provides a very accurate and efficient way to evaluate the transfer function. However, it still requires one measurement/simulation to evaluate the transfer function and several directly measurements to validate the transfer function.

For many complex leads with discontinued lead structure, such as defibrillator leads, leads with built-in filters or dual lead cases, the complete reciprocity process must be performed. Meanwhile, many leads have complex but relatively continuous structures. For example, most signal pacemaker leads have a coaxial structure; both the outer and inner conductors are helixes; and some complex structures may be built at the lead end. The lead structure is already too complex to be modeled in a simulation. However, the whole structure is continuous except the lead end structure. We can expect a continuous transfer function with relative slowly variation on this kind of lead structure because the transfer function is equivalent to a current distribution after applying an excitation at the lead end or device CAN, and the current should be continuous in this kind of structure. Based on the continuous slow changing assumption, a fast transfer function estimation approach is proposed. In this method, evaluating the whole transfer function only requires several directly measurements/simulations, which are also required in reciprocity approach for transfer function validation purposes.

Firstly, we notice that most pacemakers/defibrillators range in length from 40 cm to 60 cm. Considering normal saline with a conductivity of 0.47 S/m and relative permittivity of 80, the wavelength of a 64 MHz electromagnetic wave is 0.5237 m. The length of the lead is about 1 to 1.25 times longer than the wavelength in the saline. The lead made by good conductors can be considered as a wire antenna. Although it is located in a lossy media, most part of the lead, except the lead end, is insulated from the external environment. Therefore, it is assumed that the current distribution can be linearly represented by a set of bases with variation slower than 1.25 period along the lead:

$$TF = \sum_{n=1}^{N} C_n B_n \quad , \tag{13}$$

where B_n is the nth base function and C_n is the coefficient.

The original bases set is chosen as $\{1, \exp(-j\frac{1}{4}\frac{2\pi}{L}l)$, $\exp(-j\frac{1}{2}\frac{2\pi}{L}l)$, $\exp(-j\frac{3}{4}\frac{2\pi}{L}l)$, $\exp(-j\frac{2\pi}{L}l)$, $\exp(-j\frac{5}{4}\frac{2\pi}{L}l)\}$, where the L is the lead length and l is the distance from the lead distal end. This set of bases should be able to capture all the current variation along the lead. As discussed in 2.1, the objective quantity can be calculated as the inner product of the transfer function and the incident field as equation (1). Substitute the equation (13) in to equation (1), and the objective quantity (induced voltage or electric field) can be written as

$$X = \int \underline{E}_{inc} \cdot TF \, \underline{dl} = \sum_{n=1}^{N} C_n \int \underline{E}_{inc} \cdot B_n \, \underline{dl} \,. \tag{14}$$

Second, several induced voltages or electric fields are directly measured to solve the coefficient C_n. The measurement details are described in section 2.5.3. Since six order bases are chosen, a minimum of six induced voltages or fields from different lead trajectories are needed to build a linear equation as

$$\sum_{n=1}^{N} C_n \int \underline{E}_{inc}^{m} \cdot B_n \, \underline{dl} = X_m \tag{15}$$

where X_m is the mth induced voltage or field and $\underline{E}_{inc}^{m}$ is the incident electrical field along the mth lead trajectory.

The method should work in an ideal case, namely if the measured induced voltage or induced field is perfectly accurate. In the event of a measurement error, the solved coefficient C_n would have a huge error. This error amplification results from the highly correlated bases function. Although the bases function set is already linear independent,

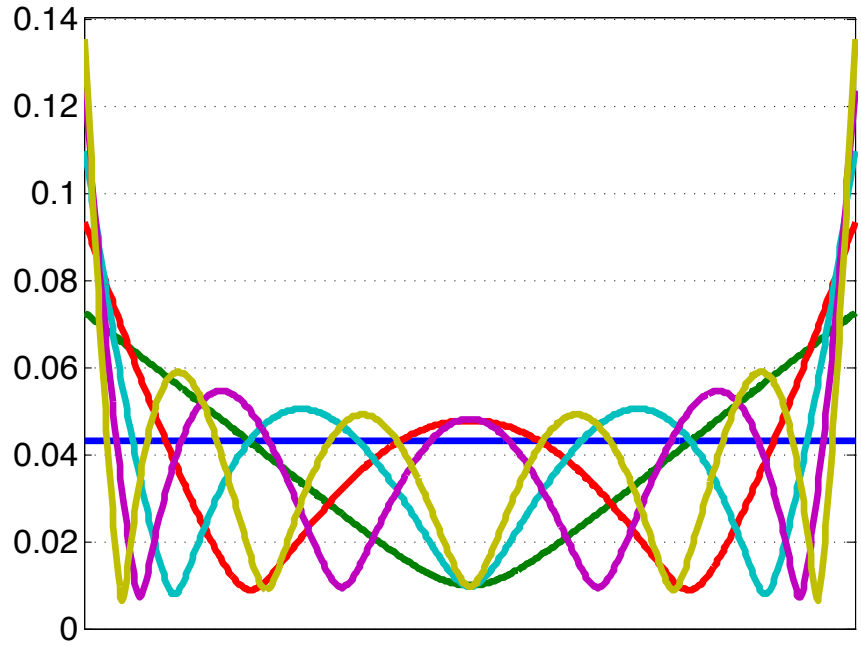

(a) Magnitude

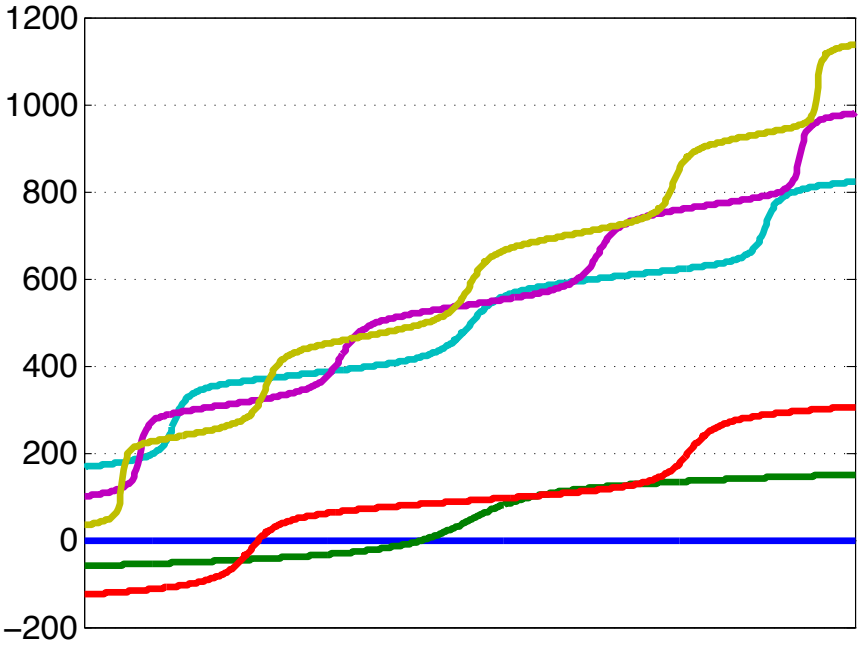

(b) Unwrapped phase

Fig. 2–7 The orthogonalized bases to represent the transfer function.

the correlation coefficient between them is very high, which makes the condition number of the matrix $\left[\int \underline{E}_{inc}^{m} \cdot B_n \underline{dl}\right]_{6\times6}$ very large. To reduce the condition number, a Gram-Schmidt process is applied to the bases to produce an orthogonal bases set. The magnitude and phase of the orthogonalized bases are plotted in Fig. 2–7.

2.4 Numerical Modeling of the MRI RF Coil and Phantom

SEMCAD X is a commercial full-wave electromagnetic simulation software package. It is used to model the MRI RF coil, human body, and simple lead structure. To model a physical RF coil, all the details of the coil dimension, such as shape and size of each rung and end-ring, are needed. In addition, it takes a very long time to achieve convergence of the simulation. Meanwhile, a non-physical coil can produce the same electromagnetic field distribution in far less simulation time. Therefore, instead of modeling the practical physical coil, we use the non-physical coil model to generate the field in our study. The non-physical coil only contains eight rungs provided by the SEMCAD shown in Fig. 2–8.

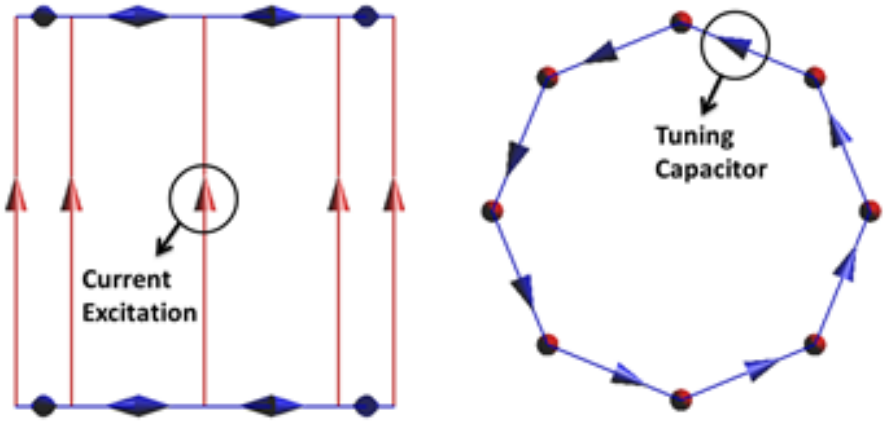

Fig. 2–8 1.5 T MRI RF coil model in SEMCAD.

The red arrows indicate the current sources, while the blue arrows represent the end-ring capacitors. In our study, the value of the end-ring capacitors is 7.2 pF, which is determined by adjusting the second highest resonant frequency to 64 MHz. The model has eight rungs, each of which has a length of 65 cm. The diameter of the end ring is 63 cm.

Phantom models described in ASTM F2182-11a[34] are then placed inside this coil. The dimensions of two types of ASTM phantoms, as well as a circular phantom, are shown in Fig. 2–9. The phantom is filled with saline having a conductivity of 0.47 S/m and a relative permittivity of 80 at 64 MHz. The field distribution in the center plane of the phantom is plotted in Fig. 2–10 .

The rectangular phantom and the phantom with head are standard phantoms frequent used in our measurements and simulations. A circular phantom is sometimes used because the electric field is almost a constant along the circumference, whose magnitude changes with that of the radius as shown in Fig. 2–10(e).

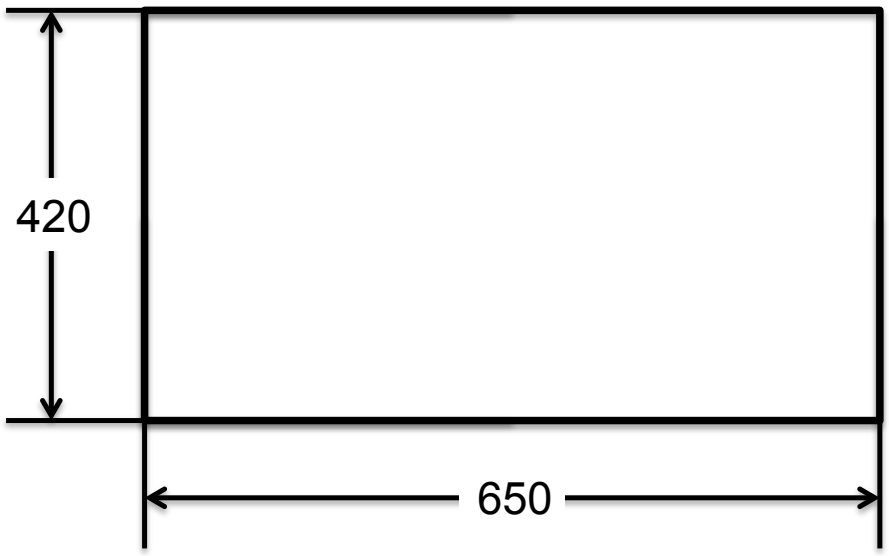

(a) Rectangular ASTM phantom.

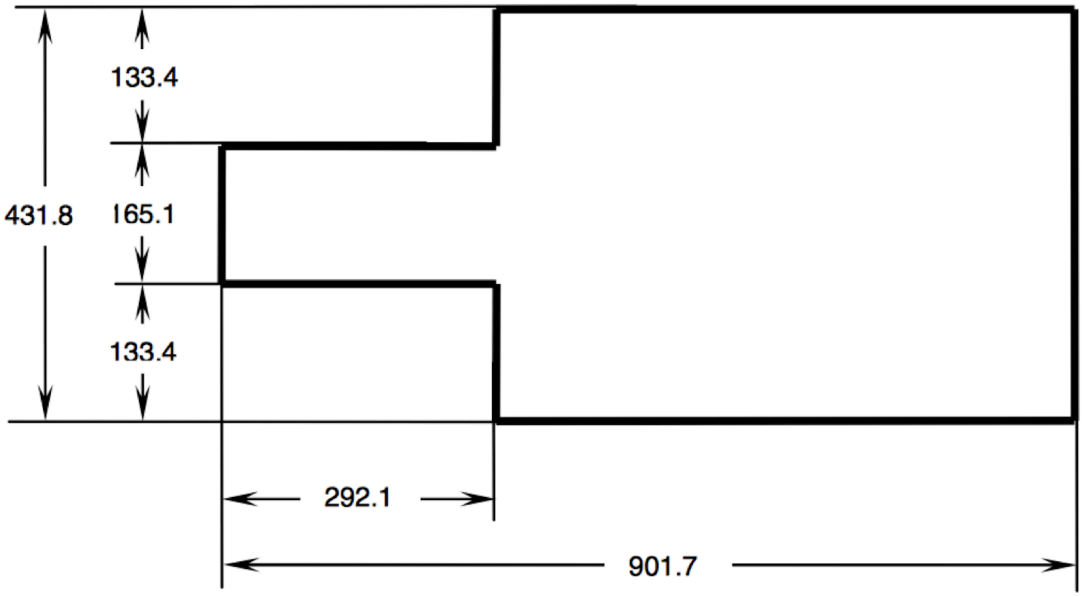

(b) ASTM phantom with head.

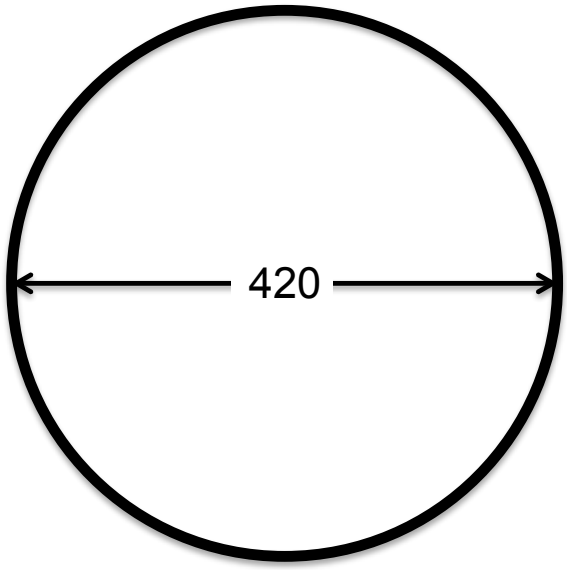

(c) Circular phantom.

Fig. 2–9 The ASTM phantom dimension in mm.

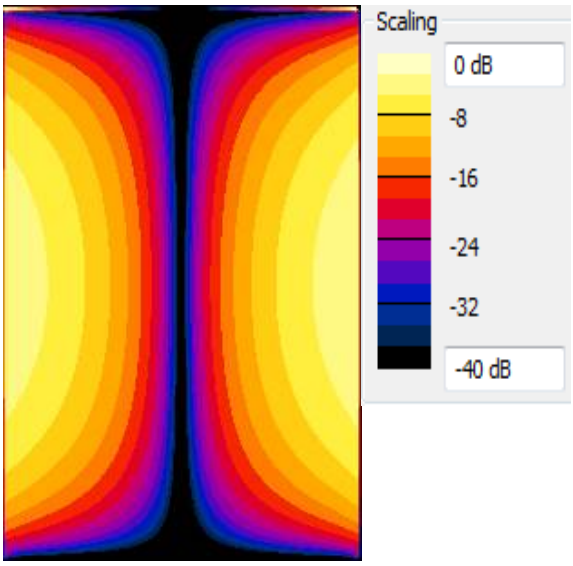

(a) E_z in the rectangular phantom.

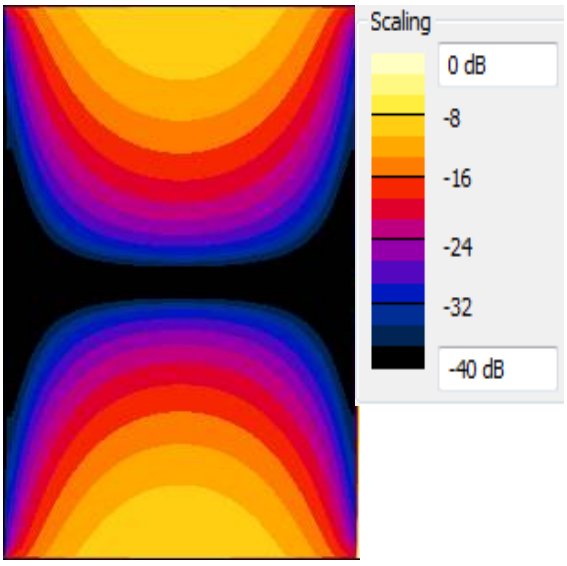

(b) E_x in the rectangular phantom.

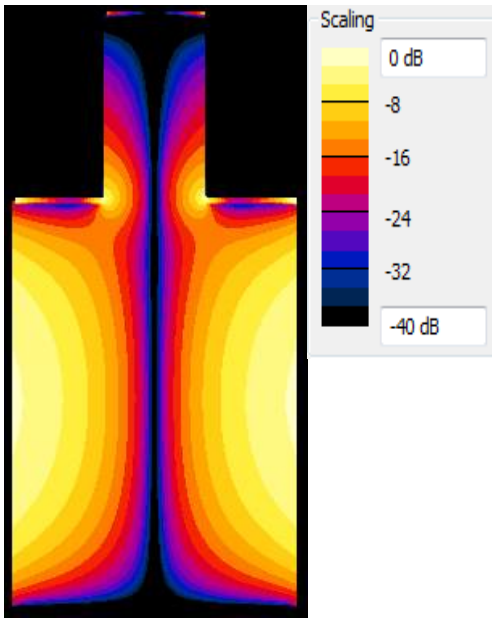

(c) E_z in the phantom with head.

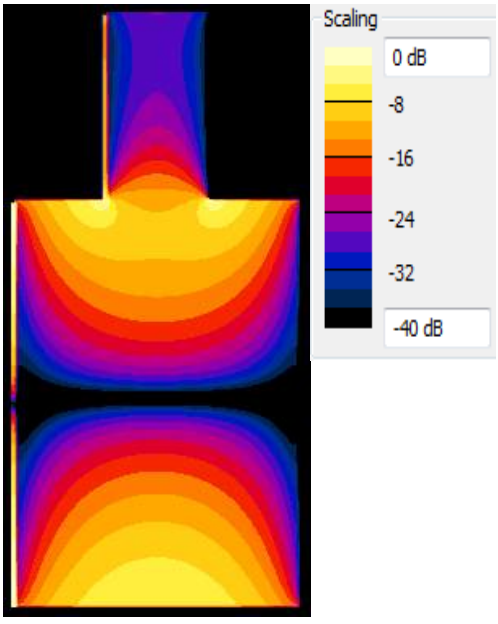

(d) E_x in the phantom with head.

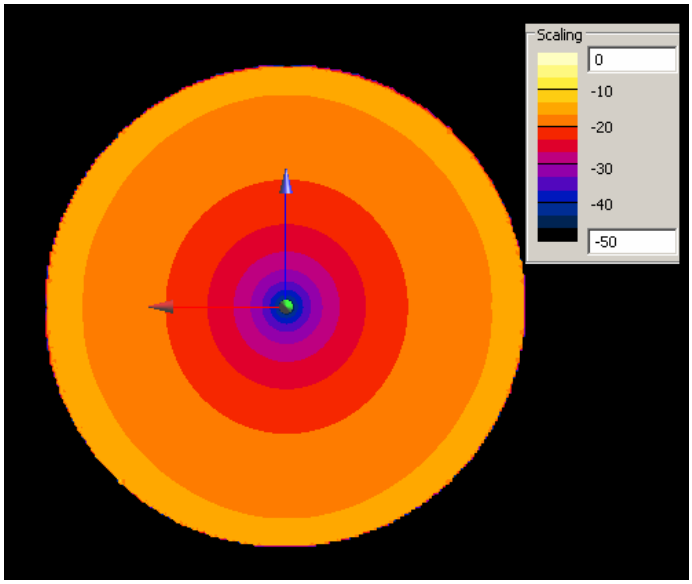

(e) Electric field magnitude in the circular phantom.

Fig. 2–10 The incident electric field distribution in dB in the vertical center plane.

2.5 Measurement Settings

2.5.1 Transfer Function Measurement

As derived in the Methodology, to measure the transfer function, an excitation is applied at the device CAN or lead distal end, and the current distribution along the lead is measured.

For the current measurement, a Pearson Electronics current probe is chosen as shown in Fig. 2–11. The sensitivity of the probe is 1 ± 1% V/A. The output resistance is 50 Ohm. The 3dB bandwidth is 500Hz ~ 250MHz.

To record the ratio of the current distribution on the lead and the excitation, the NI PXIe-5630 6 GHz vector network analyzer (VNA) is used as shown in Fig. 2–12. It is a simple 2 ports VNA. With the LabView interface, the S parameter can be easily recorded.

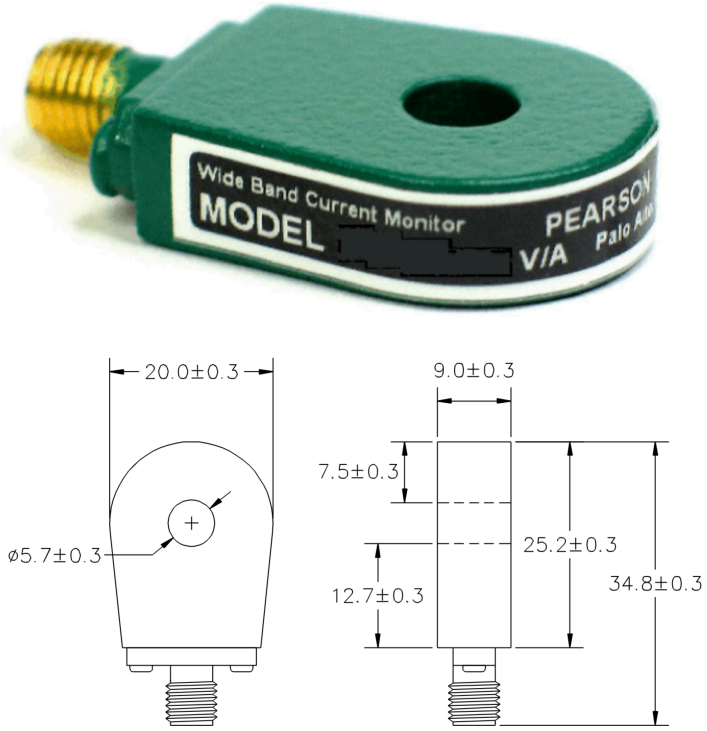

Fig. 2–11 The dimension of the current probe from Pearson electronics.

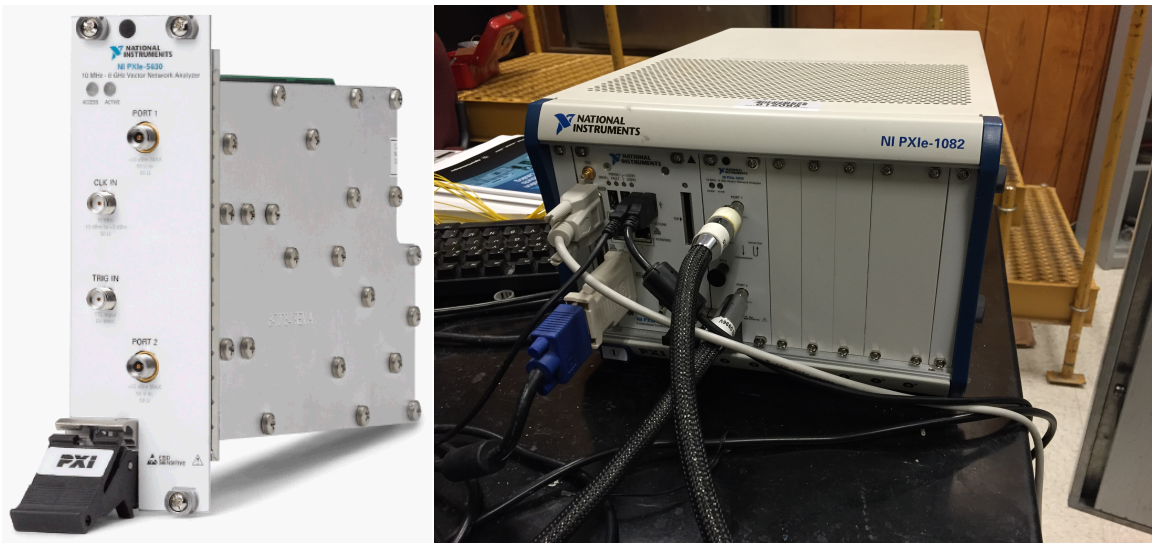

Fig. 2–12 NI PXIe-5360 vector network analyzer with NI PXIe-1082 PXI Express Chassis.

2.5.1.1 Induced Voltage Transfer functions

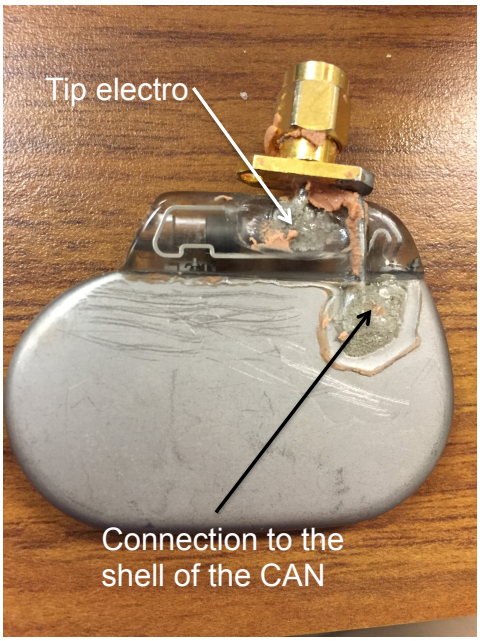

Fig. 2–13 The modified device CAN with a SMA connector.

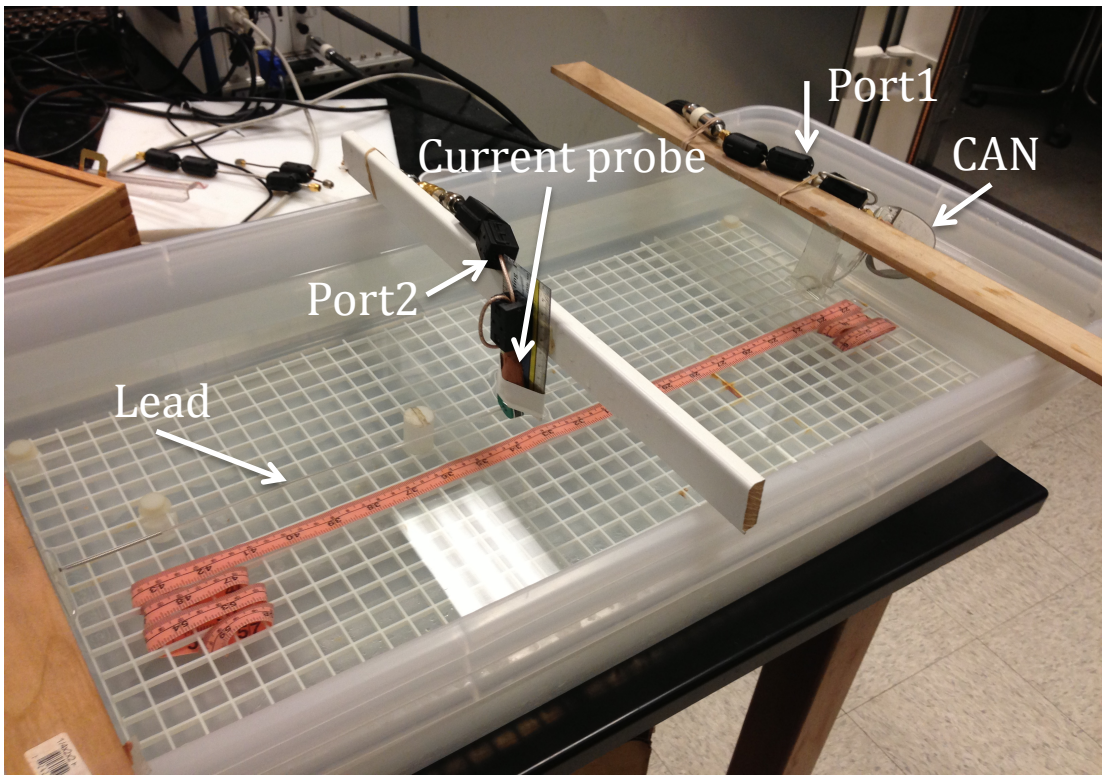

Fig. 2–14 Induced voltage transfer function measurement configuration.

In this measurement, an excitation is applied to the device CAN between the electros and the shell of the CAN. A plastic shell usually covers the electros of the ring/tip. To applying the excitation, we carefully rub away the plastic to expose the electros without breaking them. All the metallic electros and shell of the device CAN are usually made of titanium, which is non-magnetic and can be used in an MRI environment, but cannot be soldered. Therefore, we use a conductive glue to connect the electros and a SMA RF connector as shown in Fig. 2–13.

The modified device CAN with a RF connector can be connected to the VAN port. As shown in the Fig. 2–14, port 1 of the VNA is connected to the SMA connector on the device CAN as the excitation. Port 2 of the VNA is connected to the current probe. During the measurement, we move the current probe along the lead one cm a time and record the s11 and s21 of the system. The whole lead, current probe, and most of the device are immersed in the saline with a conductivity of 0.47 S/m and a relative permittivity of 80.

Two assumptions are made in this measurement: 1) the current probe does not change the characteristic of the lead, and 2) the impedance between the electros and shell of the CAN does not change significantly when VNA port 1 is connected. The s11 variation is usually very small during the measurement. The typical value of the changes is less than 0.1% wherever the current probe is along the lead, indicating that the current probe does not change the impedance of the pacemaker system. The impedance between the electros and shell of the CAN can be calculated from S11 using

$$Z_{can} = Z_0 \frac{1+S_{11}}{1-S_{11}}, \tag{16}$$

where Z_{can} is the CAN impedance and Z_0 is the VNA port impedance whose typical value is 50 Ohm. If we directly connect port 1 to the device CAN, based on the measured S_{11}, the typical impedance of the CAN is about several ohms, and in most cases, it shows weekly capacitive. This impedance is relatively small compared with 50 Ohm impedance of the VNA port. Therefore, the two assumptions of our measurements are tenable, in other words, the characteristics of the pacemaker system do not change due to the measurement configuration.

The object of this measurement is to record the ratio of the current on the lead and the strength of the excitation current, which can be calculated from measured S_{21} and S_{11}. The relationships between S_{21}, S_{11} and other values in the measurement are as follows:

$$I_{lead} = V_2, \tag{17}$$

$$S_{21} = V_2/V_1, \text{ and} \tag{18}$$

$$I_s = \frac{V_1(1+S_{11})}{Z_{can}}, \tag{19}$$

where I_{lead} is the current value of a certain point on the lead, V_2 is the outgoing voltage of port2, and V_1 is the incoming voltage of port1. Equation (17) holds because the current probe has 1 V/A sensitivity and 50 Ohms output that matches the input impedance of the VNA cable. S_{21} is the ratio of the outgoing wave function of port 2 and the incoming wave function of port 1, which is equal to the ratio of the outgoing voltage of port 2 and the incoming voltage of port 1 since the VNA cables connected to the two ports have the same impedance. Equation (19) is the simple Ohm's law on port 1. Combining equations (16)-(19) together, the ratio of the current on the lead and the excitation current can be represented as

$$TF = \frac{I_{lead}}{I_s} = Z_0 S_{21} \frac{1}{1 - S_{11}}, \tag{20}$$

which is also equal to the transfer function of the lead.

Fig. 2–15 A simple balun made by coaxial cable and magnetic core.

However, in reality measurement we do not directly evaluate the transfer function using equation (20). If the VNA cable is directly connected to the device CAN, due to the mismatch on port 1 and the inherent drawbacks of the VNA, significant interference between cables and lead as well as cables themselves occurs because of the common mode current. To reduce the effect of the common mode current, simple baluns made using coaxial cable and magnetic cores are connected between VNA cables and the CAN as shown in Fig. 2–15. Although these simple baluns are not the terribly efficient, they work well in this measurement because the whole system works at 64 MHz that is not a very high frequency. Adding the baluns eliminates interference.

The measured scatter perimeter is not accurate since a lossy transmission line is connected in series. The true measured scatter perimeter should be

$$S'_{11} = C_{11} S_{11}, \text{ and} \tag{21}$$

$$S'_{21} = C_{21} S_{21}, \tag{22}$$

where the S'_{11}, S'_{21} are the true measured scatter perimeter and C_{11} , C_{21} are the complex ratio of the true measured scatter perimeter and the accurate scatter perimeter. Because complex ratios should only correlate with the baluns, they should be constant during the measurement. Using equation (20) to calculate the transfer function, the result would be

$$TF' = Z_0 C_{21} S_{21} \frac{1}{1 - C_{11} S_{11}}. \tag{23}$$

The ratio of the new result and the correct transfer function is a function of S_{11}. Since S_{11} does not change during the measurement, the ratio is a complex constant $\frac{C_{21}(1 - S_{11})}{1 - C_{11} S_{11}}$.

Furthermore, we can also pack all terms together except the measured $S'_{21} = C_{21} S_{21}$. The correct transfer function can be represented by S'_{21}:

$$TF = S'_{21} \frac{Z_0}{C_{21}} \frac{1}{1 - S_{11}}. \tag{24}$$

Therefore, the correct transfer function is proportional to the measured S'_{21} when baluns are added. S'_{21} can be considered as an un-scaled transfer function.

To determine the coefficient, rather than performing a series of measuremens to evaluate the ratio of the scatter perimeters with and without baluns, another more accurate, easier to implement approach can be used. After obtaining the un-scaled transfer function, the inner product of the incident field from the simulation and the un-scaled transfer function can be used to predict an induced voltage. By loading the lead in the phantom into the MRI RF coil, another induced voltage is measured. The details of

the measurement setting will be described later. The ratio of the measured induced voltage and the predicted induced voltage should have the same magnitude of the scaling coefficient of the transfer function, but different phases. Since only the magnitude of the voltage matters in the induced voltage prediction, we can scale the transfer function by this real coefficient and then use the scaled transfer function to predict the magnitude of the induced voltage.

2.5.1.2 Heating Transfer functions

As discussed in the Section 2.3, in fact, the heating transfer function is the distal lead end induced electrical field transfer function. To estimate the induced electrical field at the lead distal end, an electric dipole is needed as an excitation. A semi-rigid coaxial cable is used to build a dipole. 0.5 cm long out conductor at the end of the cable is striped off. A lossy material, as shown in Fig. 2–16, covers the rest part of the coaxial cable.

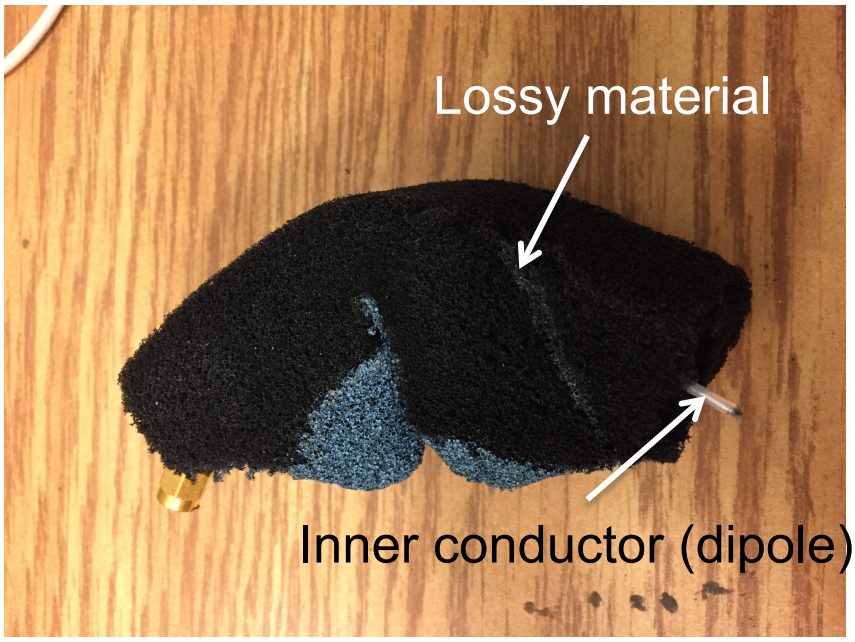

Fig. 2–16 The dipole excitation built by a semi-rigid coaxial cable covered by lossy material.

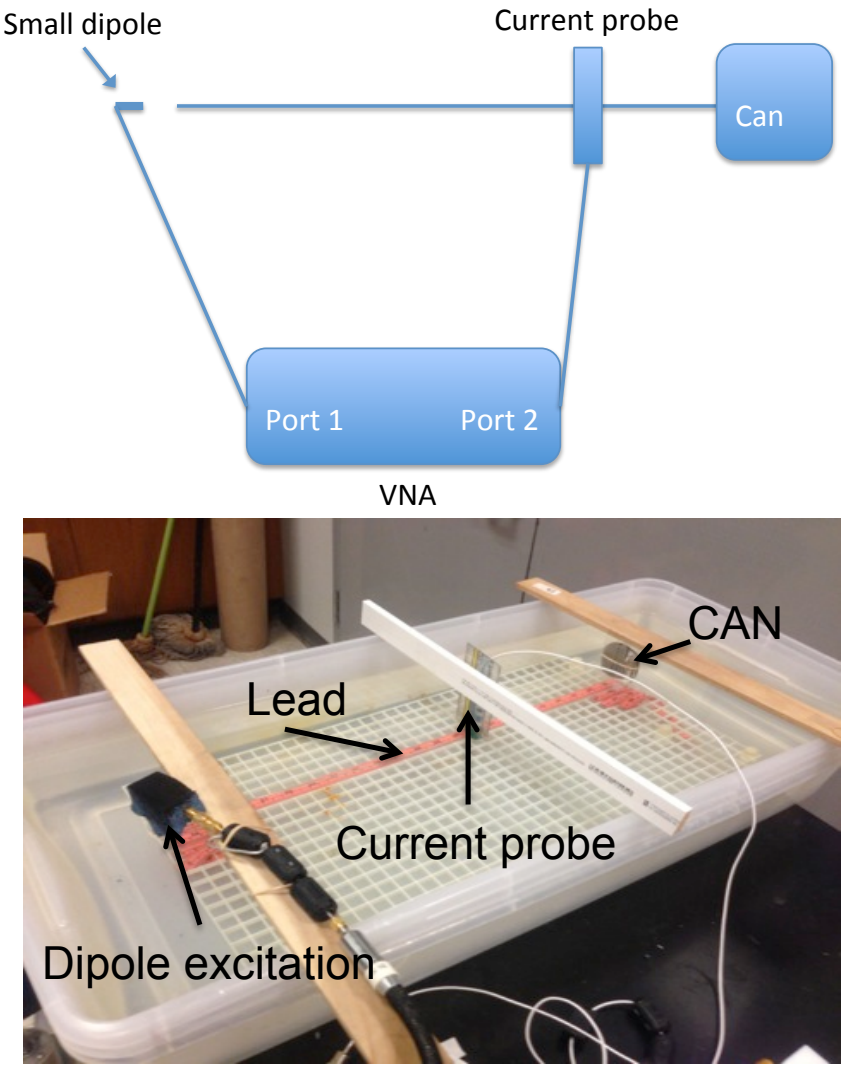

Fig. 2–17 The heating transfer function measurement configuration.

The measurement configuration is shown in Fig. 2–17. Although everything should be immersed in the gelled saline for the heating measurement, the regular saline used in the induced voltage measurement is also used here because only the electric characteristic is matter during the transfer function shape measurement and regular saline has better transparency. The small dipole is connected to VNA port 1 and is carefully located near the lead distal end. A current probe is connected to the VNA port 2 and moves along the lead to record the current distribution on the lead. Similar baluns are set

in the measurement to prevent the unexpected interference. Therefore, we also first measure the transfer function without the scaling factor, and then, evaluate the coefficient. In fact, besides the reason of adding baluns, the heating transfer function cannot be directly measured. A coefficient needs to be determined by performing a direct heating measurement. As a result, we can lump the two coefficients together using the ratio of measure result and predicted result as the coefficient

$$C_T = \sqrt{\frac{\Delta T_{measured}}{\Delta T_{predicted}}}, \tag{25}$$

where C_T is the transfer function scaling coefficient, $\Delta T_{measured}$ is the measured temperature rise, and $\Delta T_{predicted}$ is the temperature rise predicted by the inner product of the un-scaled transfer function and the incident field. This scaling coefficient is also a real number without the phase information, much as the coefficient in the induced voltage transfer functions. Although the temperature rise is predicted indirectly by first evaluating the induced electrical field with phase information, only the magnitude of the electric field affects the temperature rise. Consequently, the scaled transfer function can predict the correct temperature rise.

2.5.2 RF Coil and Control System Operation

All direct measurements in this research are performed with MITS 1.5 system from Zurich Med Tech as shown in Fig. 2–18. This coil can generate the same RF electromagnetic field as commercial 1.5 T MRI scanners. From the control center, many perimeters of the field, such as polarization, pulse type, duty cycle and power level of the RF sequence, can be defined. A pulse type typically used in MITS1.5 system is sinc2. The envelop of the time domain signal and the pulse spectrum is plotted in Fig. 2–19.

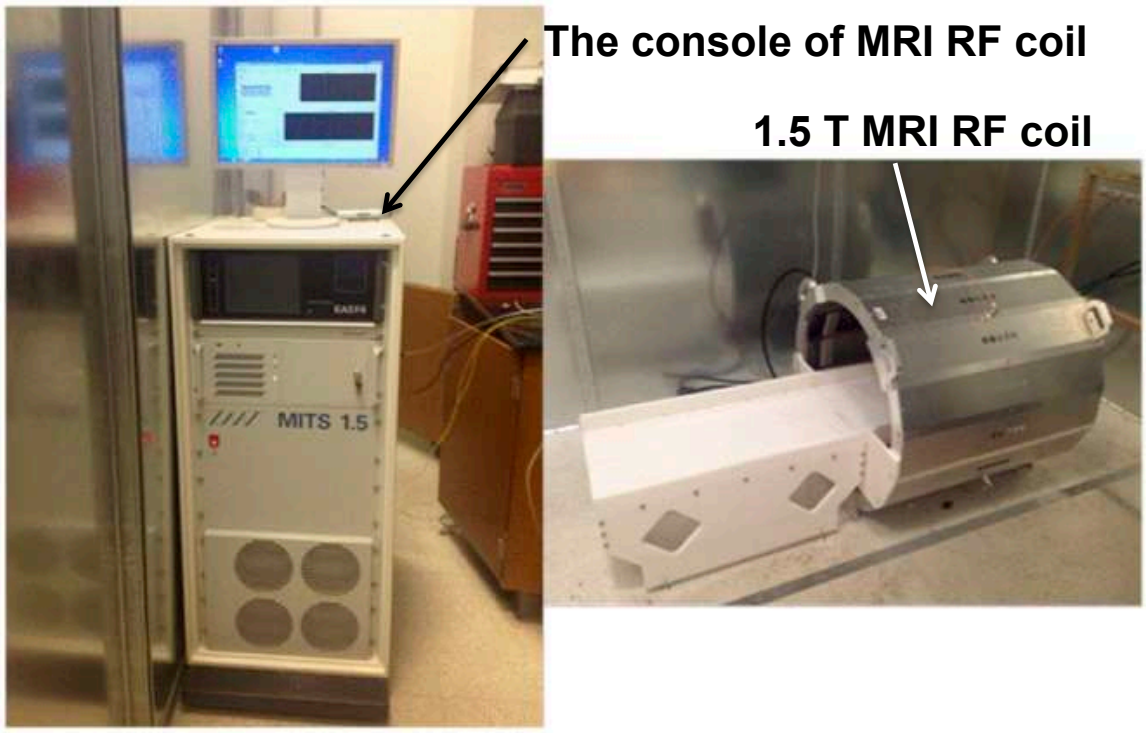

Fig. 2–18 The 1.5 T MRI RF coil and the control console.

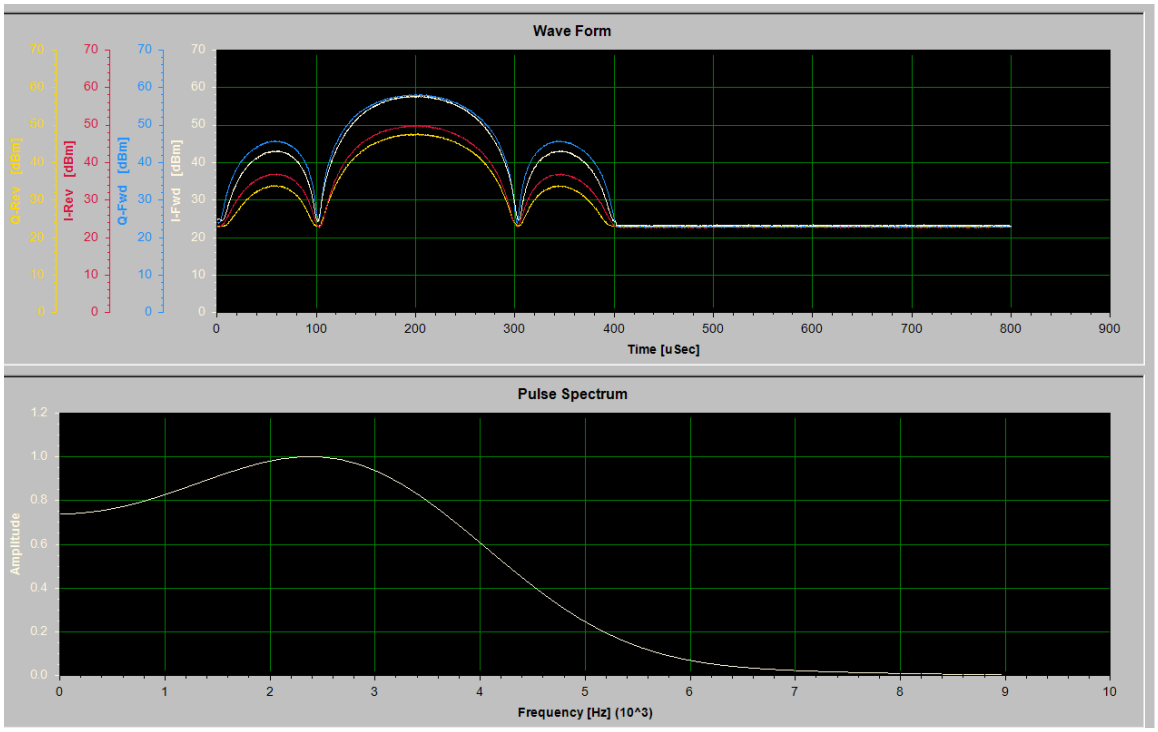

Fig. 2–19 A screen shot from the RF coil control console shows the magnitude and the spectrum of the sinc2 signal envelop.

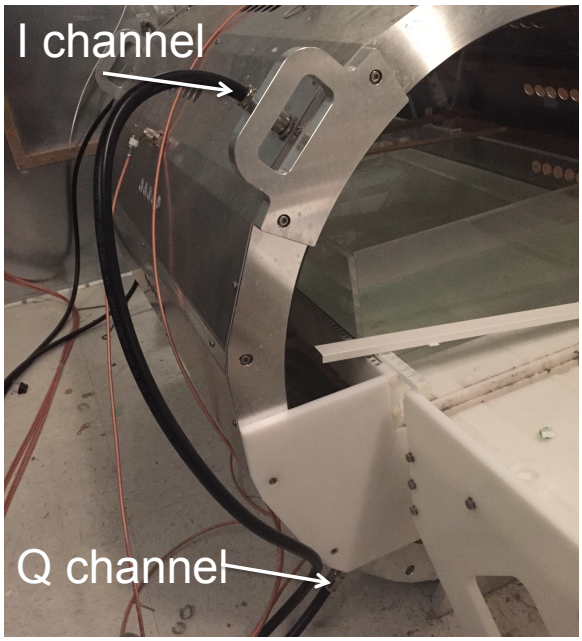

Fig. 2–20 The I/Q feed of the MRI RF coil.


Fig. 2–21 The shielding room made by ETS-Lindgren.

IQ feedings as shown in Fig. 2–20 form a quadrature excitation mode. Before each measurement, a self-calibration program adjusts the magnitude and phase of the two feedings so that the coil resonates at 64 HMz in circular polarization. The RF coil is laid

in a shielding room made by ETS-Lindgren, as shown in Fig. 2–21, to prevent interference between the strong fields generated by the RF coil and other measurement equipment.

It is important to measure the electrical field strength in side the RF coil. Two types of measurement are usually preformed: 1) measurement of a 10 cm rod temperature rise of 15 minutes and 2) measurement of the center magnetic field. The first approach is very common in small medical device thermal measurement, in which only electric field in a small region matters. The temperature rise of a certain location is closely related with the local SAR and the local electrical field. The second approach is more appropriate in our study since we care about the electrical field distribution in a relatively long region. However, measuring of the field strength at every point in the coil is impossible. Instead, field distribution can be extracted from simulation, and only fields at one point or several points are measured. By comparing the fields of several points, electrical field distribution in the RF coil can be scaled from the simulation results. In addition, because the electric field strength is substantial in the side region of the phantom as shown in Section 2.4, electrical field should be measured here to achieve a better signal noise ratio. However, the electrical field changes very rapidly in spatial that could bring a large measurement error. Meanwhile, the magnetic field is strong at the center region with a relatively little spatial variation. Therefore, the magnetic field of the ISO-center region of the coil is measured and compared with the magnetic field at the same location in the simulation. The ratio of two field strengths serves as the scaling factor. A magnetic probe provided by ITIS is used for this measurement as shown in Fig. 2–22. The signal is sent out through a fiber-optical cable. Thus, there is no RF interference from the RF coil.

Fig. 2–22 The easy4 H-field probe.

2.5.3 Induced Voltage Measurement

To determine the transfer function coefficient and validate the predicted result of the transfer function direct measurements are needed. The same modified device CAN as shown in Fig. 2–13 in 2.5.1.1 and the lead are located in the ASTM phantom filled with saline. The saline has a conductivity of 0.47 S/m and a relative permittivity of 80 at 64 MHz. The phantom is placed in the ISO-center of the RF coil as shown in Fig. 2–23.

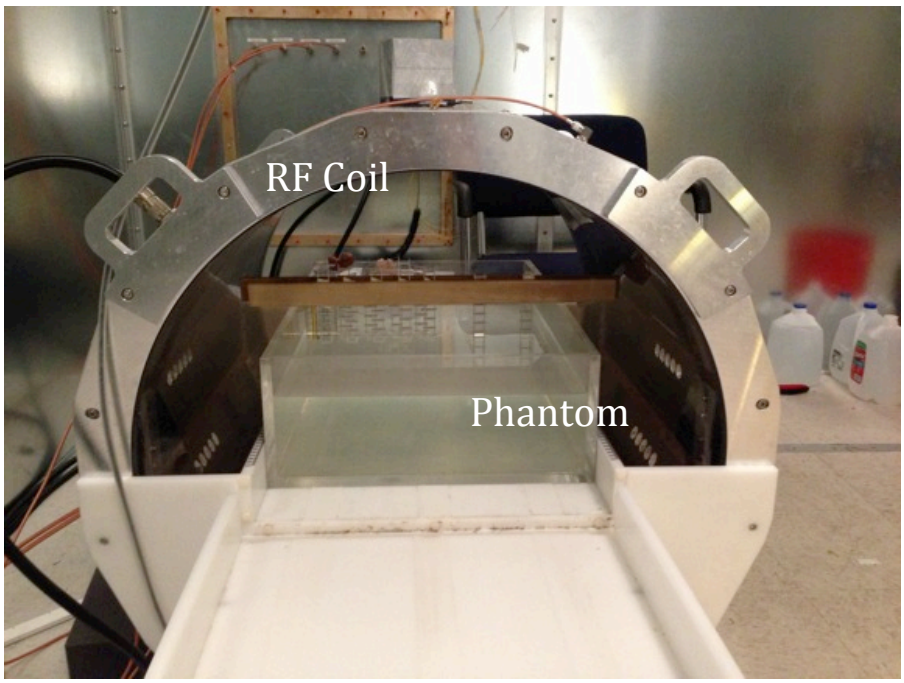

Fig. 2–23 The phantom loaded in the MRI RF coil.

The SMA connector on the device CAN is connected to an oscilloscope to measure the induced voltage between the electros and the shell of the CAN. Several measurement details need to be noticed. First, the RF coil generates a strong electromagnetic field that may directly couple with the coaxial cable and generate a significant measurement error. In order to minimize this interference, a simple balun like to one used in the transfer function measurement is added as shown in Fig. 2–24. Clay covers the whole SMA connector of waterproof. Second, if randomly orientated the device CAN up to 10% relative error on the induced voltage could be generated. To reduce this error, the CAN should be located perpendicular to the electrical field based on the electric field distribution extracted from simulation. In reality, the CAN orientation generating the minimum induced voltage is found by manually rotating the CAN for each location. Finally, all measurement equipment is set outside of the shielding room to prevent interference from the RF coil. The distance between the oscilloscope and the measured device CAN is about two meters. A very long coaxial cable, which should not change the port impedance of the CAN or the transfer function as well as the induced voltage, is used here. Unlike the VNA with 50 Ohm input impedance, which matches the impedance of a standard coaxial cable, the oscilloscope has very high input impedance. Therefore, the input impedance changes periodically along the cable. The period is a half wavelength of the signal, which is 1.48 m for a 64MHz signal with a relative dielectric of 2.5. The total length of the coaxial cable and the simple balun approximates 2.96 m. The input impedance at the port is $371 + j50$ Ohm measured by the VNA, which is a significant larger impedance than the pacemaker impedance between electros and the shell of the CAN at 64 MHz.

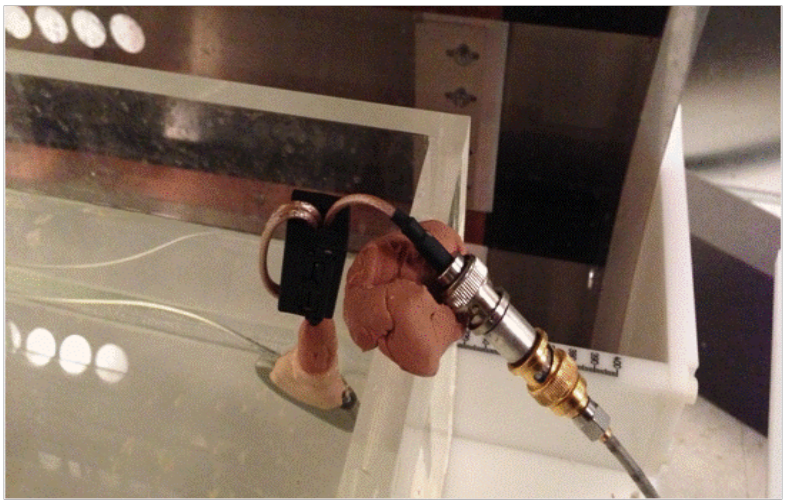

Fig. 2–24 A pacemaker device CAN in the phantom is connected through a simple balun.

Besides normal induced voltage measurement in which only the magnitude of the induced voltage is recorded, the phase information is also required for the fast transfer function estimation proposed in 2.3.4. To capture the phase information of the induced voltage, a reference signal is necessary. A second coaxial cable connected with a copper sheet is fixed to a certain place on the MRI RF coil. The signal received from this copper sheet is treated as a reference. The phase difference between the measured induced voltage waveform and the signal waveform from the copper sheet is recorded as the phase of the induced voltage.

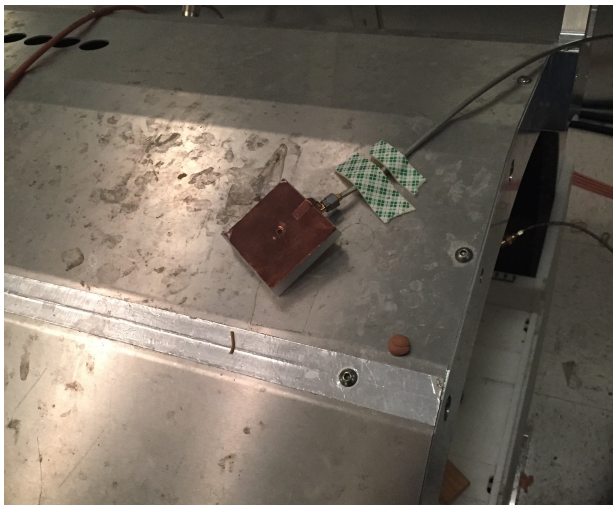

Fig. 2–25 A copper sheet is fixed on a certain place on the RF coil shield.

2.5.4 Thermal Measurement

To obtain an observable temperature rise, we use a gelled saline, which has the same electrical parameters as the saline used in induced voltage measurement with a relative permittivity of 80±20% at 64 MHz and a conductivity of 0.47±10% S/m. The difference between the gelled saline and the regular saline is the fluidity. The poor fluidity of gelled saline leads to a diffusivity of about 1.3×10^{-7} m^2/s, which is desirable for thermal measurement because the heating due to a local SAR is confined to a small region, which causes an observable temperature rise. The procedure of mixing the gelled saline is as follows: 1) add NaCl to water to achieve a concentration of 1.32g/L so that the conductivity is 0.26±10% S/m measured at a frequency lower than 15 KHz; 2) add polyacrylic acid (PAA) and stir to suspend completely; 3) after one hour, blend the suspension into a slurry using a kitchen grade immersion blender with a blade for at least 20 min; 4) after 24 hours verify that the conductivity is 0.47 ± 10% S/m at a room temperature of 20 to 25 °C. The formed gel is shown in Fig. 2–26 with dimensions marked in mm.

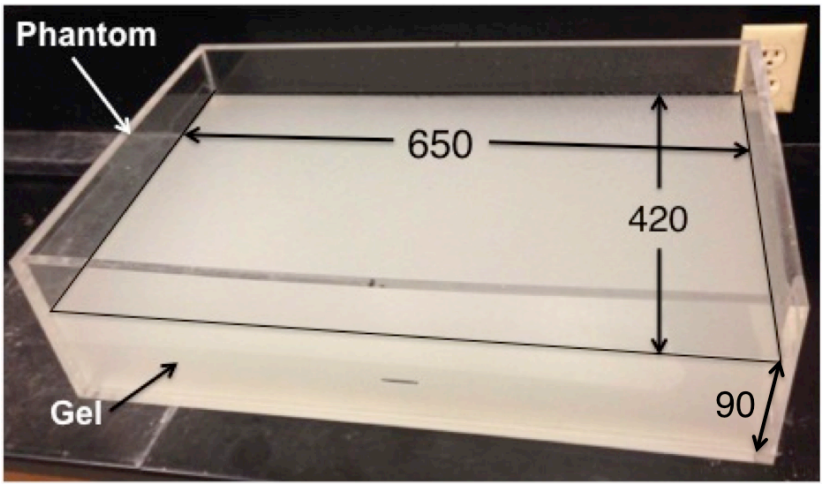

Fig. 2–26 Mixed gelled saline in the rectangular ASTM phantom.

Fiberoptic temperature probes from Neoptix are used to record the real temperature rise for all thermal measurements. Our thermometer has four channels as shown in Fig. 2–27. The T2™ probe consists of a 300-micron O.D. solid-state sensitive element bonded to an optical fiber covered with a 1.06 mm O.D. oil-permeable protective PTFE Teflon sheath. The entire probe is protected by a 3.1 mm O.D. PTFE "spiral wrap" reinforcement. Only chemically resistant and low dielectric constant materials are used for these temperature probes. The T2™ temperature range is -80ºC to +200ºC with ±1°C accuracy.

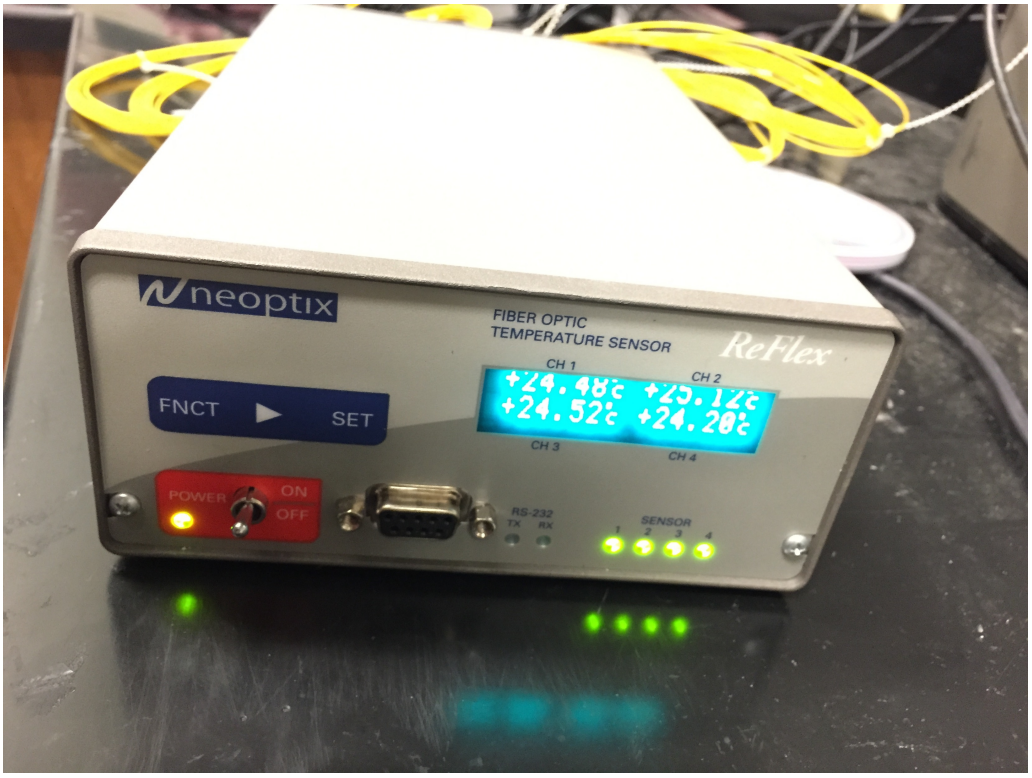

Fig. 2–27 The thermometer with four channels from Neoptix.

During the measurement one temperature probe is tied to the lead. The head of the probe is fixed as close as possible to the lead distal end as shown in Fig. 2–28 since the highest temperature rise always happens at the tip electro due to its sharp shape. Another probe is fixed at the symmetric location of the first probe in the phantom as the reference.

Because the incident electrical field in the phantom has a symmetric distribution, the temperature rise due to the directly incident field is the same at two symmetric locations. Therefore, differences in the temperature rises measured by two probes are the temperature rise due to the lead structure.

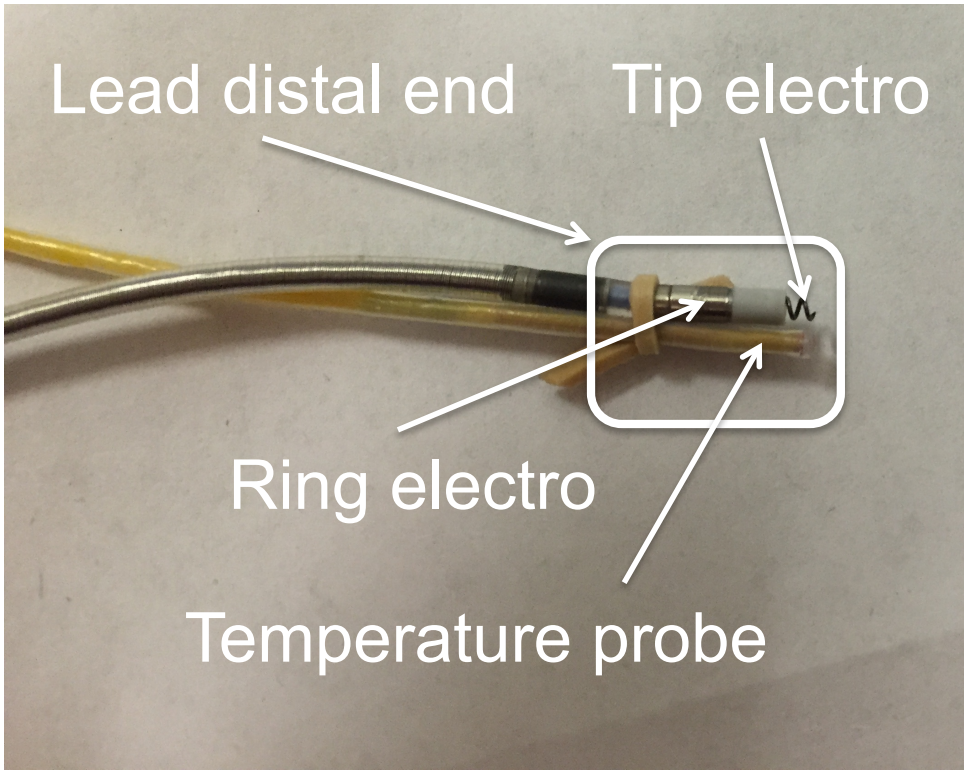

Fig. 2–28 A temperature probe is tied to a lead distal end to measure the temperature rise.

Chapter 3 Numerical and Experimental Results

To validate our proposed approach, both numerical modeling and experimental measurements are used. In both approaches, the transfer function should be obtained first through either simulation or measurement. The incident fields along different lead paths are then obtained through simulations. The transfer functions are integrated with the incident field to obtain the induced electric field. Because typical pacemaker leads have very complex structures, it is not possible to obtain their transfer functions via simulations. Therefore, in the numerical modeling results, only simple straight wires are used to demonstrate the effectiveness of our approach. Experimental measurements are performed on other lead structures.

3.1 Induced Electric Field Transfer Functions of Thin Wire Leads

In this section, the simplest lead structure is studied both numerically and experimentally. First, to validate our measurement configuration, a transfer function of 42 cm lead is carefully measured and simulated using the reciprocity approach. In simulation, a small electric dipole source is placed at the lead distal end as the excitation. Due to the conductivity loss of gel, the electric field decays very rapidly away from the metallic lead. This implies that it is actually not necessary to include the MRI RF coil and the full ASTM phantom in this step. In our study, the simulation domain is reduced to a rectangular solid containing the same saline material with a size of only 18 cm × 18 cm × 90 cm. The Perfectly-matched-layer (PML) boundary conditions are applied on its six sidewalls to truncate the FDTD simulation domain. The current is calculated using $I = \oint \underline{H} \cdot \underline{dl}$ on a close loop around the lead cross-section. The measurement is performed

as described in Section 2.3.3. The current is recorded every 2 cm. The magnitude and phase of the transfer function are plotted in Fig. 3–1. The relative error of the magnitude and the difference between the two phases are shown in Fig. 3–2.

Based on the plots, the transfer function magnitudes from simulation and measurement closely align, except the last few points where the simulated transfer function approaches zero, meanwhile the measured transfer function remains a small value due to the noise and the sensitivity of the current probe. The phase difference is in the range of ±10°. In the reciprocity theorem, the magnitude of the dipole moment should be equal to 1 Am, which means the current strength is about 2000 A on a 0.5 cm dipole. A normal current output from a VNA is on the order of mA or even smaller. As a result, the absolute value of the current on the lead during the measurement is extremely small, even smaller than the noise level or the sensitivity of the current probe. However, this only happens where the transfer function is particularly very small. It also won't bring significant error into the prediction of the induced voltage or temperature rise if the small value only appears at several points or a short segment because the induced voltage or the temperature rise are the integral of the transfer function and the incident field. In the sense of induced voltage or heating prediction, the measured transfer function matches the simulated transfer function very well.

To validate the simulated transfer function, a series simulation is performed. Four different lead lengths are evaluated: L1 = 43.5 cm, L2 = 28.5 cm, L3 = 13.5 cm, and L4 = 58.5 cm, respectively. The simulated magnitude and phase of the transfer functions are plotted in **Fig. 3–3**.

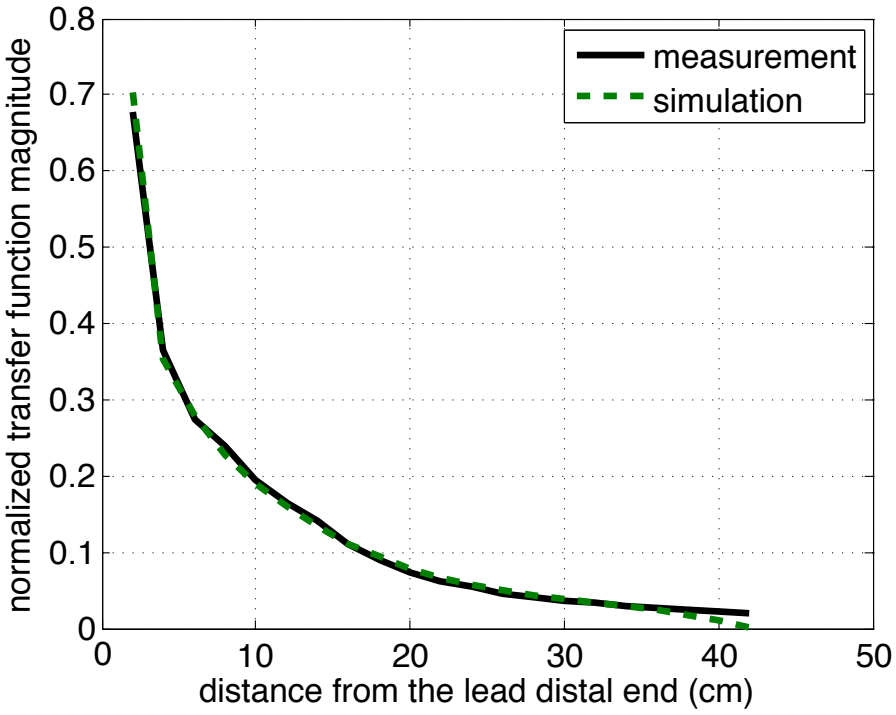

(a) Magnitude

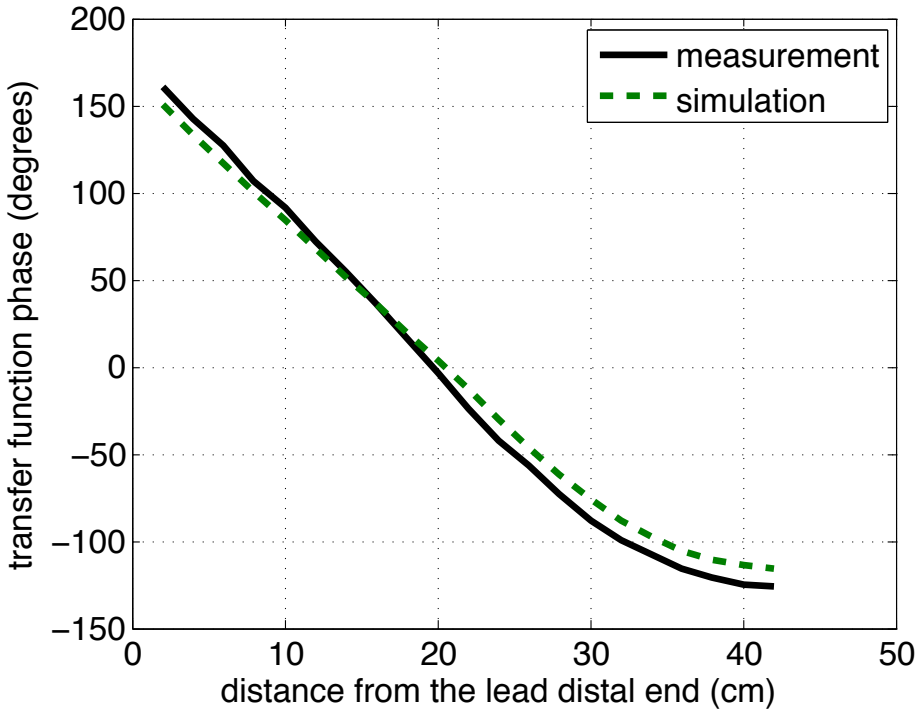

(b) Phase

Fig. 3–1 The measured and simulated transfer functions of a 42 cm thin wire.

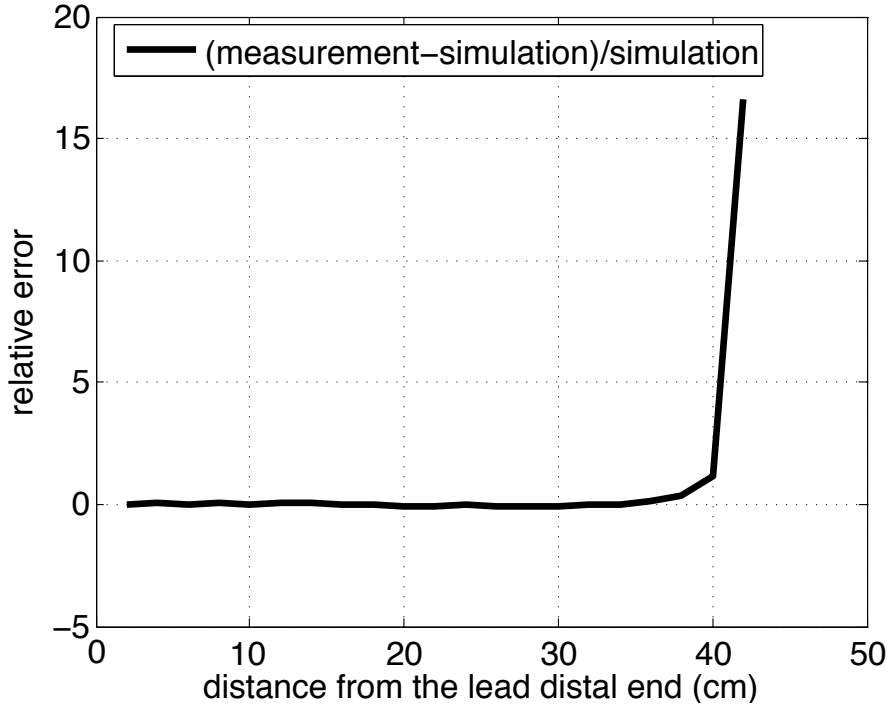

(a)

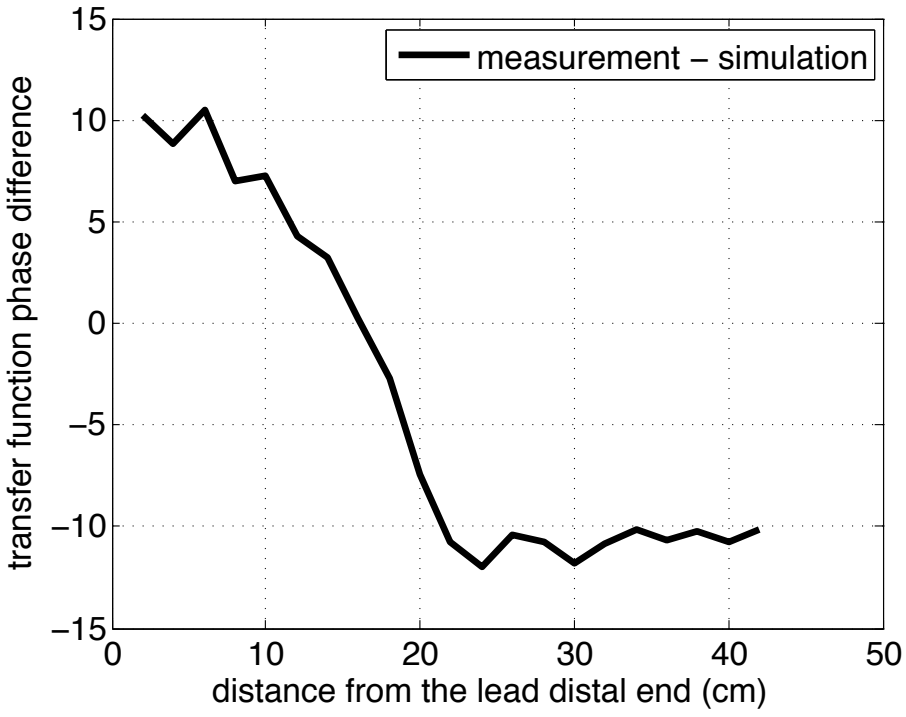

(b)

Fig. 3–2 (a) The relative error of the measured transfer function magnitude and (b) the phase difference between measured and simulated transfer function.

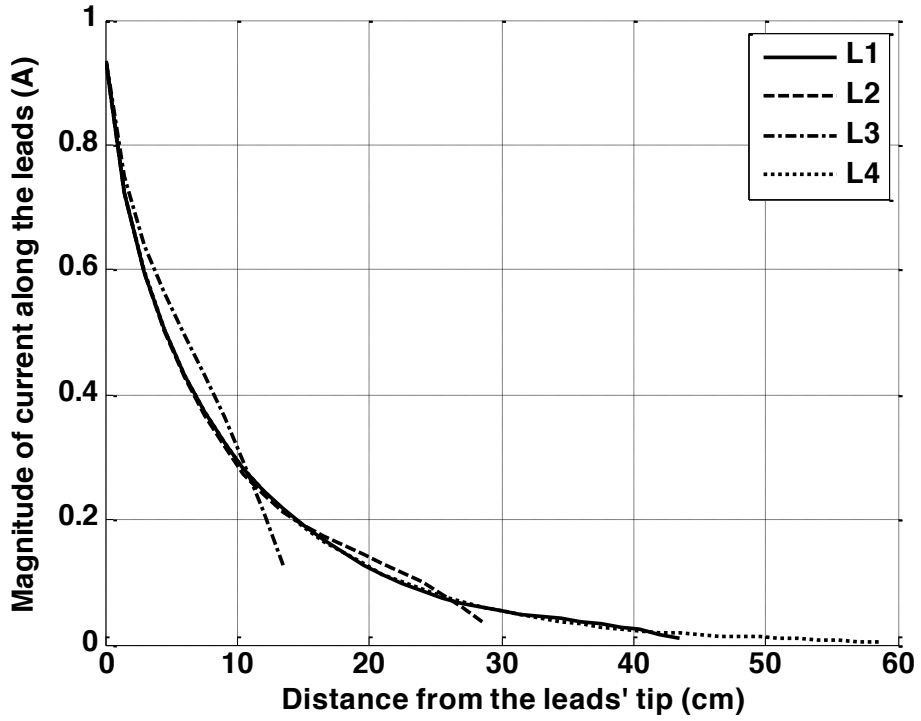

(a) Magnitude

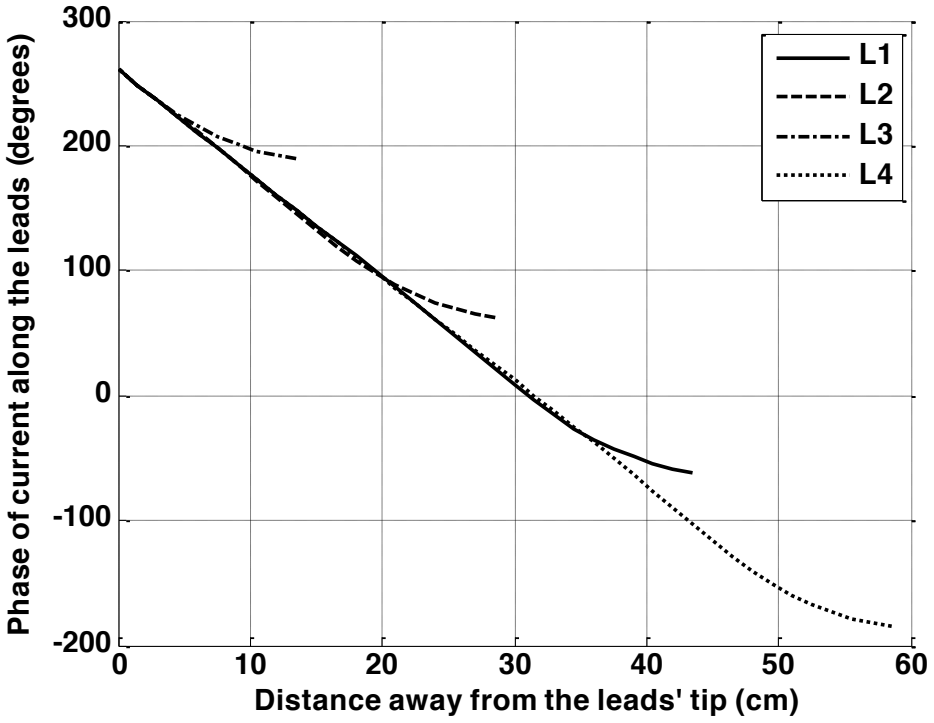

(b) Unwrapped phase

Fig. 3–3 The simulated transfer function on the straight thin wire leads for four different lengths.

Once the transfer functions are obtained, the incident fields along different pacemaker lead paths are evaluated. The incident field is extracted from a simulation with the MRI RF coil and the phantom with head described in 2.4. The electric field obtained in this step is regarded as the incident field $\underline{E}_{inc}$ in equation (10).

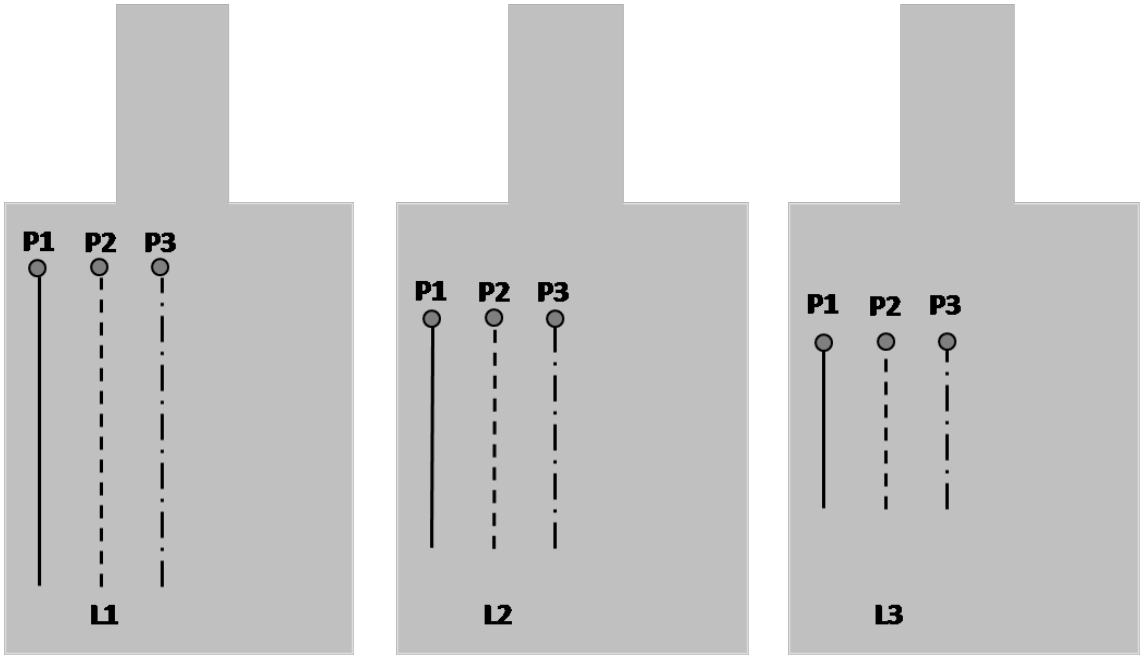

(a) (b) (c)

Fig. 3–4 The straight leads are put into the phantom at three positions (distance to the left border: P1 = 4.5 cm, P2 = 12 cm and P3 = 19.5 cm).

In the rest of the section, eight different lead trajectories are studied to validate the transfer function from the reciprocity approach simulation. First, three straight lead paths as well as three different lead lengths, L1, L2, and L3 as shown in **Fig. 3–4** are investigated. The first lead path is vertically placed in the phantom 4.5 cm (P1) away from the left side of the phantom. The second and the third leads (P2, P3) are moved 7.5 cm and 15 cm toward the center of the phantom as shown in **Fig. 3–4**. For each position and length, $\underline{E}_{end}$ (denoted in **Fig. 3–4** as a circle) is estimated using the transfer function shown in **Fig. 3–3** together with the incident electric field $\underline{E}_{inc}$ shown in Fig. 2–10(c)(d)

using equation (10). For validation we compare our method with the conventional FDTD method to directly calculate $\underline{E}_{end}$ for all nine cases. In these direct calculations, non-uniform meshes must be used. In the vicinity of the wires, the mesh size is on the order of millimeters. The mesh size increases for the regions that are away from the wire in order to make the problem solvable on regular computers. The maximum mesh size here is limited to 10 mm.

Table 3-1 Comparison of simulated $\underline{E}_{end}$ of straight line.

		$\underline{E}_{end}$ (V/m) / relative error (%)		
		P1	P2	P3
L1	Direct	589	361	66
	Reciprocity	594 / 0.74	361 / 0.04	65 / 1.2
L2	Direct	807	477	79
	Reciprocity	777 / 3.7	467 / 2.1	80 / 1.7
L3	Direct	983	623	106
	Reciprocity	983 / 0.0	598 / 4	103 / 2.8

Comparisons are given in Table 3-1. The maximum error is only 4%. By further inspection for all groups, the largest induced electric field is always at the P1 location and the smallest induced electric field is always at the P3 location. This phenomenon has been confirmed by the measurements in Fig. 4a and Fig. 5a-c in [14] and can be explained by inspecting the right side of (10). Considering current distributions identical wherever the trajectories are, the tip electrode field relies only on the strength of the local incident field. In Fig. 2–10 in 2.4, the electric field polarized along the vertical direction has the minimal values in the center region of the phantom. Therefore, the inner product of this low incident field with transfer function produces the smallest $\underline{E}_{end}$ value at P3. Finally, Table 3-1 shows that the shortest line L3 generates a greater electric field than

those from L1 and L2. This indicates that the longer lead does not necessarily generate greater $\underline{E}_{end}$ due to a possible phase cancellation effect.

The second set of leads configuration considered here involves bending the upper and lower one-thirds of straight lead L_1 in **Fig. 3–4**(a) into horizontal directions to form a U-shape line as shown in **Fig. 3–5**a. In **Fig. 3–5**b, we extend the lead at P3 position in **Fig. 3–5**a by 15 cm towards the shoulder region of this phantom to make it longer.

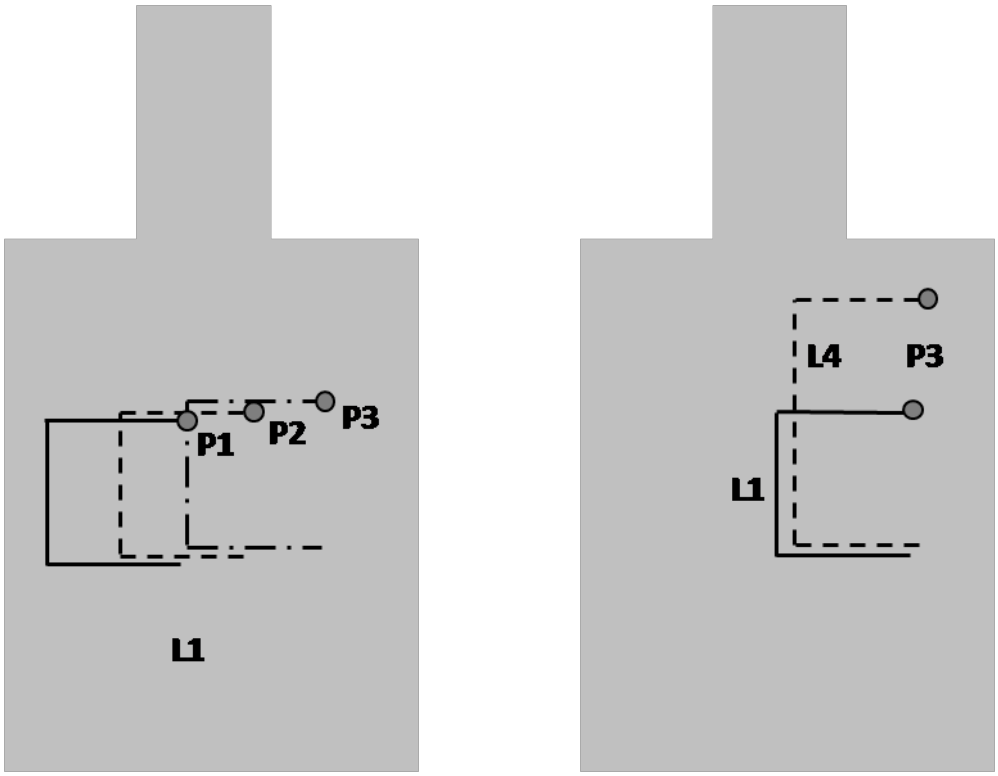

(a) (b)

Fig. 3–5 The straight leads are put into the phantom at three positions (distance to the left border: P1 = 4.5 cm, P2 = 12 cm and P3 = 19.5 cm).

Table 3-2 Comparison of simulated $\underline{E}_{end}$ of the U-shape leads, L1 and L4.

	$\underline{E}_{end}$ (V/m) / relative error (%)			
	L1, P1	L1, P2	L1, P3	L4, P3
Direct	437	301	211	744
Reciprocity	425 / 2.8	303 / 1.5	222 / 5.2	743 / 0.2

Again $\underline{E}_{end}$ is calculated by both direct simulation and reciprocity approach, and the results are shown in Table 3-2. Although the induced $\underline{E}_{end}$ on L1 at P3 has the smallest value due to very small $\underline{E}_{inc}$ over that area, changing its length by only 15 cm produces a much higher field in Table 3-2. This is due to the field pattern in Fig. 2–10(c)(d). The top shoulder region has a very strong horizontal direction of $\underline{E}_{inc}$ to interact with transfer function.

3.2 Induced Voltage Transfer Functions of Coaxial Lead and 4-Wire Lead

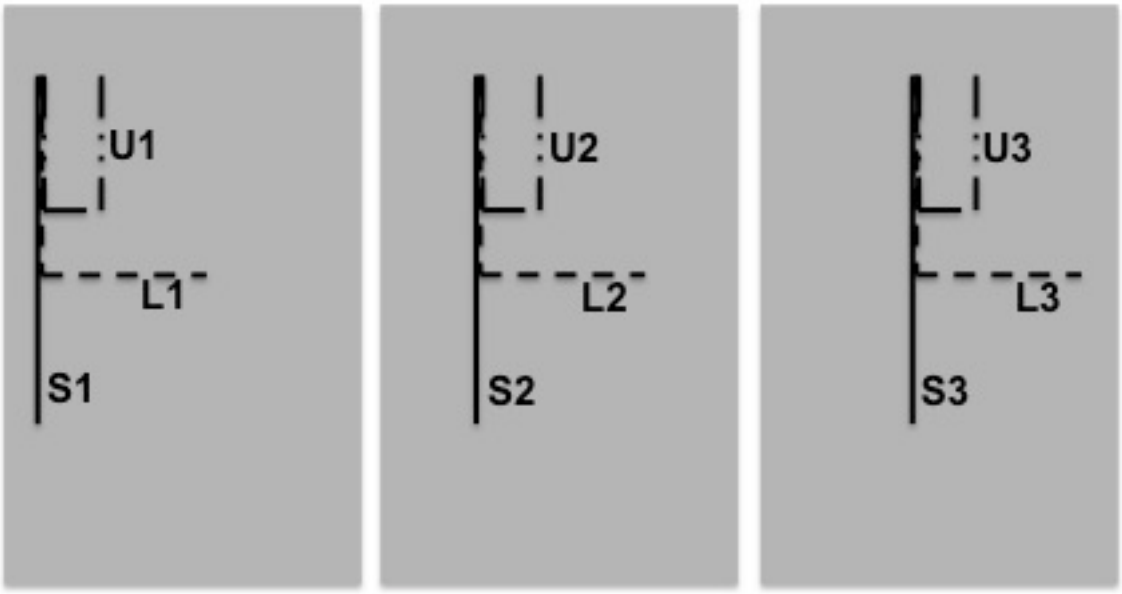

(a) (b) (c)

Fig. 3–6 Illustration of nine different trajectories for validation test (distance to the left border: S1, L1 and U1 are 2 cm; S2, L2 and U2 are 6 cm; S3, L3 and U3 are 10 cm.

In this section two types of lead structures are investigated experimentally. The induced voltage transfer function of the coaxial lead and 4-wire lead are measured. The induced voltages on different trajectories are predicted and directly measured, and the results are presented and compared.

The lead paths used to validate the result here are shown in **Fig. 3–6**. One set of lead paths is parallel to the phantom sidewall along the z-direction, and the other two lead path sets are U-shaped and L-shaped paths to emulate conventional pectoral insertion and the sub-clavian lead insertions. Each set of lead paths consisted of three different offsets in the described configuration. We use the rectangular phantom here because it is easier to perform the directly measurement in it. The incident electric field distribution shown in Fig. 2–10 in 2.4 is extracted from simulation.

The four-wire cable investigated in this study is shown in **Fig. 3–7**. The length of each wire is 48 cm. Each wire is insulated from each other and encapsulated inside an outer insulator. A 3.6 Ohm resistance is connected at one end of the cable between the two leads to model the pacemaker device CAN impedance. An SMA port is also connected to pick the induced voltage. The waterproof clay covers both the SMA port and the resistance. The objective quantity is the induced voltage on the SMA port, namely the induced voltage on the 3.6 Ohm resistance.

The transfer function (total current distribution) of the four-wire cable is shown in Fig. 3–8. The transfer function obtained here is substituted into equation (6) together with the incident fields along nine different trajectories to estimate the induced voltage. Direct measurement is also performed by placing the four wires leads inside the ASTM phantom along the nine trajectories shown in **Fig. 3–6**. Fig. 3–9 shows the comparison between the directly measured and predicted results, which are closely aligned. The largest induced voltage is approximately 0.5 Volt on the S1 trajectory. The percentage error of the induced voltages on all trajectories is less than 20%.

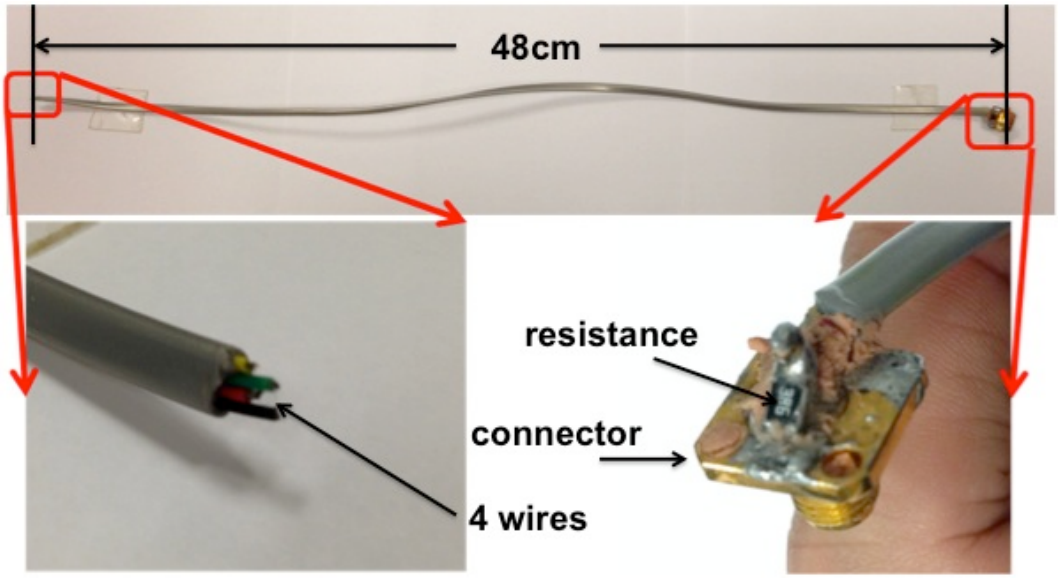

Fig. 3–7 The geometry and connector for the four-wire cable.

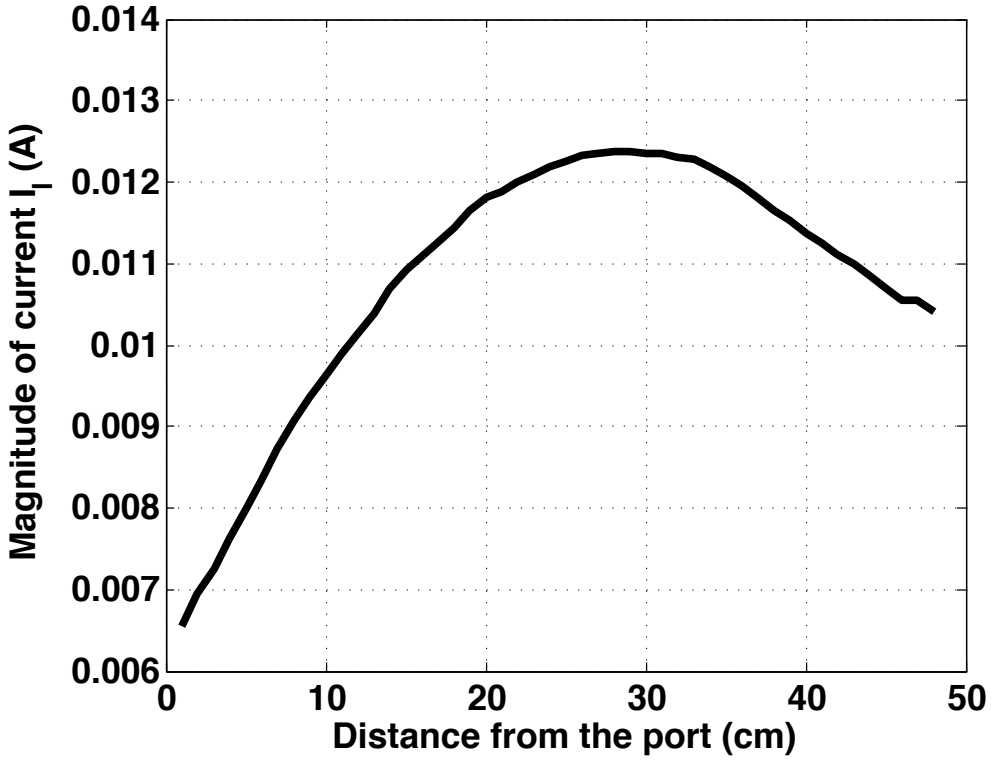

(a) Magnitude

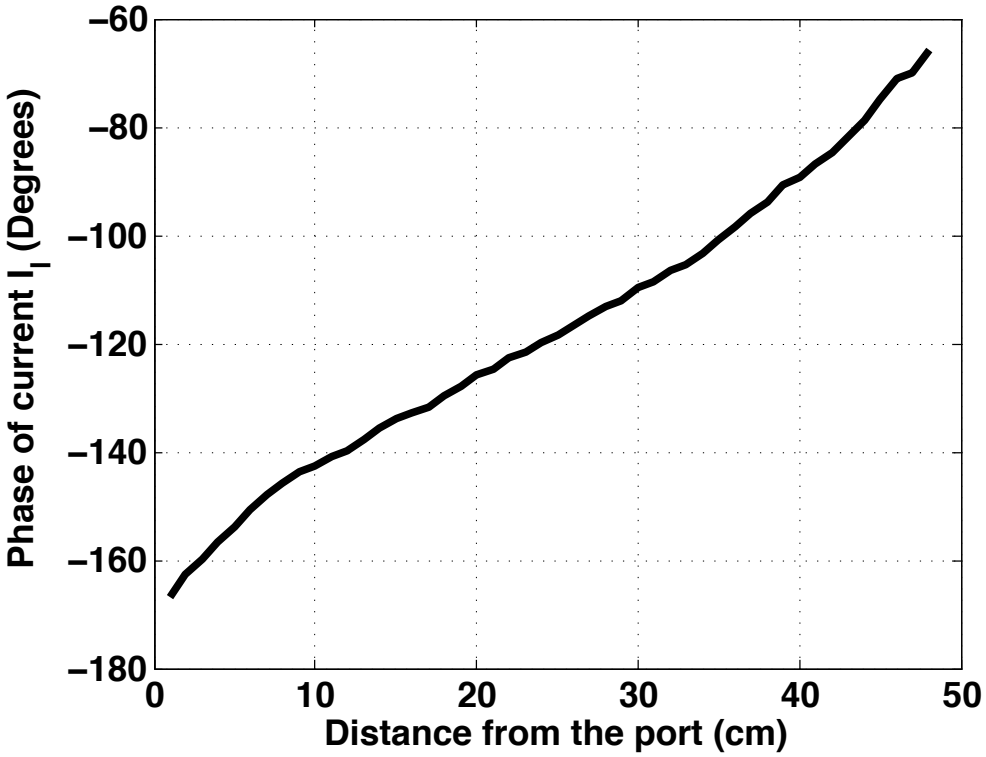

(b) Phase

Fig. 3–8 The transfer function of the four-wire cable.

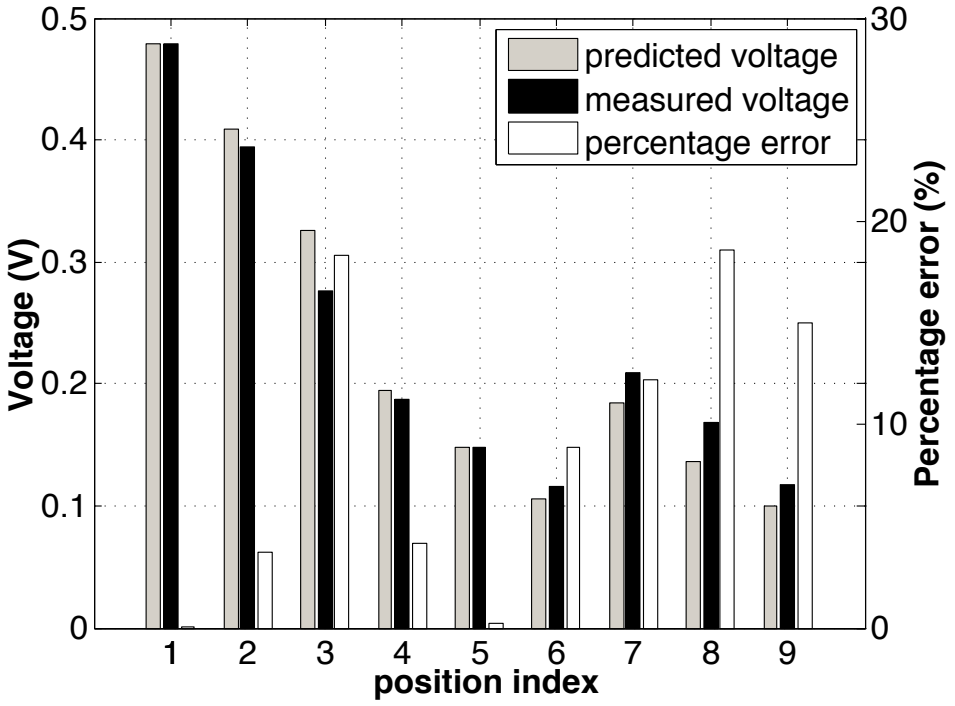

Fig. 3–9 The comparison between induced voltage from direct measurement and induced voltage predicted from transfer function for the four-wire cable.

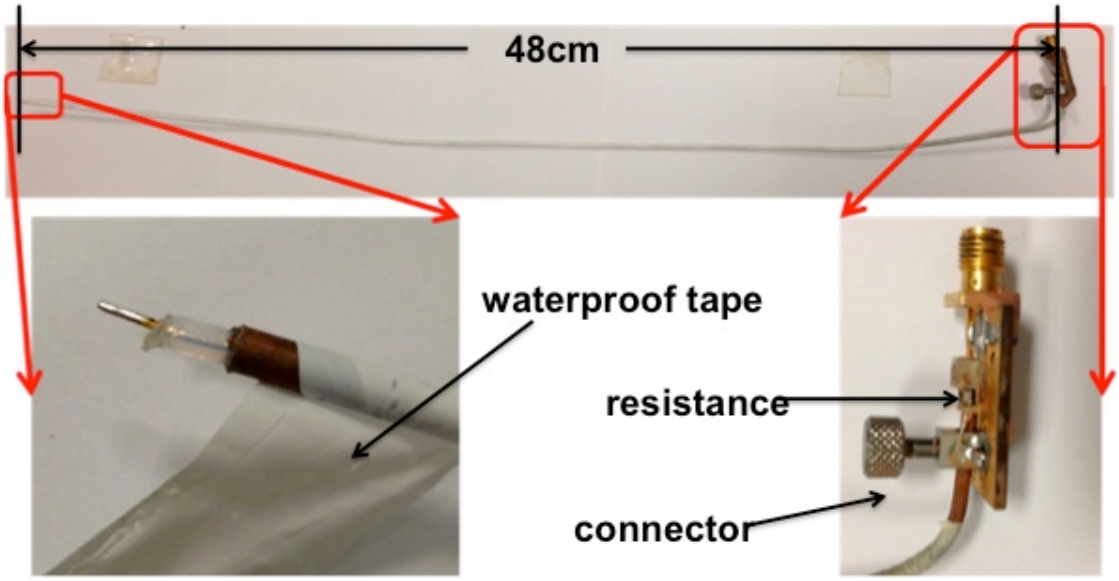

Fig. 3–10 The coax cable covered by a waterproof tape.

In the second measurement validation, the induced voltage between the inner and outer conductor of a coaxial cable is studied as shown in Fig. 3–10. As in the four-wire cable test, the length of the coaxial cable is 48 cm. To model the pacemaker that lead which usually is covered by a plastic layer, the entire coaxial cable is covered by waterproof tape. The outer conductor is left off at one end of the coaxial cable; the other end of the coaxial cable is connected to an SMA port. A 3.6 Ohm resistance is also connected between the inner and outer conductor to emulate the pacemaker device CAN impedance. The SMA connector and the resistance are covered using clay during the measurement under the saline.

The transfer function of the coax structure is shown in Fig. 3–11. The same phantom and the pathway are used. Therefore, the same incident field is applied to the coaxial cable. The magnitude of the coaxial cable is larger than magnitude of the four-wire lead transfer function. However, the phase here has a faster variation, which may cause some cancellation effect. Therefore, the calculated induced voltage is close to the induced voltage of four-wire lead.

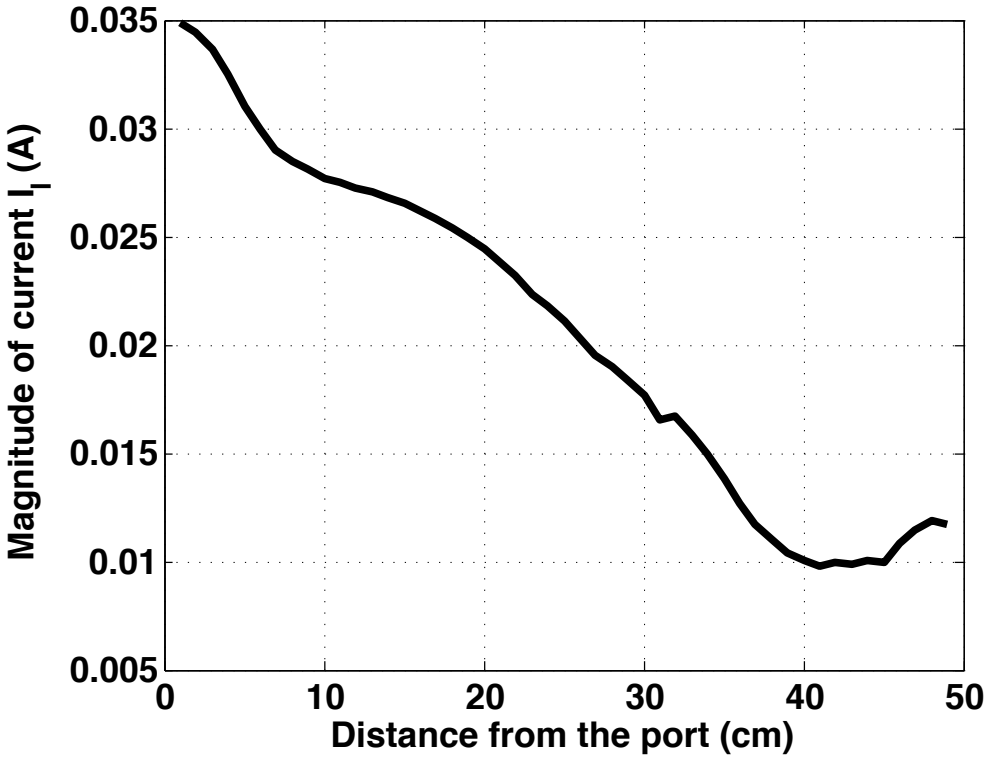

(a) Magnitude

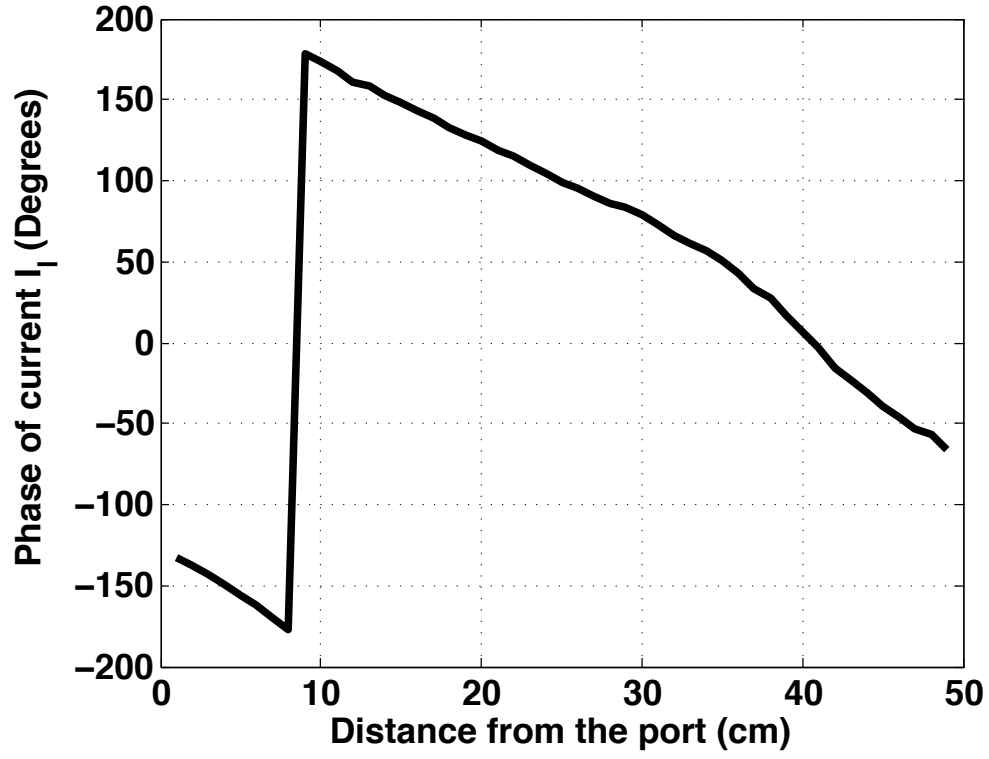

(b) Phase

Fig. 3–11 The transfer function of the coax cable.

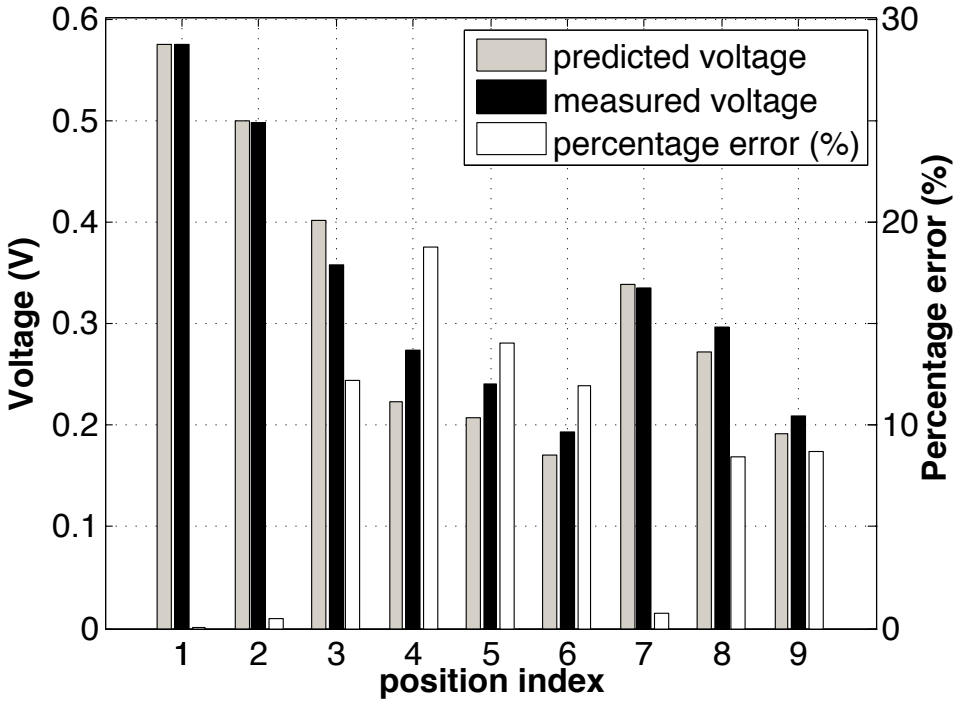

Fig. 3–12 The comparison between induced voltage from direct measurement and induced voltage predicted from transfer function for the coax.

Fig. 3–12 shows the comparison between the measured and predicted induced voltage of the coaxial cable from different trajectories. As show in the figure, the largest induced voltage appears with the S1 trajectory. All induced voltages for the nine trajectories are consistent in both measured and predicted result. The percentage error of the induced voltages on all trajectories is less than 20%.

3.3 Transfer Functions of Practical Pacemaker/Defibrillator Leads

Numerous practical pacemaker/defibrillator leads have been measured. Parts of the measured transfer functions are plotted as the example. They are chosen from different lead type. Due to the confidentiality agreement, the model number and name are not mentioned here.

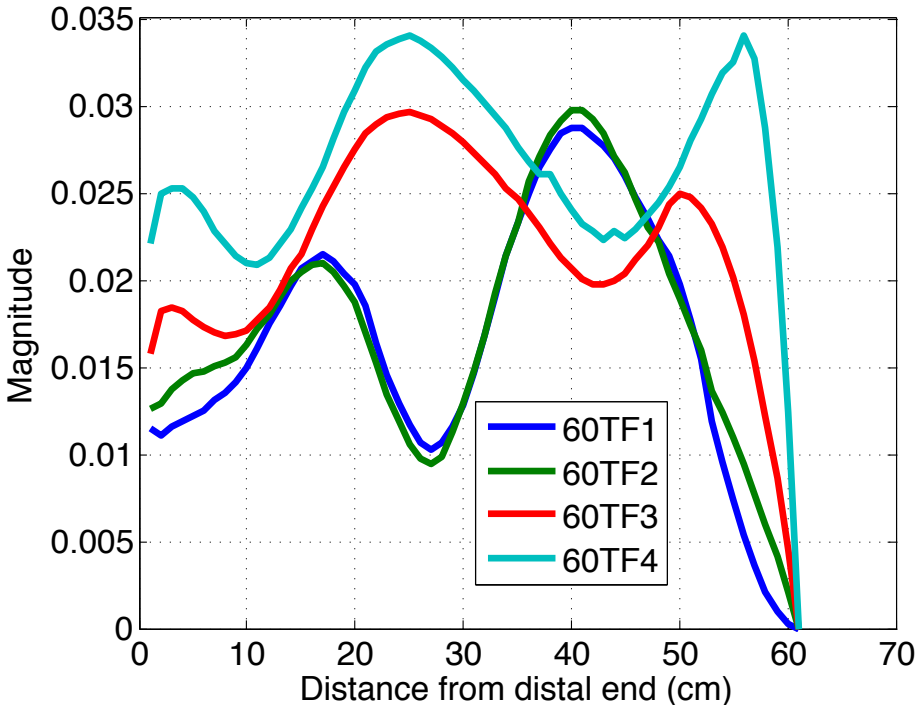

(a) Magnitude and

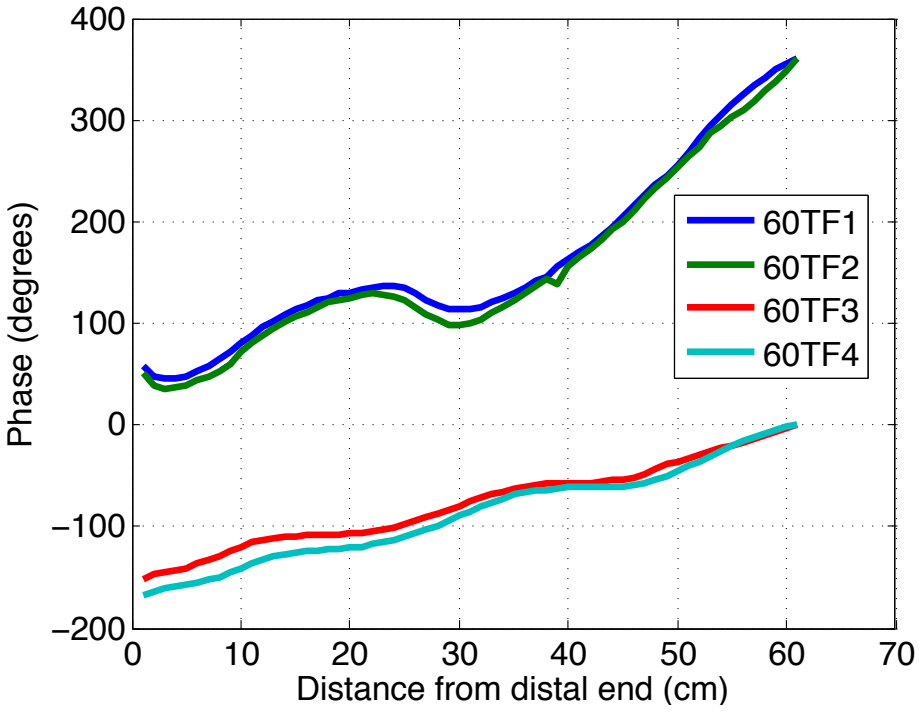

(b) Unwrapped phase

Fig. 3–13 A set of 60 cm pacemaker lead transfer functions.

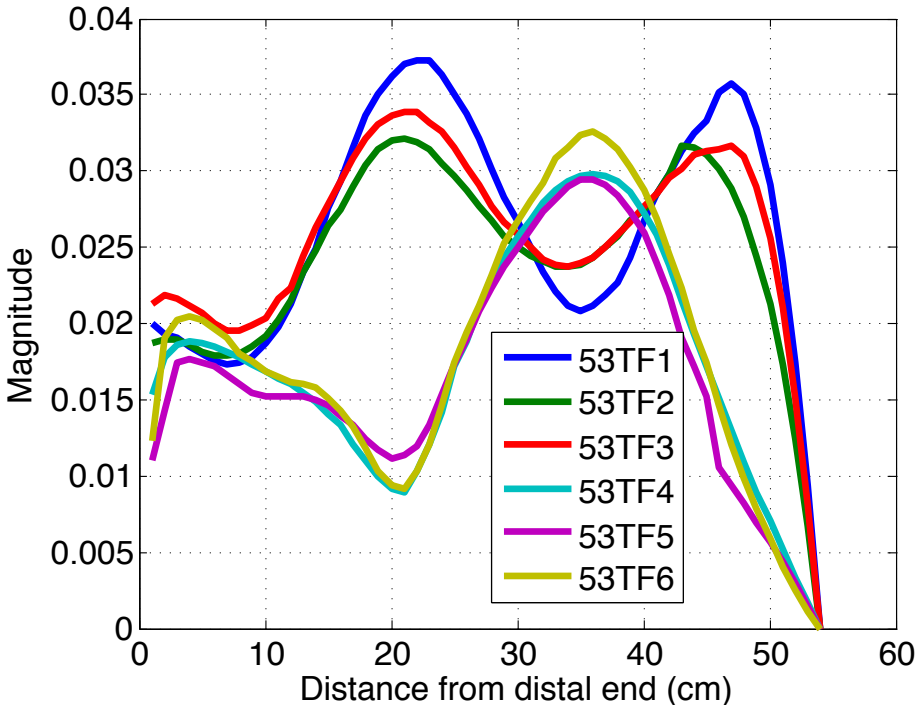

(a) Magnitude

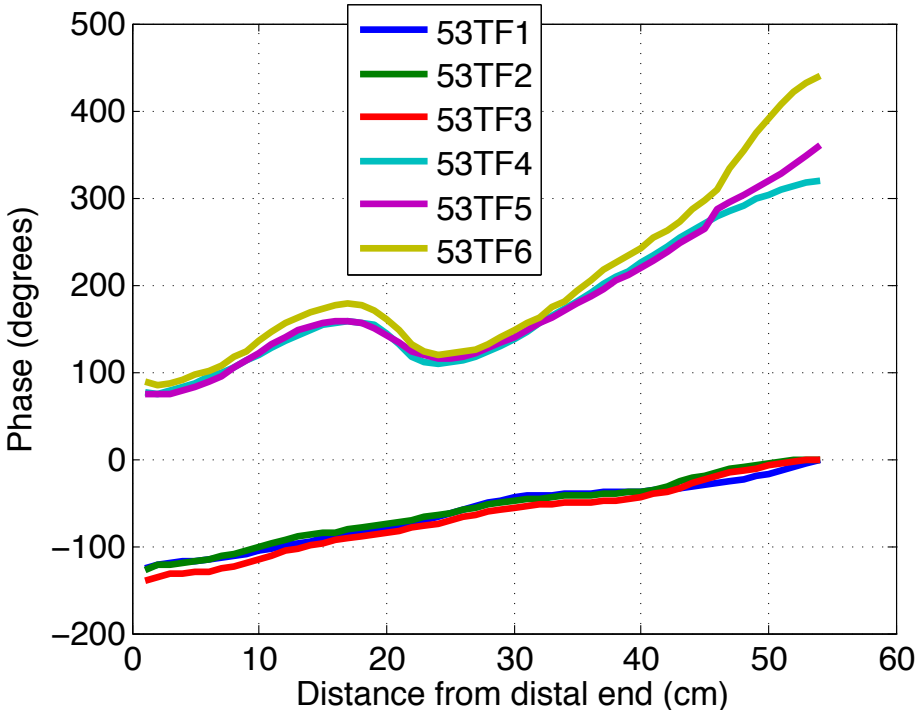

(b) Unwrapped phase

Fig. 3–14 A set of 53 cm pacemaker lead transfer functions.

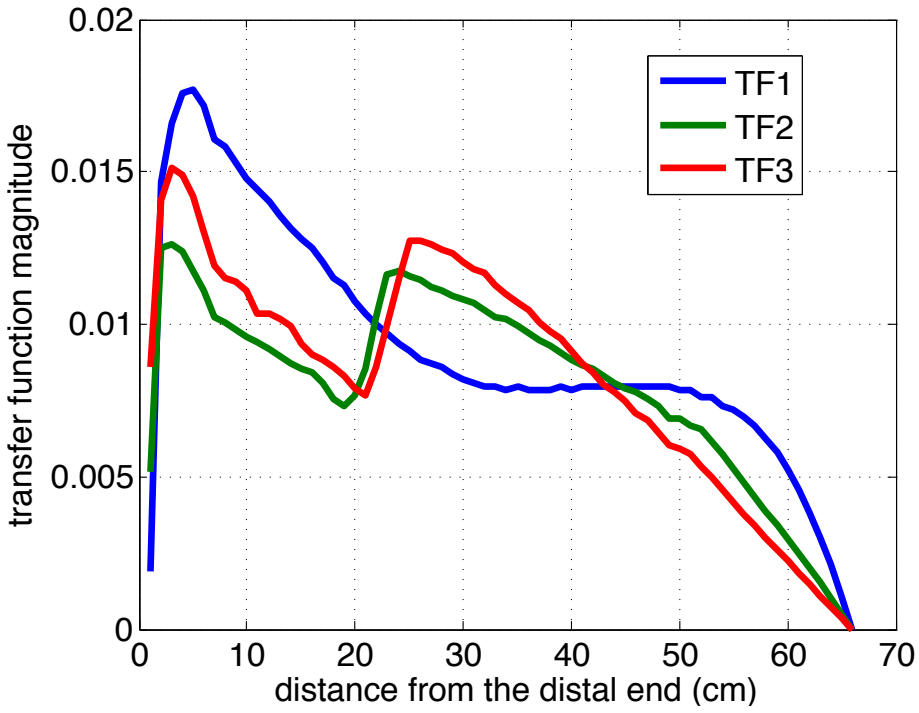

(a) Magnitude

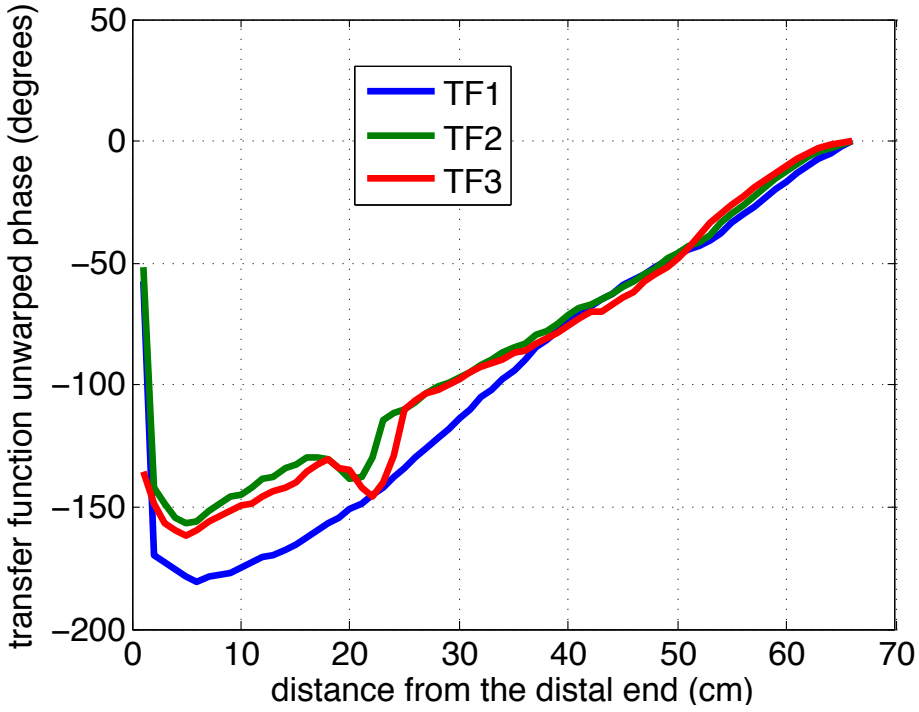

(b) Unwrapped phase

Fig. 3–15 A set of 65 cm lead transfer functions.

Fig. 3–13 and Fig. 3–14 show a set of the 60 cm pacemaker lead transfer functions and a set of 53 cm pacemaker lead transfer functions. For both the 60 cm and 53 cm transfer function, different lead samples but the same lead model are used. The transfer function is clearly separated into different groups for both 60 cm and 53 cm lengths. Different groups correspond to the induced voltage between different electros so that the port impedance is different. In the same group, the transfer functions, which are measured on different lead samples plugged into different pacemaker device CAN channels, are almost identical. The minor difference is caused by the leads sample difference and the measurement uncertainty. These are typical sets of pacemaker transfer functions whose magnitude and phase vary continuously and slowly along the lead.

Fig. 3–15 shows a set of 65 cm defibrillator lead transfer functions. Different lead types of the same length are measured here. Three transfer functions are used to predict same type of induced voltage on the same channel. Therefore, the end impedance is totally the same. The difference is due to the location of the shocking coil. Because of the discontinuous of the lead structure, the transfer function could change rapidly over a short distance. To capture these changes and measure the transfer function accurately, the measurement resolution in the direction along the lead needs to be high enough. Usually one cm resolution is required to accurately predict the result.

The same discontinuity appears at dual lead transfer functions. Sometimes, a patient requires a dual channel pacemaker to stimulate both atrium and ventricle. Therefore, many dual leads transfer functions are also measured. The two lead lengths in a dual lead system are usually different. In most cases, the two leads are parallel except

for the last several centimeters. Thus, the leads are also tied in parallel during the measurement as shown in Fig. 3–16.

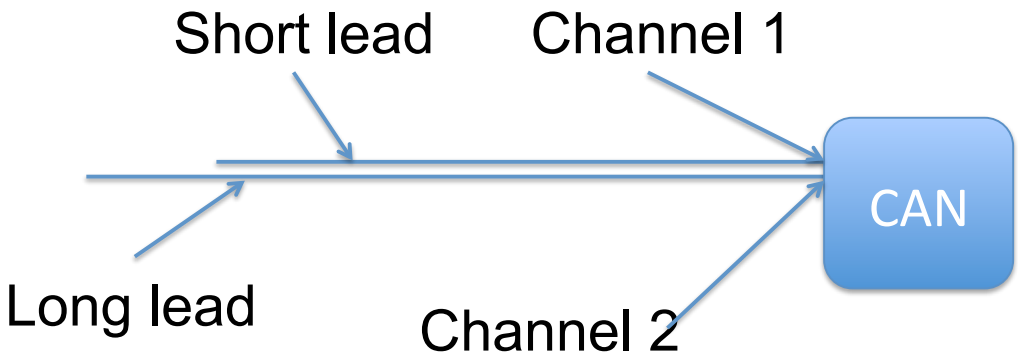

Fig. 3–16 Two leads are laid parallel during the measurement.

We can expect a jump variation when the second lead is in. Several sets of dual leads transfer function examples are shown in Fig. 3–17 and Fig. 3–18. A clear jump can be observed in both the magnitude and the phase of the transfer functions where the short lead is in. As shown in this measured transfer functions, the measurement approach can monitor this jump variation within 1 cm length.

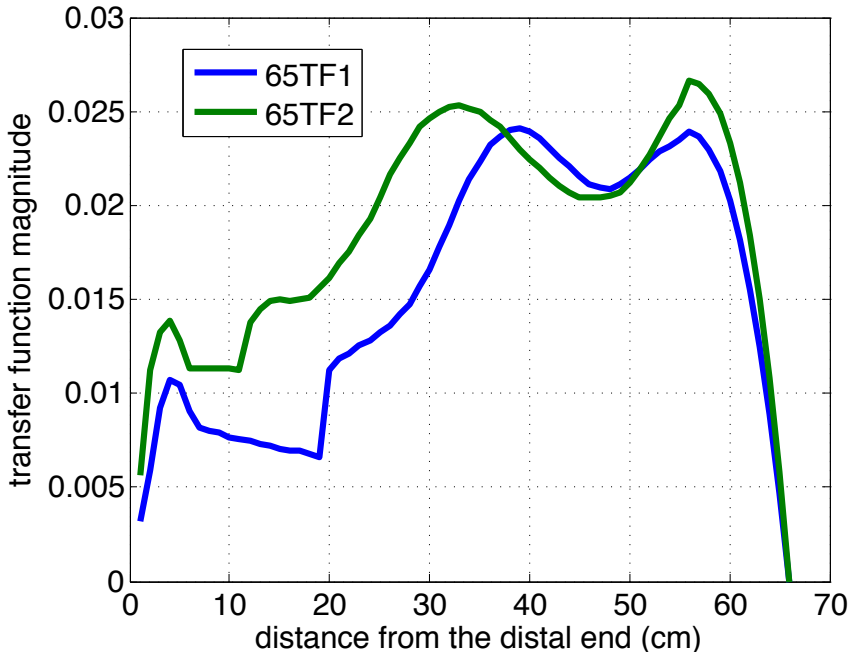

(a) Magnitude

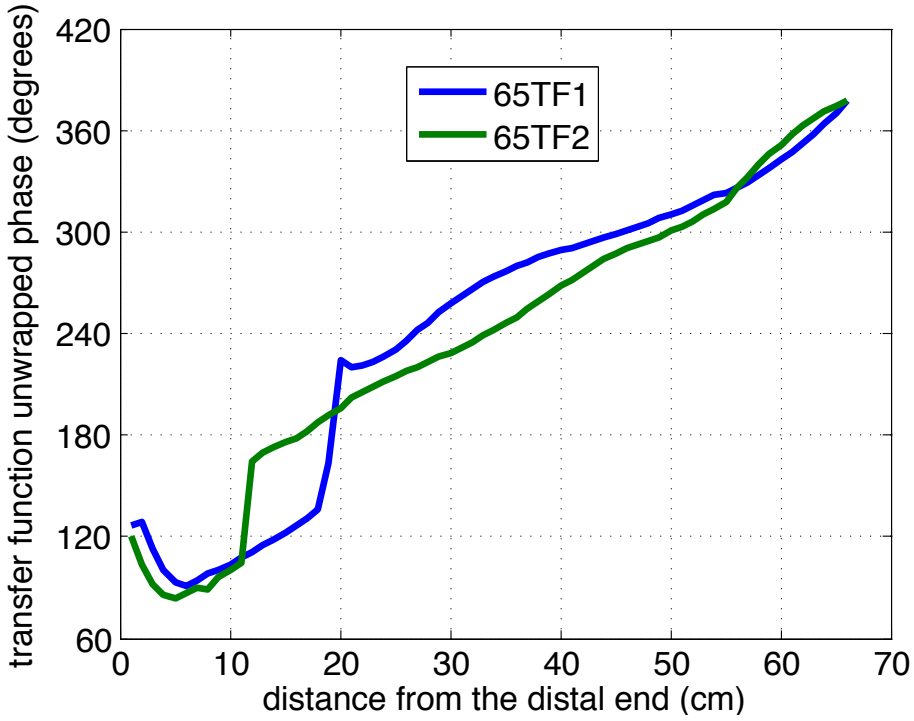

(b) Unwrapped phase

Fig. 3–17 Two dual leads 65 cm transfer functions with different short lead length.

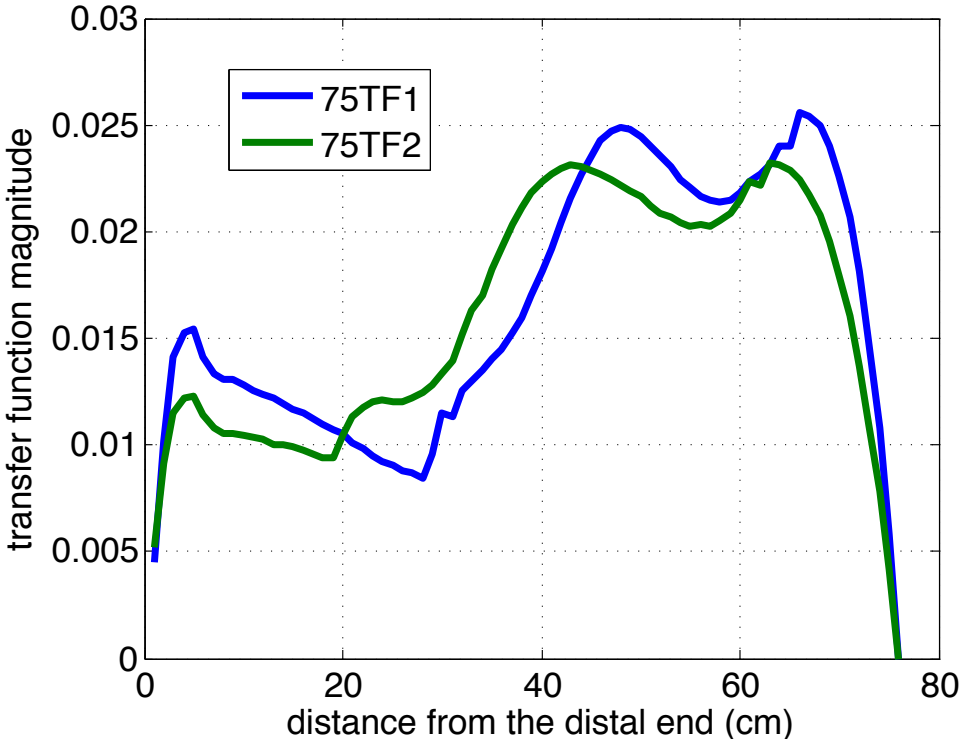

(a) Magnitude

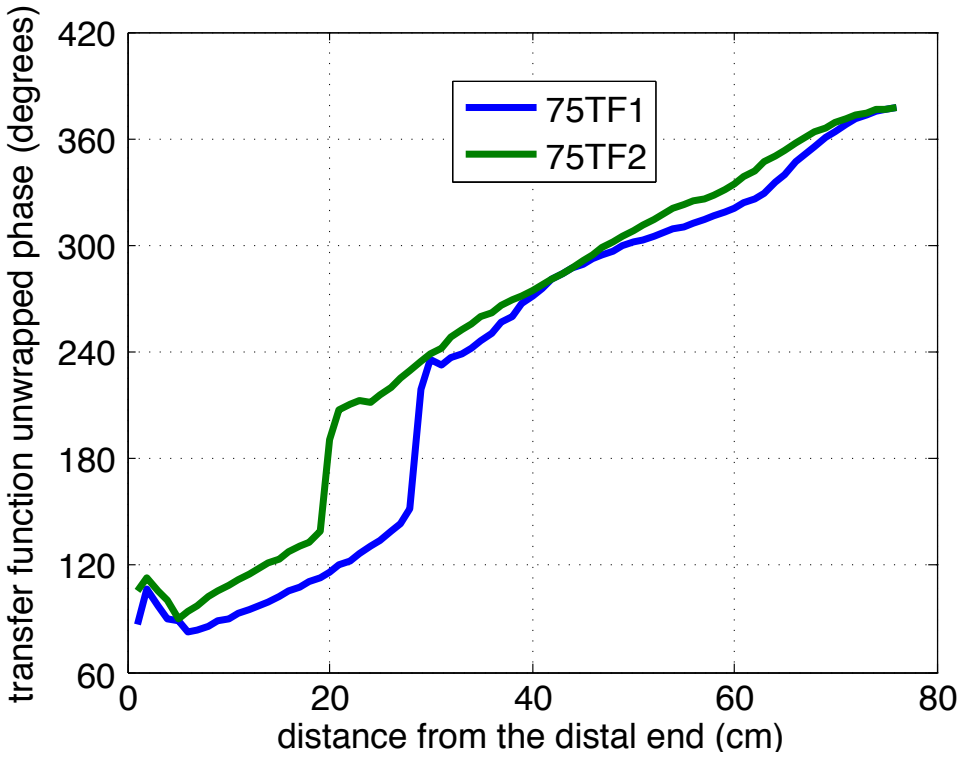

(b) Unwrapped phase

Fig. 3–18 Two dual leads 65 cm transfer functions with different short lead length.

3.4 Validation Results of Practical Leads Transfer Functions

Several different types of validation tests are performed to validate the measured practical lead transfer functions. First, the induced voltage for these leads laid in different trajectories is directly measured in the rectangular phantom. Considering the lead path and shape implanted in the patient's body as shown in Fig. 3–19, the validation test is also performed in these trajectories as shown in **Fig. 3–6**. These paths are one set of straight paths, one set of L-shape paths and one set of U-shape paths. Each set contains three paths at different distances from the sidewall of the phantom. In fact, the electrical field in the patient's body is much more complex than the electrical field in the ASTM phantom, even if the chosen lead path is the same as it in the patient's body. The human

body is a very inhomogeneous environment, but the saline in the phantom is a homogeneous media. However, rather than use this direct measurement to predict the induced voltage in the human body, we use it to verify our transfer function. Therefore, the nine trajectories could be used as the validation configuration as long as the incident field is different along different trajectories. Some of the test results are shown in tables below. Notice the leads sets are not the same as the leads set shown in 3.3.

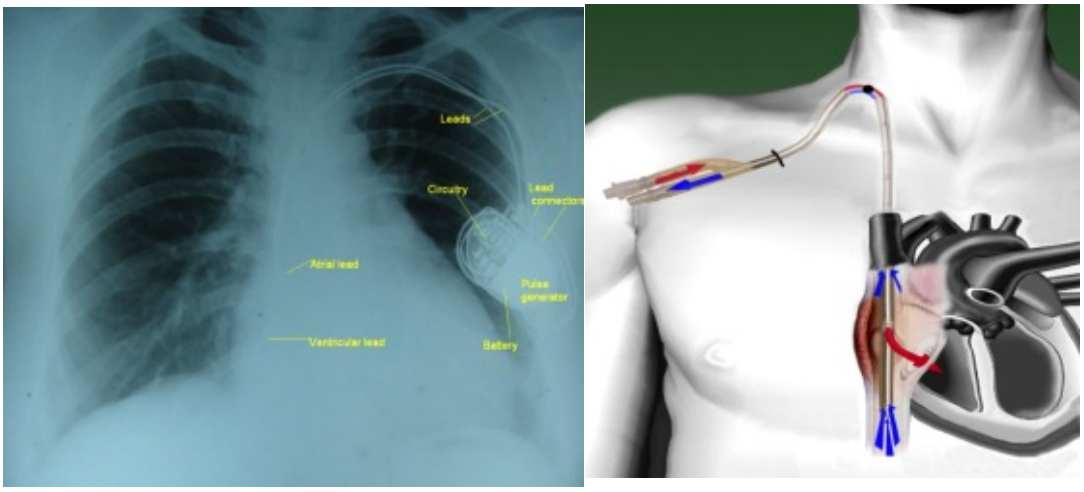

U-shaped path L shaped path

Fig. 3–19 Illustration of the U-shaped and L-shaped lead paths in the patient's body.

Table 3-3 Predicted induced voltage of leads set 1 in ASTM phantom.

Validation (modeling)	Induced voltage from modeling (V)									
Test condition	TF1	TF2	TF3	TF4	TF5	TF6	TF7	TF8	TV9	TF10
S1	1.13	0.63	1.08	0.65	1.26	0.62	1.2	0.61	1.22	0.62
S2	0.92	0.52	0.88	0.53	0.98	0.49	0.94	0.48	0.96	0.49
S3	0.66	0.37	0.63	0.38	0.67	0.33	0.64	0.33	0.65	0.33
L1	0.77	0.42	0.85	0.47	0.87	0.41	0.81	0.39	0.98	0.45
L2	0.64	0.35	0.73	0.41	0.69	0.33	0.65	0.31	0.81	0.38
L3	0.47	0.26	0.56	0.32	0.48	0.23	0.45	0.22	0.59	0.28
U1	0.53	0.38	0.6	0.44	0.55	0.41	0.56	0.38	0.76	0.43
U2	0.36	0.27	0.41	0.31	0.36	0.28	0.36	0.27	0.49	0.29
U3	0.24	0.18	0.27	0.21	0.24	0.18	0.24	0.17	0.31	0.19

Table 3-4 Measured induced voltage of leads set 1 in ASTM phantom.

Validation (measurement)	Induced voltage from measurement (V)									
Test condition	TF1	TF2	TF3	TF4	TF5	TF6	TF7	TF8	TV9	TF10
S1	1.01	0.61	1.05	0.61	1.18	0.57	1.16	0.56	1.11	0.57
S2	0.83	0.53	0.87	0.49	0.86	0.43	0.85	0.44	0.81	0.45
S3	0.65	0.36	0.63	0.38	0.6	0.29	0.57	0.3	0.6	0.33
L1	0.76	0.47	0.84	0.49	0.85	0.38	0.85	0.39	0.85	0.45
L2	0.58	0.35	0.71	0.37	0.63	0.29	0.66	0.3	0.67	0.37
L3	0.47	0.24	0.56	0.33	0.44	0.22	0.44	0.22	0.5	0.28
U1	0.52	0.4	0.64	0.41	0.61	0.41	0.59	0.31	0.67	0.37
U2	0.39	0.26	0.47	0.29	0.39	0.24	0.44	0.24	0.59	0.26
U3	0.24	0.18	0.29	0.2	0.28	0.18	0.3	0.17	0.32	0.19

Table 3-5 Percentage error between measurement and modeling of leads set 1.

Validation (error %)	Percentage error between measurement and modeling									
Test condition	TF1	TF2	TF3	TF4	TF5	TF6	TF7	TF8	TV9	TF10
S1	11.87	2.94	3.46	5.67	6.93	8.64	3.54	9.64	10.2	9.4
S2	11.4	-2.45	0.94	8.67	14.36	13.64	10.28	8.45	18.75	9.48
S3	2.28	5.36	0.82	0.85	11.08	15.79	12.35	10.75	8	1.91
L1	1.24	-10.84	2.09	-2.99	3.19	5.77	-4.61	-1.46	15.18	-0.35
L2	8.96	1.43	3.3	9.96	9.99	13.57	-2.3	5.86	20.01	1.93
L3	-0.39	9.61	-0.42	-3.05	7.47	4.46	1.05	-0.72	17.93	1.28
U1	1.46	-5.17	-5.92	7.79	-8.46	-0.58	-6.17	21.29	12.58	16
U2	-9.22	3.67	-14.32	6.58	-7.57	18.4	-17.34	12.79	-17.12	14.38
U3	2.94	1.2	-5.48	4.29	-12.87	-0.54	-19.52	0.16	-5.13	-3.22

Table 3-6 Measured and predicted induced voltage of a complex defibrillator lead 1.

Configuration	Voltage Type	Measured Voltage [V]	Modeling Voltage [V]	Error (%)
S1	T-R	0.30	0.34	-12
S2	T-R	0.25	0.29	-14
S3	T-R	0.20	0.23	-13
L1	T-R	0.31	0.31	0
L2	T-R	0.27	0.27	3
L3	T-R	0.22	0.22	1
U1	T-R	0.30	0.30	-1
U2	T-R	0.25	0.24	3
U3	T-R	0.23	0.19	16
S1	T-C	0.84	0.83	2
S2	T-C	0.74	0.71	5
S3	T-C	0.59	0.56	5
L1	T-C	0.74	0.69	8
L2	T-C	0.68	0.61	11
L3	T-C	0.58	0.52	11
U1	T-C	1.25	1.24	1
U2	T-C	0.92	0.98	-6
U3	T-C	0.63	0.70	-9
S1	RVC-C	0.21	0.22	-4
S2	RVC-C	0.19	0.18	3
S3	RVC-C	0.17	0.15	15
L1	RVC-C	0.19	0.19	0
L2	RVC-C	0.19	0.17	9
L3	RVC-C	0.17	0.15	18
U1	RVC-C	0.42	0.42	0
U2	RVC-C	0.34	0.33	4
U3	RVC-C	0.25	0.23	10
S1	PR-C	1.74	1.75	-1
S2	PR-C	1.49	1.50	-1
S3	PR-C	1.12	1.20	-6
L1	PR-C	1.32	1.40	-6
L2	PR-C	1.27	1.23	4
L3	PR-C	1.09	1.03	6
U1	PR-C	1.49	1.64	-9

Table 3-6 Measured and predicted induced voltage of a complex defibrillator lead 1 (continued).

U2	PR-C	1.25	1.33	-6
U3	PR-C	0.98	0.96	3
S1	DR-C	0.97	0.96	1
S2	DR-C	0.80	0.82	-3
S3	DR-C	0.56	0.65	-15
L1	DR-C	0.80	0.76	5
L2	DR-C	0.65	0.67	-2
L3	DR-C	0.51	0.56	-10
U1	DR-C	0.84	0.89	-6
U2	DR-C	0.66	0.72	-8
U3	DR-C	0.48	0.52	-8

Table 3-7 Measured and predicted induced voltage of a complex defibrillator lead 2.

Configuration	Voltage Type	Measured Voltage [V]	Modeling Voltage [V]	Error (%)
S1	T-R	0.36	0.36	0.00
S2	T-R	0.32	0.31	0.02
S3	T-R	0.25	0.25	0.01
L1	T-R	0.32	0.33	-0.04
L2	T-R	0.27	0.29	-0.07
L3	T-R	0.22	0.23	-0.06
U1	T-R	0.31	0.33	-0.05
U2	T-R	0.26	0.26	-0.02
U3	T-R	0.21	0.21	0.01
S1	T-C	0.82	0.77	0.06
S2	T-C	0.75	0.66	0.12
S3	T-C	0.61	0.53	0.16
L1	T-C	0.78	0.67	0.16
L2	T-C	0.69	0.59	0.16
L3	T-C	0.58	0.51	0.15
U1	T-C	1.30	1.31	-0.01
U2	T-C	1.02	1.03	-0.02
U3	T-C	0.73	0.74	-0.01
S1	RVC-C	0.25	0.21	0.19
S2	RVC-C	0.20	0.18	0.12
S3	RVC-C	0.16	0.14	0.12

Table 3-7 Measured and predicted induced voltage of a complex defibrillator lead 2 (continued).

L1	RVC-C	0.16	0.19	-0.13
L2	RVC-C	0.14	0.17	-0.17
L3	RVC-C	0.12	0.14	-0.16
U1	RVC-C	0.41	0.41	0.00
U2	RVC-C	0.29	0.32	-0.07
U3	RVC-C	0.20	0.22	-0.11
S1	PR-C	1.80	1.79	0.01
S2	PR-C	1.60	1.53	0.05
S3	PR-C	1.18	1.22	-0.04
L1	PR-C	1.49	1.42	0.05
L2	PR-C	1.33	1.25	0.06
L3	PR-C	1.08	1.05	0.03
U1	PR-C	1.50	1.67	-0.10
U2	PR-C	1.34	1.36	-0.01
U3	PR-C	1.09	0.97	0.12
S1	DR-C	0.83	0.82	0.01
S2	DR-C	0.72	0.70	0.02
S3	DR-C	0.54	0.56	-0.04
L1	DR-C	0.74	0.65	0.14
L2	DR-C	0.66	0.57	0.16
L3	DR-C	0.52	0.48	0.09
U1	DR-C	0.76	0.76	0.00
U2	DR-C	0.64	0.62	0.04
U3	DR-C	0.50	0.44	0.12

In addition to the trajectories in the rectangular phantom, we also validate some set of leads in the circular phantom. The lead trajectories chosen in the circular phantom are called fold-back lead paths as shown in Fig. 3–20. The electrical field in the circular phantom, as discussed in 2.4, is ideally a constant along a circumference. Thus, the fold-back test configuration produces an incident electrical field with a constant magnitude and a 180 degrees phase difference between the forward segment and the folded-back

segment. A set of leads is placed into both the ASTM phantom and the circular phantom. **Table 3-8** shows the predicted induced voltage, **Table 3-9** shows the directly measured induced voltage, and **Table 3-10** shows the error between them.

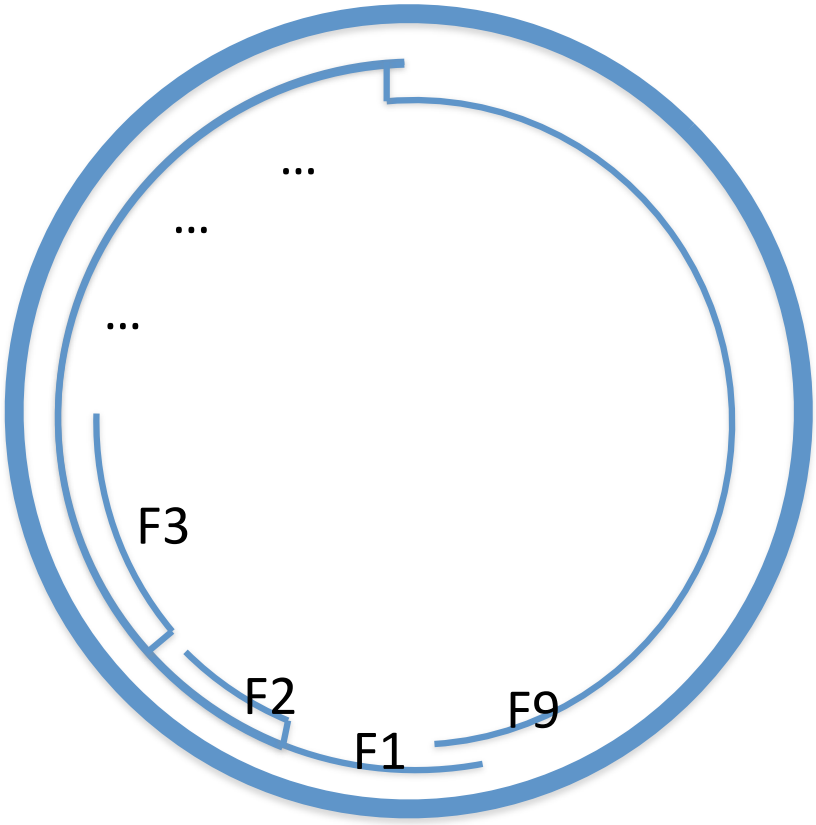

Fig. 3–20 Illustration of the fold-back path configurations in circular phantom for validation.

Table 3-8 Predicted induced voltage of leads set 2 in both ASTM phantom and circular phantom.

Validation (modeling)	Induced voltage from measurement (V)					
Test condition	Lead1 R-C	Lead1 T-C	Lead2 R-C	Lead2 T-C	Lead3 R-C	Lead 3 T-C
S1	0.73	0.33	0.28	0.85	0.41	0.61
S2	0.63	0.19	0.25	0.73	0.34	0.52
S3	0.50	0.04	0.20	0.58	0.27	0.42
L1	0.68	0.12	0.38	0.72	0.41	0.55
L2	0.61	0.28	0.32	0.63	0.34	0.48

Table 3-8 Predicted induced voltage of leads set 2 in both ASTM phantom and circular phantom (continue).

L3	0.50	0.27	0.25	0.52	0.27	0.39
U1	0.43	0.20	0.67	0.39	0.18	0.29
U2	0.40	0.13	0.55	0.32	0.15	0.25
U3	0.36	0.24	0.40	0.27	0.12	0.21
F1	0.76	0.31	0.14	0.83	0.43	0.56
F2	0.62	0.27	0.24	0.72	0.49	0.54
F3	0.40	0.24	0.54	0.55	0.60	0.48
F4	0.31	0.22	0.76	0.38	0.57	0.36
F5	0.35	0.19	0.78	0.28	0.32	0.21
F6	0.42	0.18	0.77	0.27	0.14	0.11
F7	0.52	0.21	0.72	0.40	0.28	0.16
F8	0.60	0.26	0.52	0.60	0.41	0.32
F9	0.68	0.31	0.19	0.77	0.38	0.49

Table 3-9 Measured induced voltage of leads set 2 in both ASTM phantom and circular phantom.

Validation (measurement)	Induced voltage from measurement (V)					
Test condition	Lead1 R-C	Lead1 T-C	Lead2 R-C	Lead2 T-C	Lead3 R-C	Lead3 T-C
S1	0.73	0.33	0.24	0.85	0.41	0.61
S2	0.57	0.21	0.19	0.71	0.34	0.47
S3	0.42	0.03	0.16	0.50	0.24	0.37
L1	0.68	0.10	0.37	0.73	0.44	0.57
L2	0.56	0.24	0.32	0.61	0.35	0.44
L3	0.47	0.24	0.24	0.45	0.23	0.34
U1	0.43	0.19	0.67	0.47	0.18	0.32
U2	0.37	0.14	0.58	0.34	0.13	0.24
U3	0.31	0.27	0.39	0.26	0.10	0.21
F1	0.74	0.30	0.14	0.85	0.44	0.51
F2	0.60	0.27	0.34	0.63	0.51	0.49
F3	0.49	0.23	0.66	0.46	0.60	0.43
F4	0.31	0.20	0.68	0.38	0.54	0.32
F5	0.34	0.17	0.83	0.22	0.34	0.21
F6	0.45	0.16	0.79	0.24	0.18	0.06
F7	0.59	0.20	0.68	0.46	0.35	0.13
F8	0.63	0.26	0.51	0.68	0.39	0.36
F9	0.68	0.29	0.28	0.90	0.40	0.53

Table 3-10 Percentage error between measurement and modeling of leads set 2.

Validation (error %)	Induced voltage from measurement (V)					
Test condition	Lead1 R-C	Lead1 T-C	Lead2 R-C	Lead2 T-C	Lead3 R-C	Lead3 T-C
S1	-0.14	0.30	18.10	-0.12	0.25	-0.16
S2	9.60	-8.42	28.78	2.73	0.89	11.19
S3	19.76	16.47	23.44	16.13	13.02	13.02
L1	-0.48	14.99	1.90	-1.68	-7.08	-3.50
L2	8.57	15.79	0.63	3.97	-3.50	7.33
L3	7.55	9.40	6.83	15.19	13.77	14.53
U1	0.62	4.61	0.00	-17.74	0.32	-7.33
U2	9.30	-7.74	-4.30	-3.41	12.09	2.15
U3	15.05	-11.58	2.50	4.83	23.54	-1.81
F1	2.01	1.66	2.63	-3.38	-0.72	9.94
F2	2.73	1.10	-27.87	15.10	-3.67	10.42
F3	-18.12	5.67	-18.24	19.86	-0.54	12.30
F4	-1.67	8.73	11.30	0.00	6.11	11.91
F5	2.73	15.68	-5.37	26.47	-7.93	-2.95
F6	-8.16	17.78	-2.60	10.18	-23.87	87.33
F7	-12.81	5.62	6.25	-13.49	-19.31	17.93
F8	-5.11	-2.21	0.92	-12.94	4.11	-12.66
F9	0.06	8.87	-33.62	-14.15	-3.28	-6.96

The correlation between the measured induced voltage and induced voltage predicted by transfer function is shown in Fig. 3–21. As the figure indicates, all the points from measurement and modeling approximate the ideal line on which modeling values are equal to measured values. The correlation coefficient between them is 0.9836, which shows strong agreement between each other. The histogram of the relative error is shown in Fig. 3–22. The relative error is defined as

$$Err = \frac{V_{predicted} - V_{measured}}{V_{measured}}, \tag{26}$$

where $V_{predicted}$ is the predicted induced voltage from the measured transfer function and the simulated incident electrical field. $V_{measured}$ is the directly measured induced voltage on the pacemaker located in the Phantom loaded in the MRI RF coil. The mean value of

the relative error is 0.010 which is very close to zero. The variance of the fitted normal distribution is 0.109. The maximum relative error is 0.369, which is relative high percentage error. However, this error occurs when the measured induced voltage is 0.28, which is a relatively small value among measured induced voltage, which can reach 1.8 V at some trajectories. The relative error is also plotted with the magnitude of the induced voltage in Fig. 3–23. The relative error is inversely related to the induced voltage because the signal noise ratio is worse at a small voltage than it at a large one. Therefore, the relative error could be mainly related to a direct measurement error rather than a transfer function measurement error. Overall, the predicted induced voltage closely matches the measured induced voltage for all tested lead trajectories.

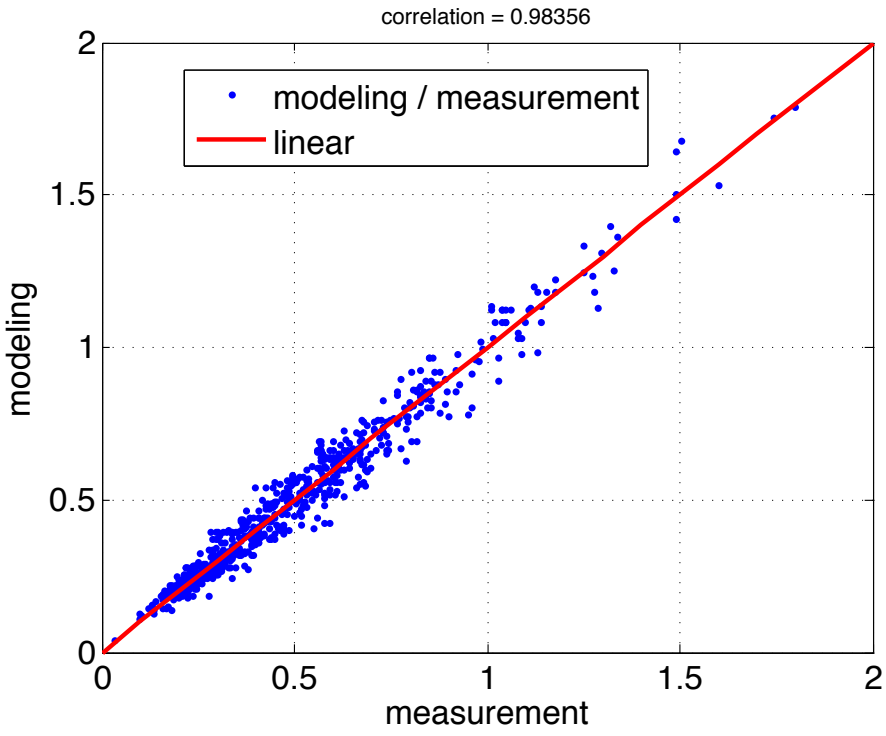

Fig. 3–21 Illustration of correlation between predicted (modeling) induced voltage and measured induced voltage.

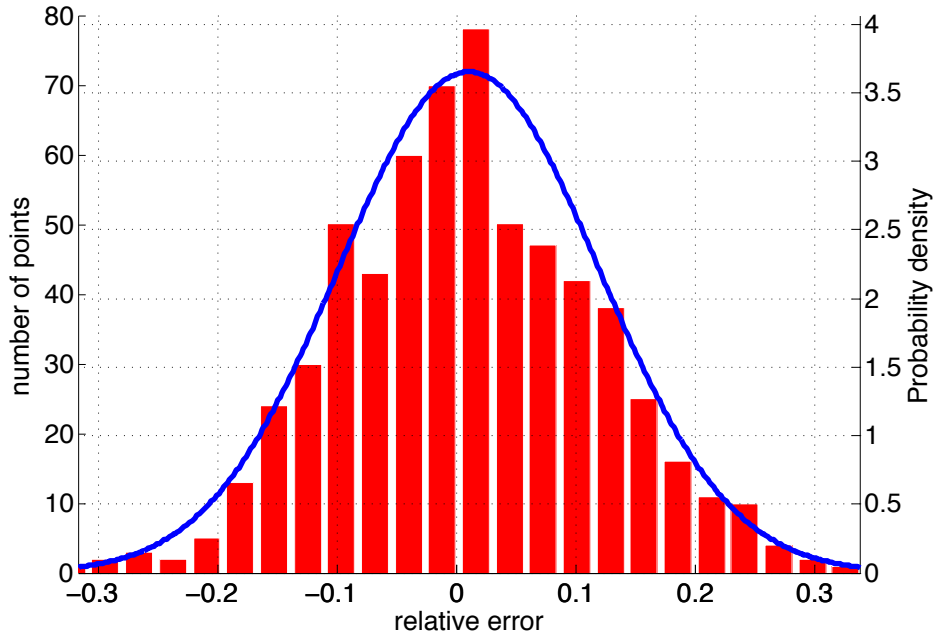

Fig. 3–22 Histogram plot of relative error between predicted voltage and measured voltage.

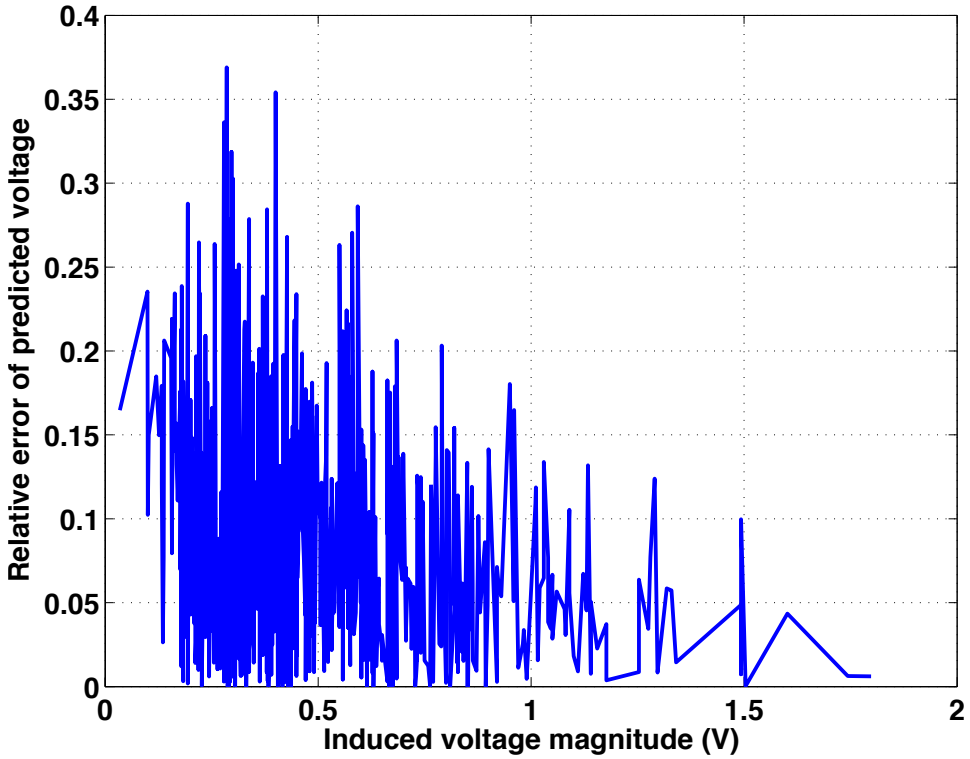

Fig. 3–23 The relative error of predicted induced voltage decreases as the magnitude of the induced voltage increases.

3.5 Fast Transfer Function Estimation Result

In addition to the using the reciprocity theorem to estimate the transfer function, a fast method is also proposed in 2.3.4. As discussed earlier, this fast method should work for a lead with a continuous structure. The set of 53 cm pacemaker leads, whose measured transfer functions are shown in Fig. 3–14, should belong in this category. The test features three steps. First, the induced voltage is calculated from the transfer function. The lead paths are the same as those chose in **Fig. 3–6**. Only six paths are needed to solve the problem. The calculated voltage is substituted into the equation

$$\sum_{n=1}^{6} C_n \int \underline{E}_{inc}^{m} \cdot B_n \underline{dl} = V_m \,, \tag{27}$$

where V_m is calculated from the transfer function, B_n is the bases shown in Fig. 2–7, $\underline{E}_{inc}^{m}$ is the incident field extracted from simulation, and C_n is the coefficients to be solved.

The transfer function is represented by

$$TF = \sum_{n=1}^{6} C_n B_n \quad . \tag{28}$$

The solved transfer functions are plotted with the measured transfer function in Fig. 3–24 and Fig. 3–25. They are closely aligned, which indicates that the chosen bases should contain all necessary information. To model the induced voltage measurement uncertainty, a random error is added to the calculated induced voltage. The estimated transfer functions solved from induced voltage with 1% random relative error are plotted with the measured transfer function in Fig. 3–26 and Fig. 3–27. There is a significant error between the solved and measured transfer functions, which indicates that the condition number of the coefficient matrix is bad and amplifies the small error on the induced voltage to a large error on the transfer function.

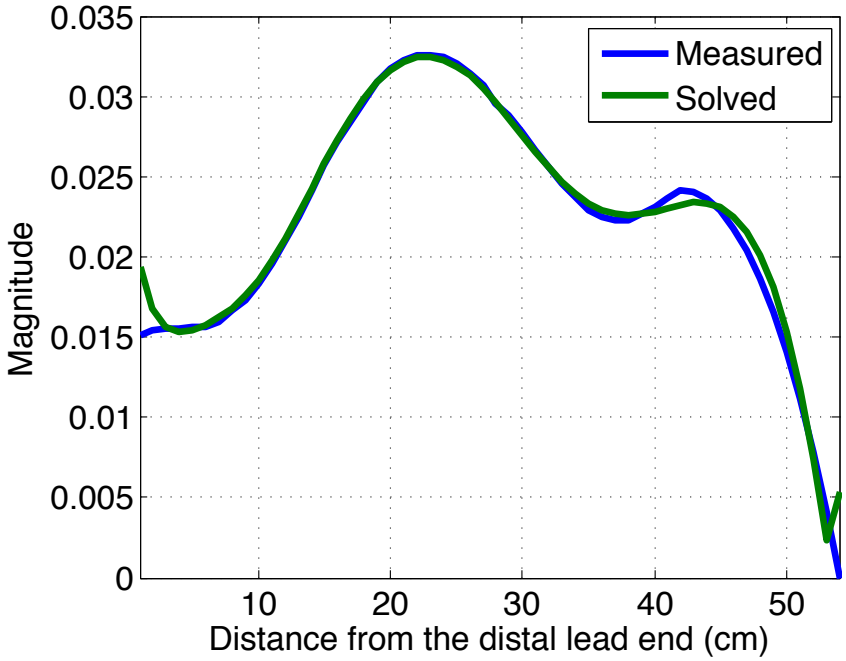

(a) Magnitude

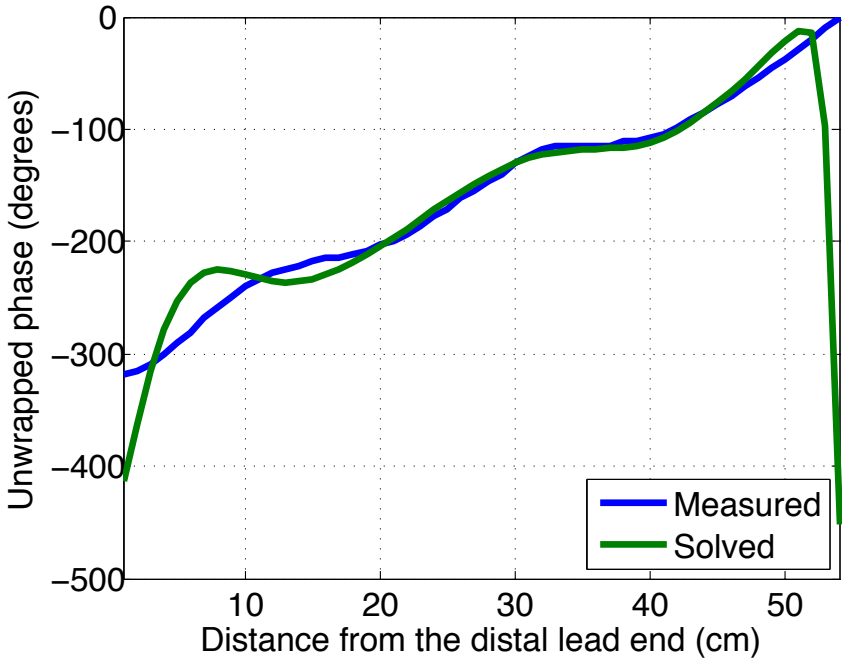

(b) Unwrapped phase

Fig. 3–24 Comparison of solved and measured transfer function 1 using exactly calculated induced voltage and S L U lead path.

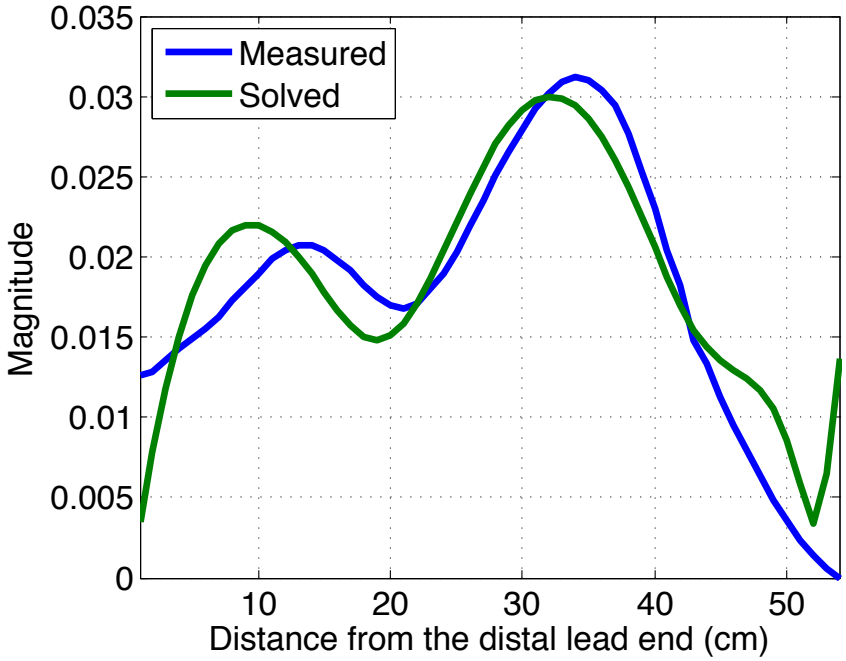

(a) Magnitude

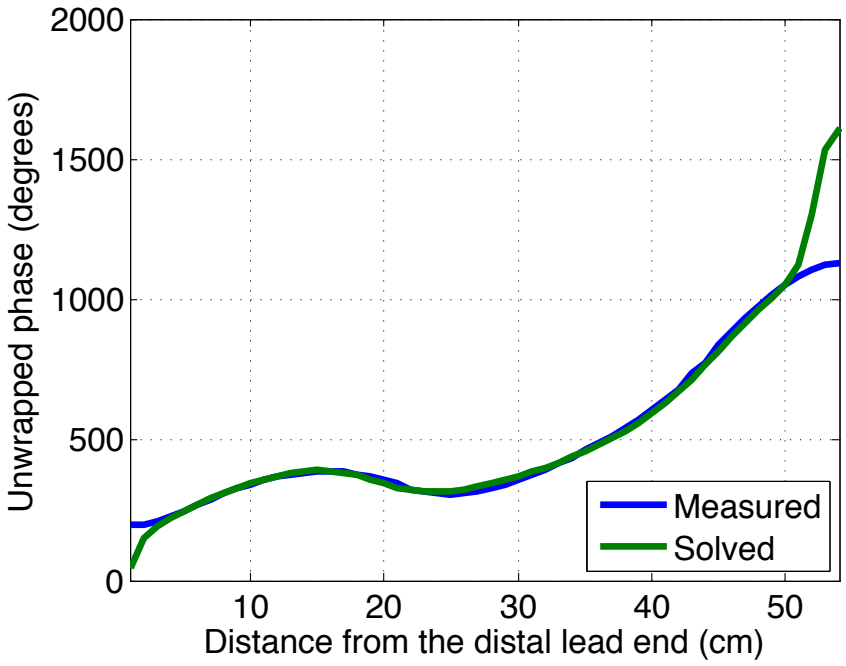

(b) Unwrapped phase

Fig. 3–25 Comparison of solved and measured transfer function 2 using exactly calculated induced voltage and S L U lead path.

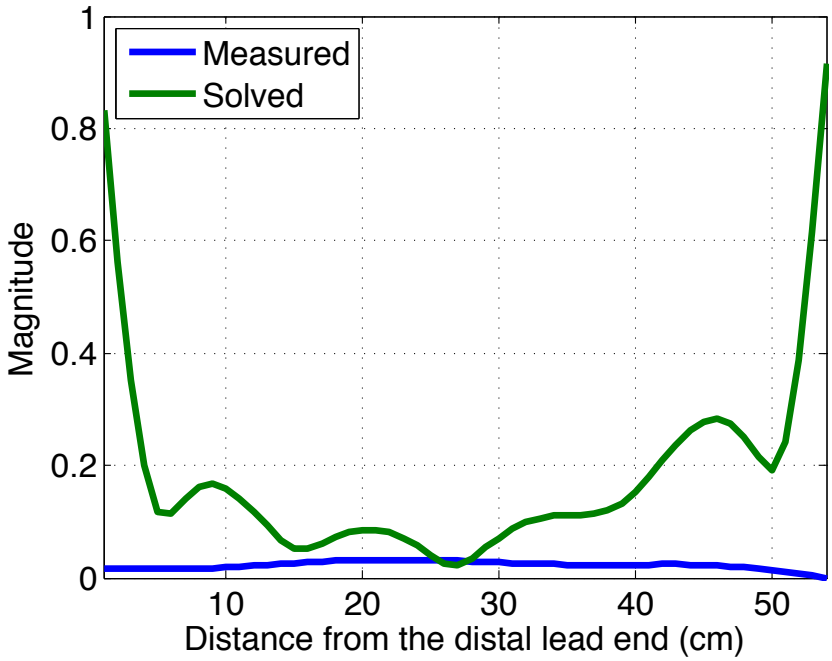

(a) Magnitude

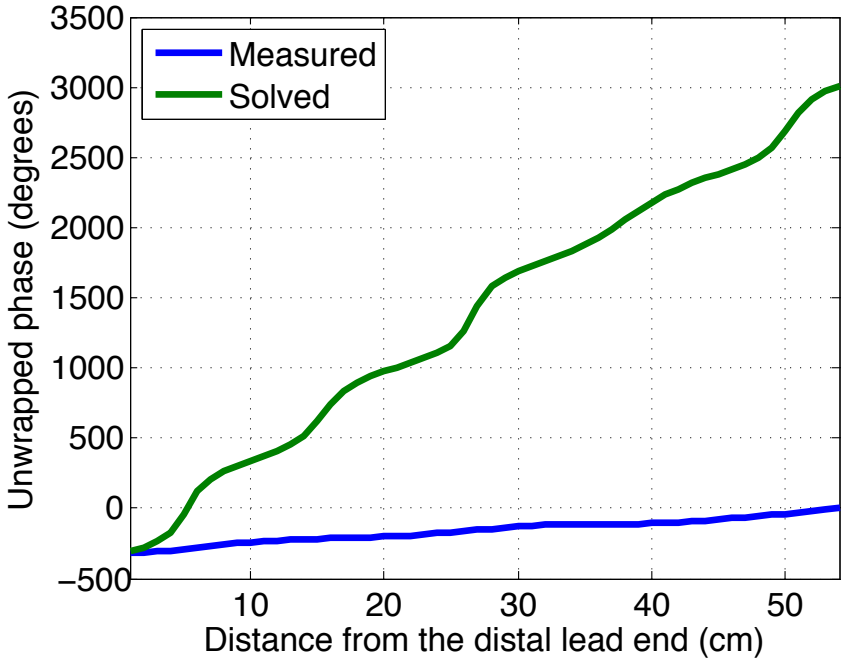

(b) Unwrapped phase

Fig. 3–26 Comparison of solved and measured transfer function 1 using calculated induced voltage with 1% random error.

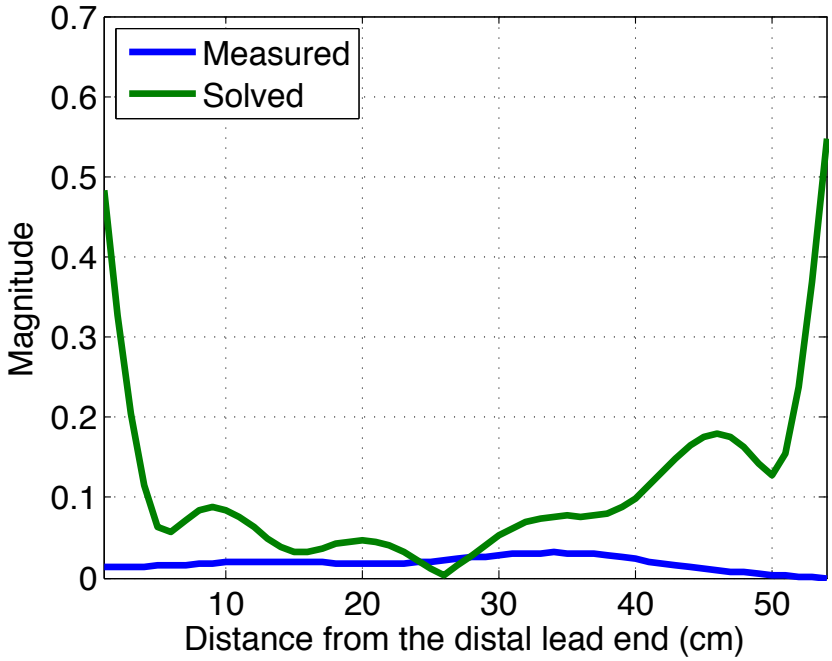

(a) Magnitude

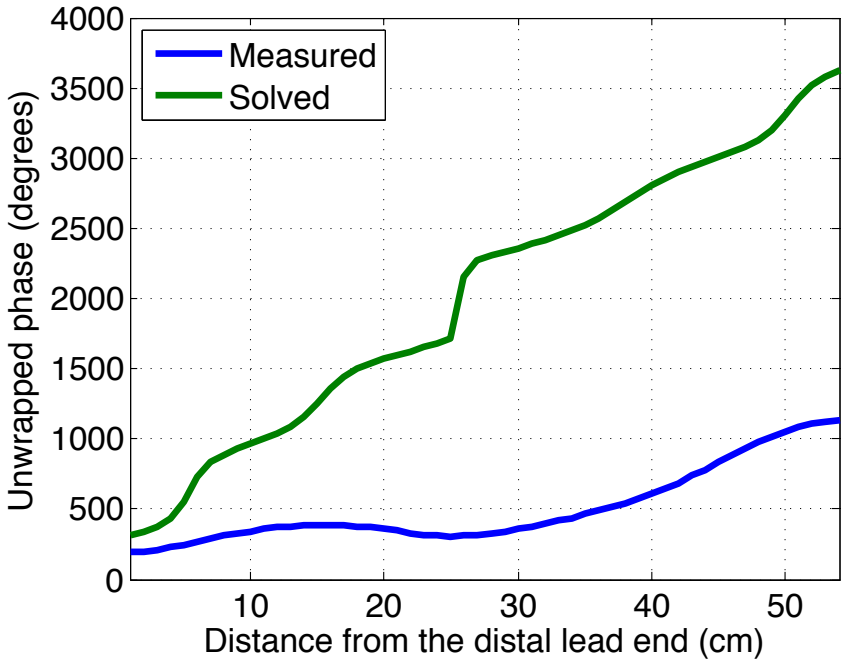

(b) Unwrapped phase

Fig. 3–27 Comparison of solved and measured transfer function 2 using calculated induced voltage with 1% random error.

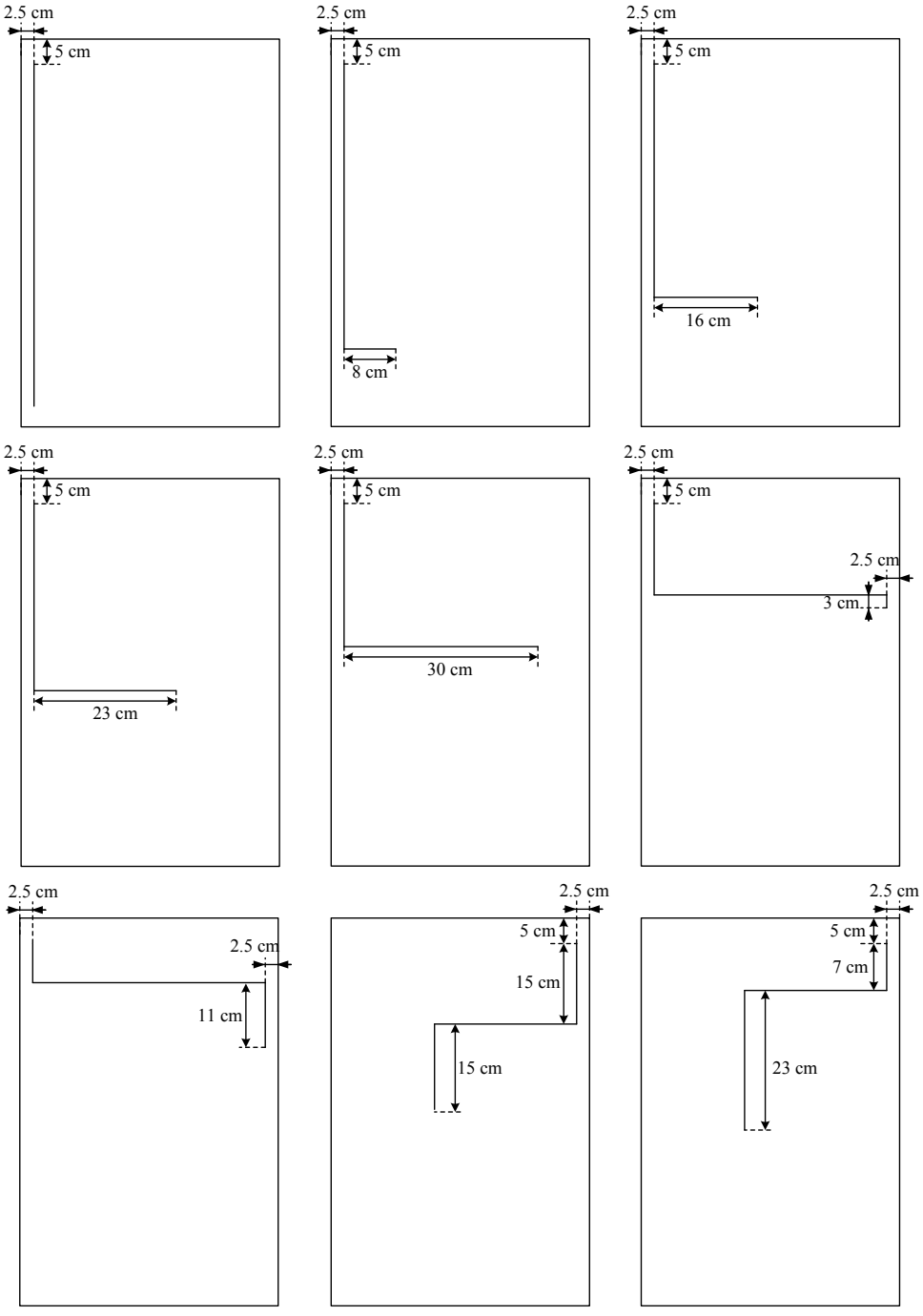

Fig. 3–28 Eight lead trajectories with low correlated incident fields are used to solve transfer function from inaccurate induced voltage.

Notice the bases are already orthogonalized, so the correlation of the coefficient matrix should come from the correlation of the incident field. In order to solve this problem, two improvements are made. On one hand, the test lead trajectories are modified as shown in Fig. 3–28 so that the correlation between different incident fields reduced dramatically. These paths may be not the best for practical measurement of induced voltage because of the measurement configuration difficulty. On the other hand, instead of just six induced voltages on different lead paths, nine induced voltages are considered, and the transfer function coefficient is solved from over determined linear equations by the least squares method.

Fig. 3–29 and Fig. 3–30 show comparison result between measured transfer function and the solved transfer function solved from 20% random error induced voltage, which is a reasonable value based on the validation result shown in 3.4.

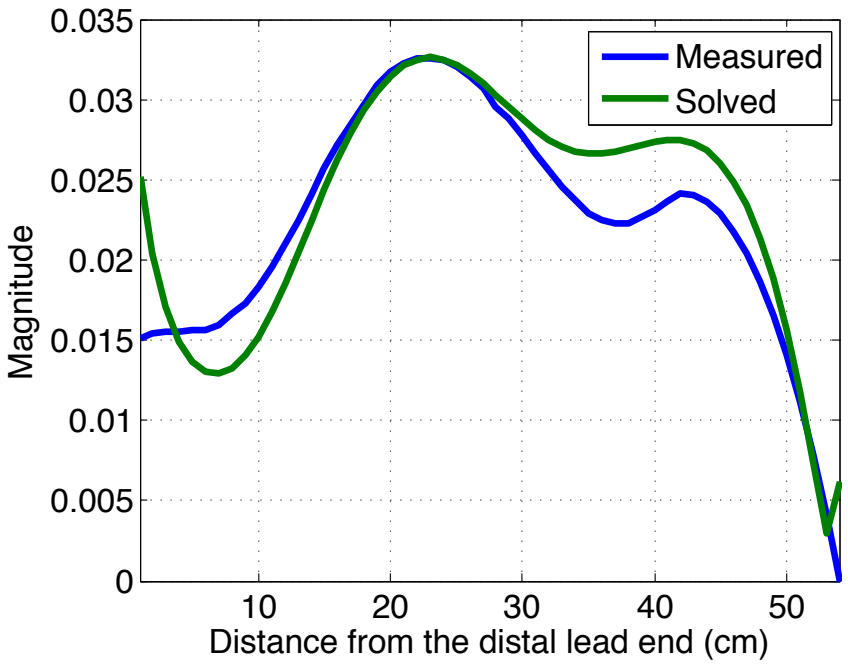

(a) Magnitude

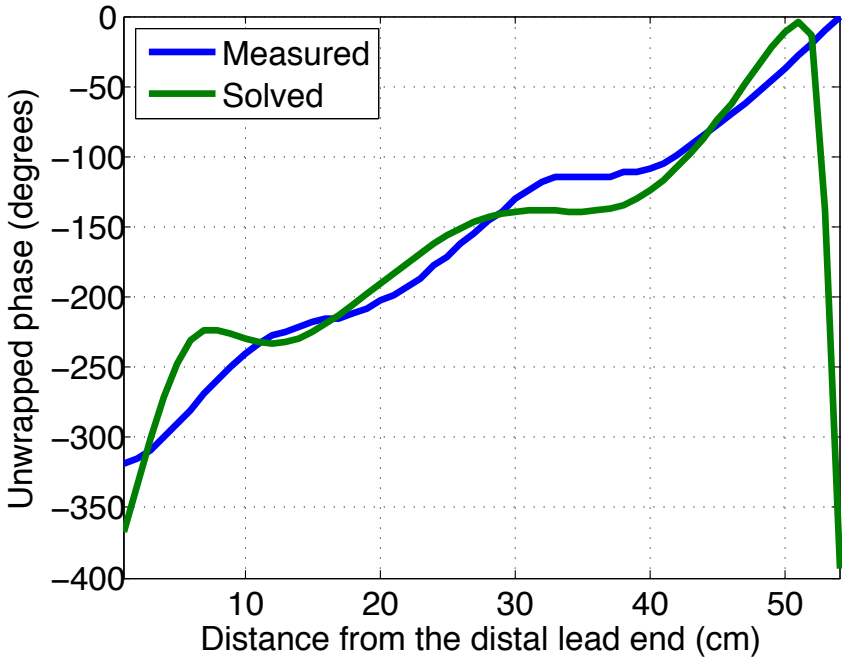

(b) Unwrapped Phase

Fig. 3–29 Comparison of solved and measured transfer function 1 using calculated induced voltage on optimized trajectories with 20% random error.

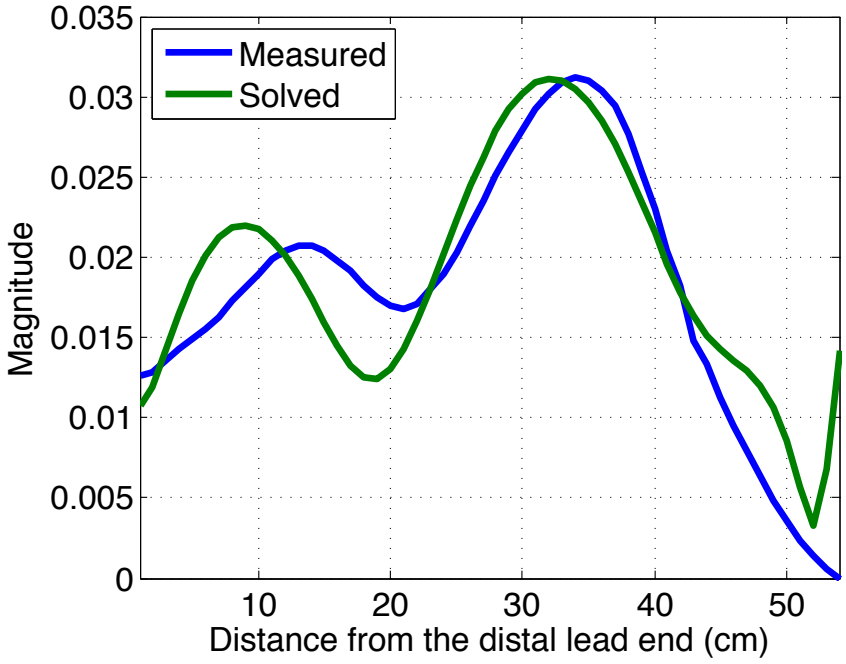

(a) Magnitude

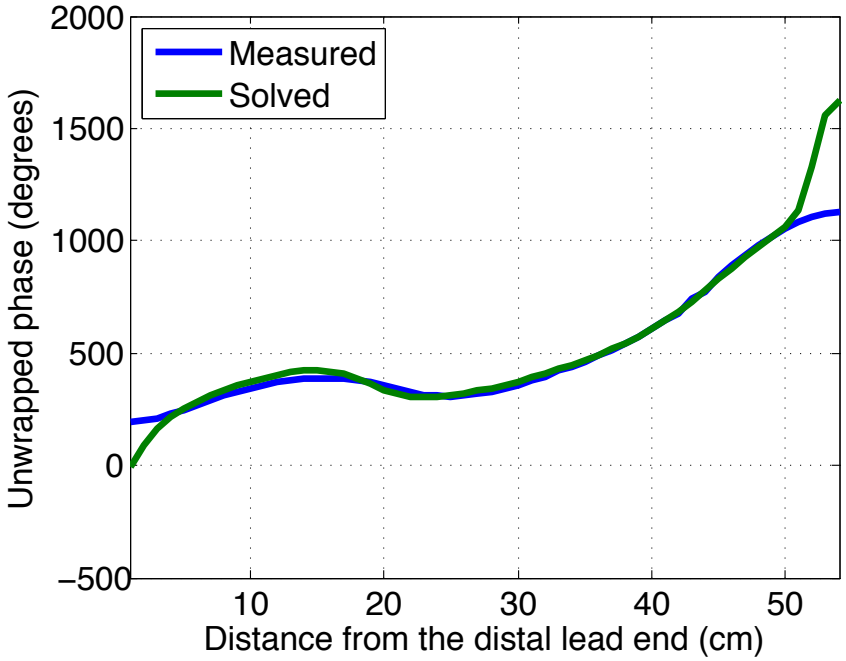

(b) Unwrapped phase

Fig. 3–30 Comparison of solved and measured transfer function 2 using calculated induced voltage on optimized trajectories with 20% random error.

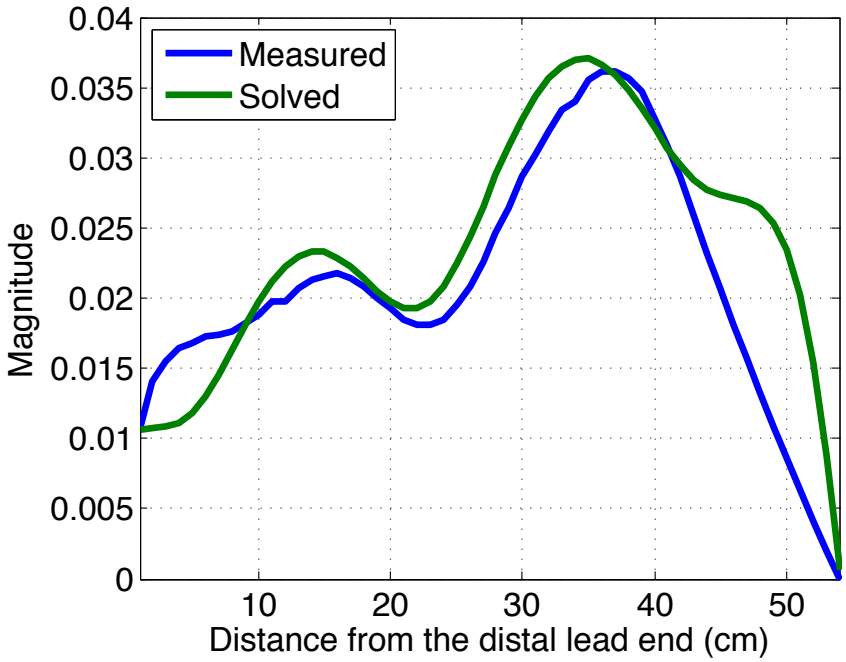

(a) Magnitude

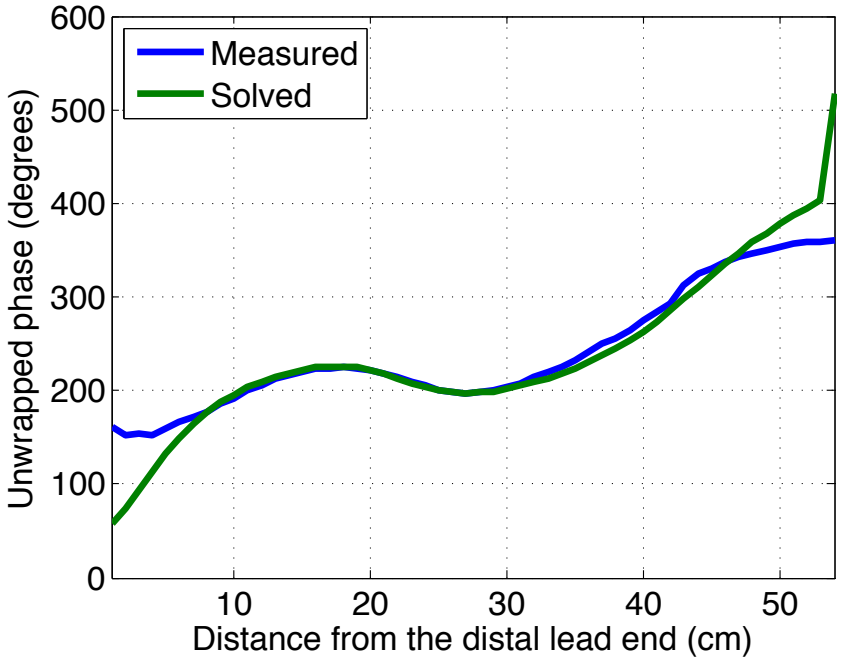

(b) Unwrapped phase

Fig. 3–31 Comparison of measured transfer function and solved transfer function from measured induced voltage.

After the improvement of the lead paths, the solved transfer function is still stable even if 20% error is introduced to the induced voltage. Fig. 3–31 shows the comparison result between the measured transfer function and the solved transfer function from measured induced voltage. Despite some obvious errors occurs on some segment, the solved transfer function displays behavior very similar to that of the measured transfer function.

Chapter 4 Human Body and Phantom Effect Study

The induced voltage on the device CAN or the transfer function and the incident electrical field determine the temperature rise of the tissue around the lead distal end together. The transfer function has been studied in previous chapters. The human body and the phantom mainly determine the incident field. In this chapter, we focus on the effects of the human body and the phantom.

4.1 Transfer Function Used in This Study

A temporary pacemaker lead with 40cm length is chosen and used during the surgery. Usually, a temporary pacemaker lead has three different penetration statuses: 1) all inside, 2) 20 cm in and 20 cm out, and 3) all out. The distal end of the all "out" lead is penetrated into the human body. Measured transfer functions of three statuses are shown in Fig. 4–1, Fig. 4–2 and Fig. 4–3.

As shown in the figure, the transfer functions of the same lead are totally different when the lead penetration status is different. When the lead is completely implanted into the human body, the transfer function magnitude is relatively small at the lead distal end, and the phase smoothly decreases from the distal end to the near end. Meanwhile, the magnitude is relatively large at the distal end when the lead is partially implanted. The phase still decreases from the distal end to the near end; however the phase is not monotone decreasing, and the variation range is much smaller than the transfer function of the completely implanted lead. When all but the last segment of the distal end of the

lead is in the air, the transfer function displays a constantly large magnitude with small phase variation.

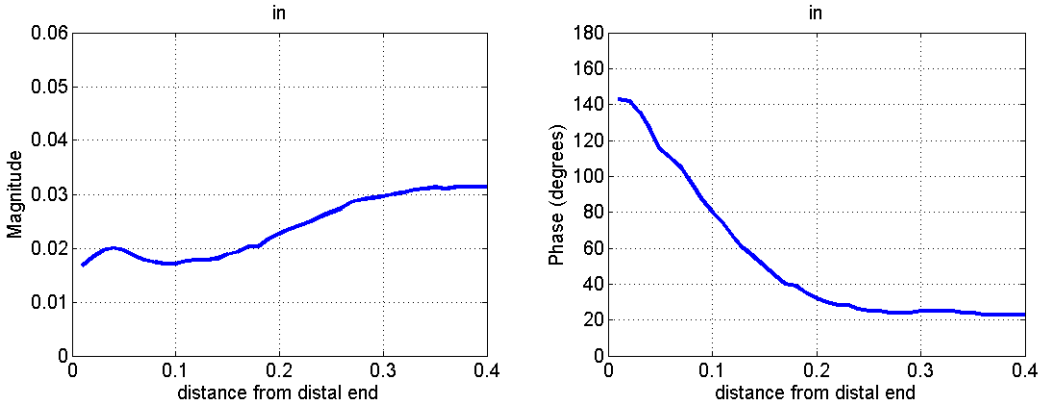

(a) (b)

Fig. 4–1 Transfer function (a) magnitude and (b) phase of the lead all in the saline.

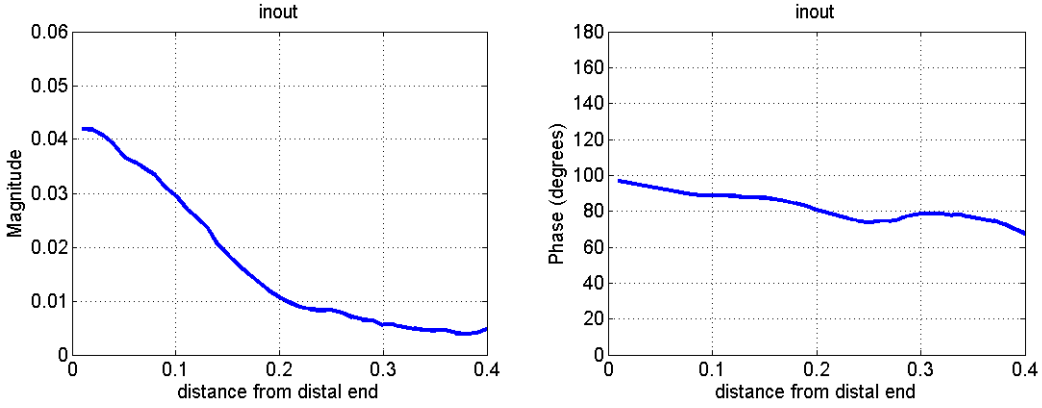

(a) (b)

Fig. 4–2 Transfer function (a) magnitude and (b) phase of the lead partial in and partial out of the saline.

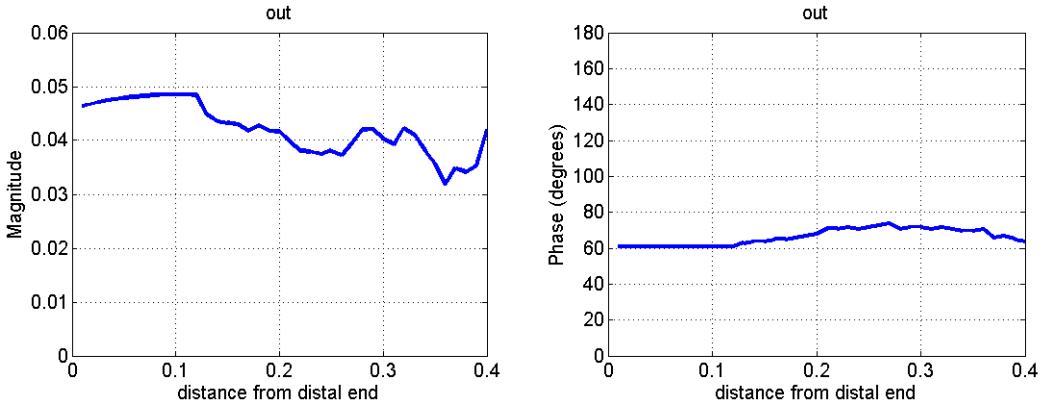

(a) (b)

Fig. 4–3 Transfer function (a) magnitude and (b) phase of the lead all out of the saline.

4.2 Incident Electrical Field Along Lead Paths of Three States

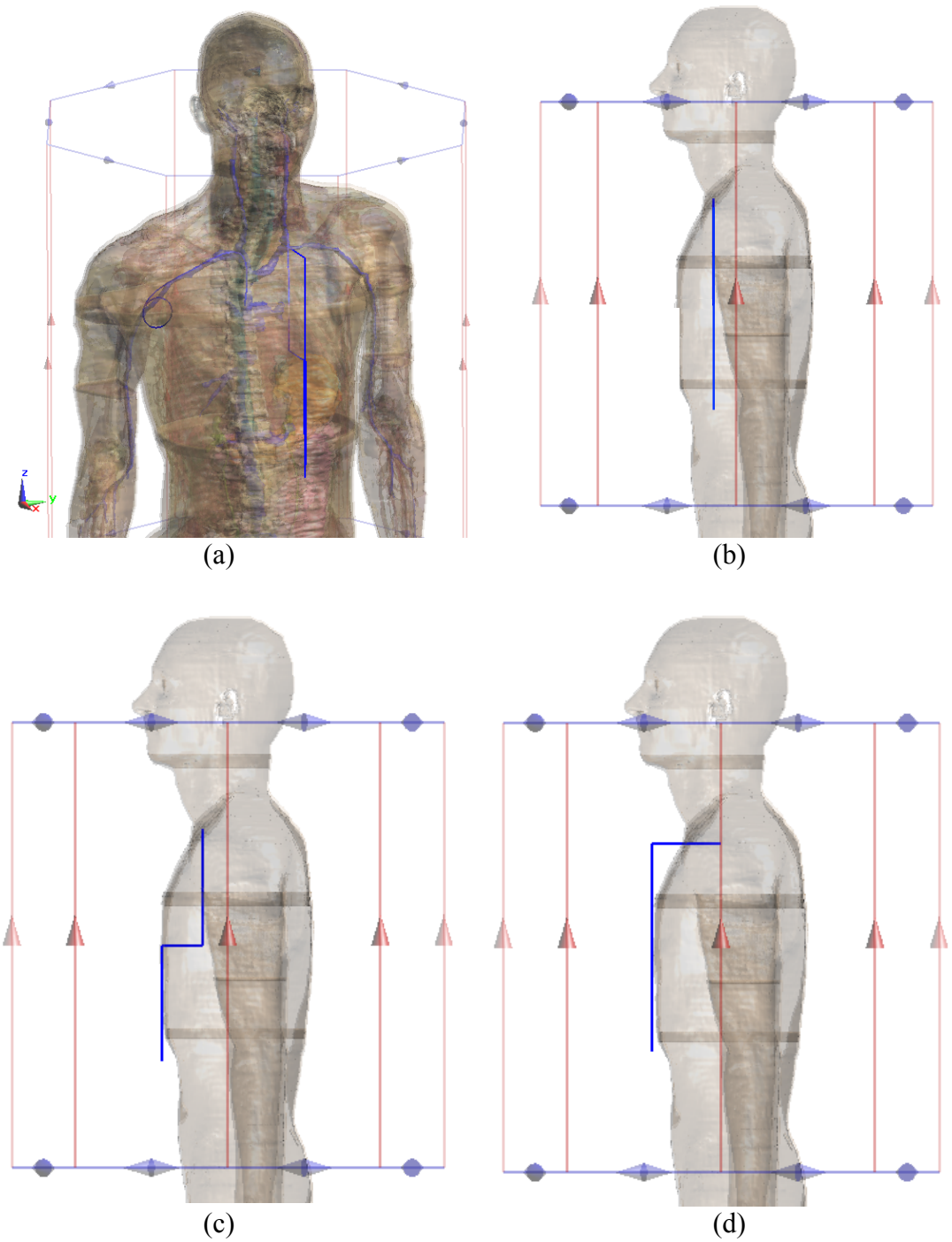

(a) (b)

(c) (d)

Fig. 4–4 Lead paths with adult male body model: (a) the over view; (b) all “in” lead path; (c) partially in, partially out lead path; (d) all “out” lead path.

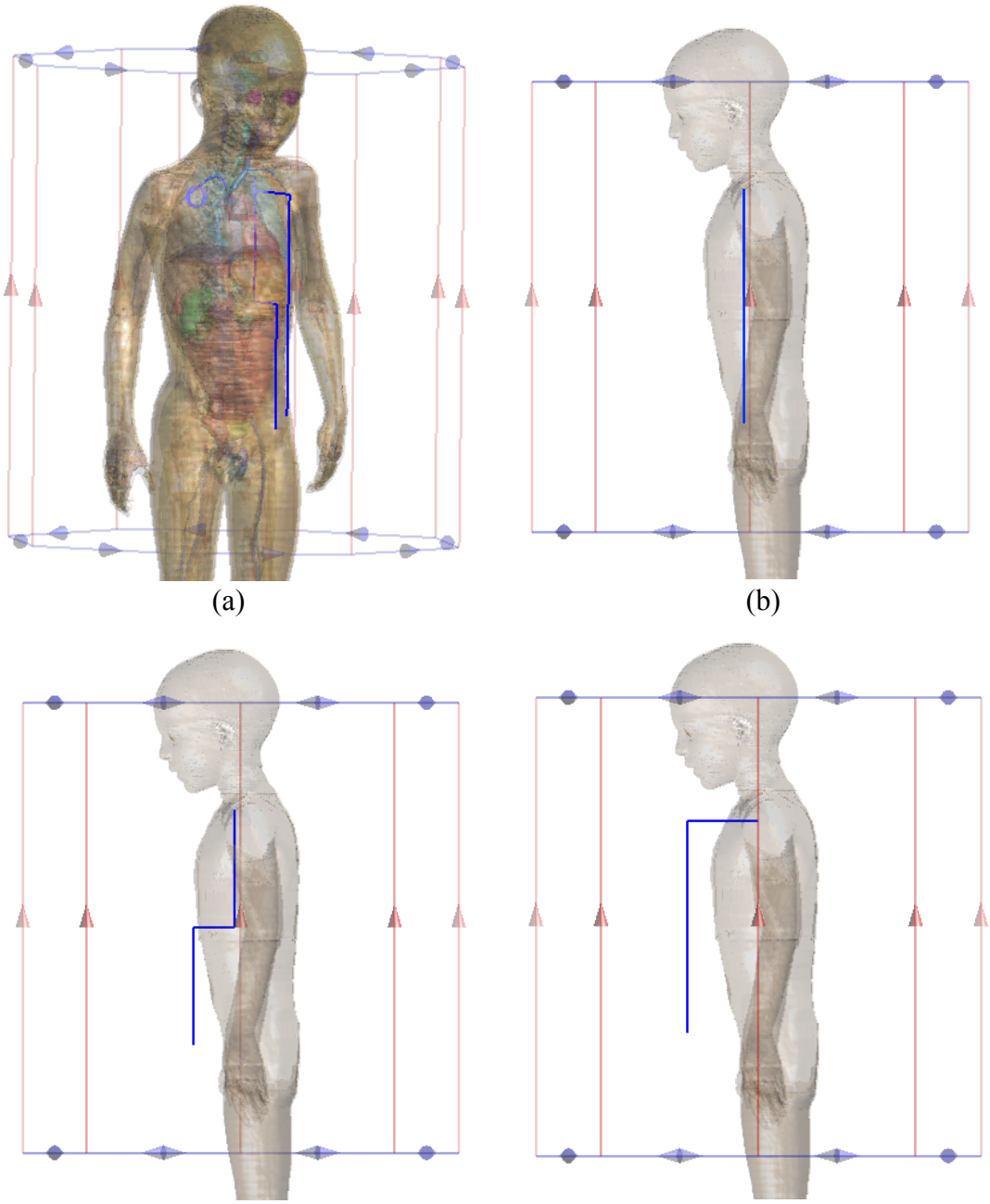

(a) (b)

(c) (d)

Fig. 4–5 Lead paths with boy body model: (a) the over view; (b) all “in” lead path; (c) partially in, partially out lead path; (d) all “out” lead path.

Three bodies/phantoms are studied in this section: an adult male model, a boy model, and an ASTM phantom with head. The lead path with the studied model is shown in Fig. 4–4, Fig. 4–5 and Fig. 4–6. For all three studied body/phantom models, the leads are located at the left chest. The incident field difference due to both the lead penetration

status and the body volume are considered. Although the boy model and adult model are generated independently, the boy model can be seen as a practical scaled version of the adult male. The ASTM phantom is scaled to 0.8 and 0.7 times of the original one geometrically.

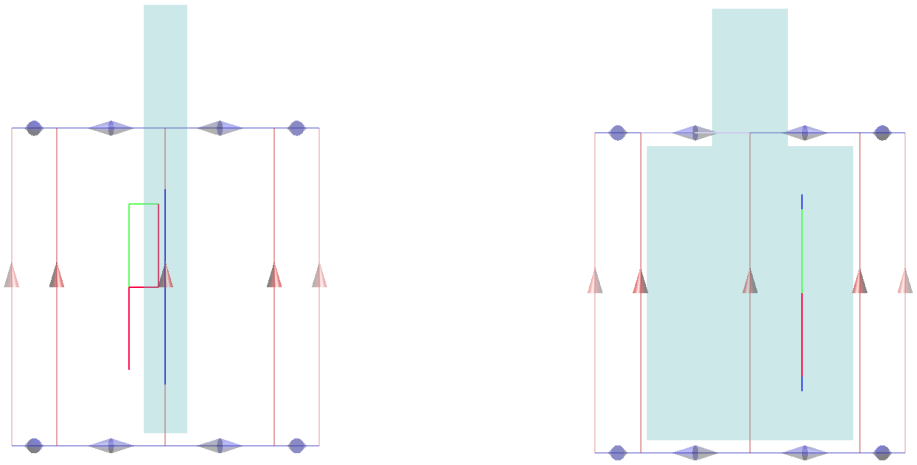

(a) (b)

Fig. 4–6 Lead paths with phantom model in (a) the side view and (b) the front view.

The tangential component of incident electrical fields along different lead trajectories in the human body model and phantom model are plotted in Fig. 4–7 to Fig. 4–15. The input power of all the simulation is normalized so that the one-gram average SAR is 2 W/Kg in the human body or phantom.

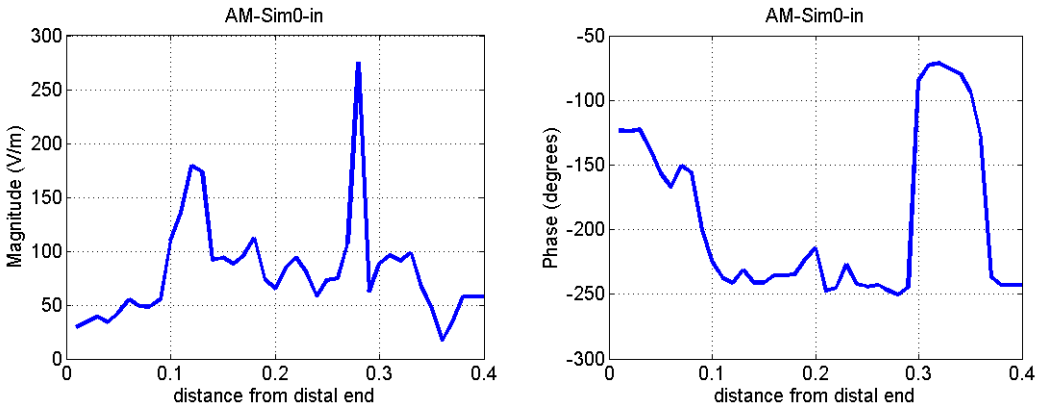

(a) (b)

Fig. 4–7 Tangential incident field (a) magnitude and (b) phase along the lead path all in the adult male left chest.

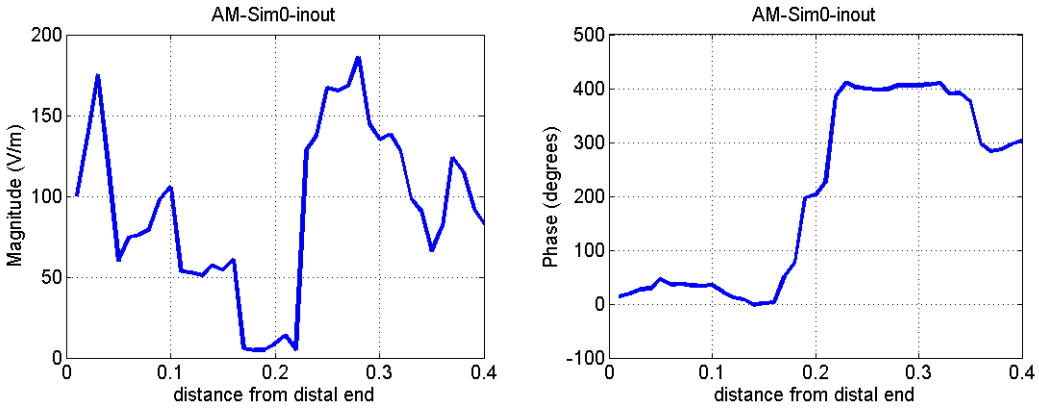

(a) (b)

Fig. 4–8 Tangential incident field (a) magnitude and (b) phase along the lead path partially in and partially out of the adult male left chest.

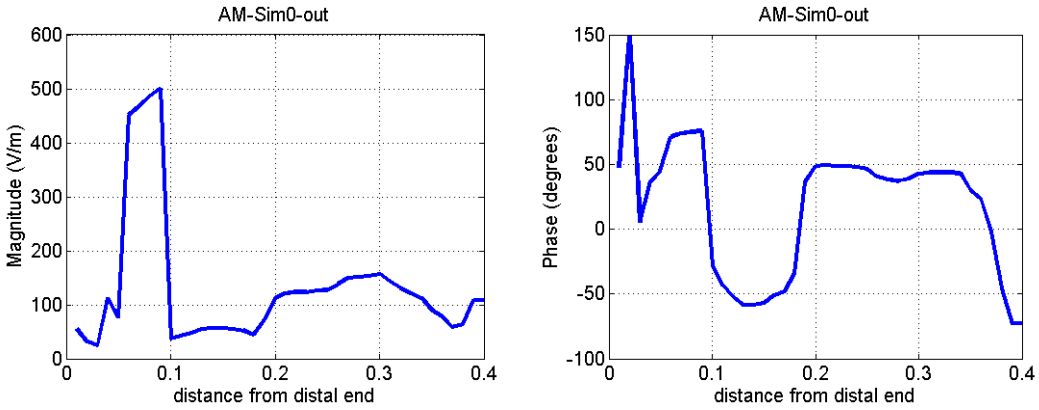

(a) (b)

Fig. 4–9 Tangential incident field (a) magnitude and (b) phase along the lead path all out of the adult male left chest.

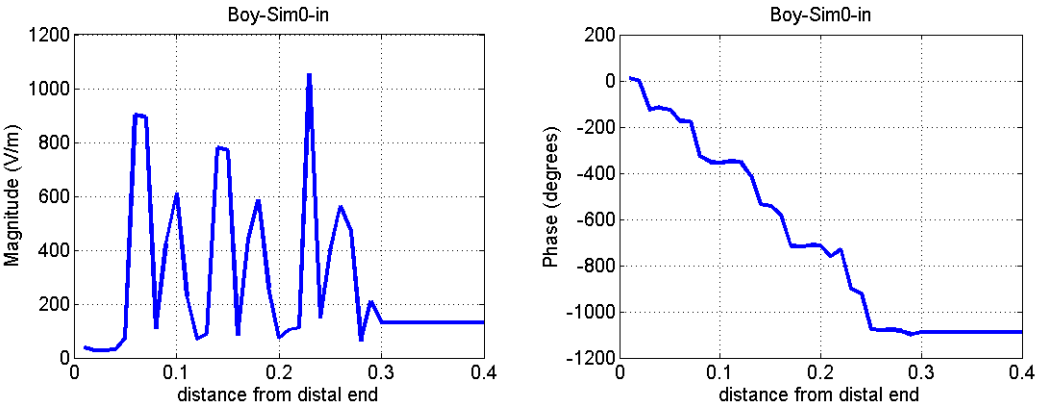

(a) (b)

Fig. 4–10 Tangential incident field (a) magnitude and (b) phase along the lead path all in the boy left chest.

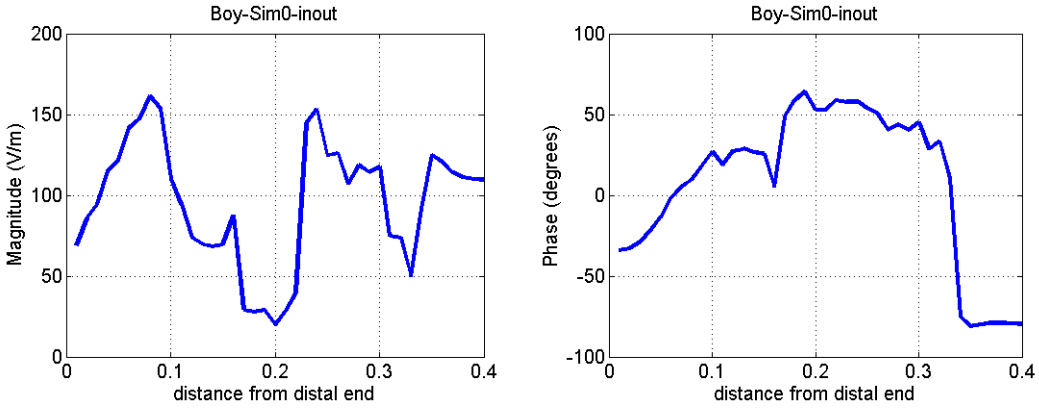

(a) (b)

Fig. 4–11 Tangential incident field (a) magnitude and (b) phase along the lead path partially in and partially out of the boy left chest.

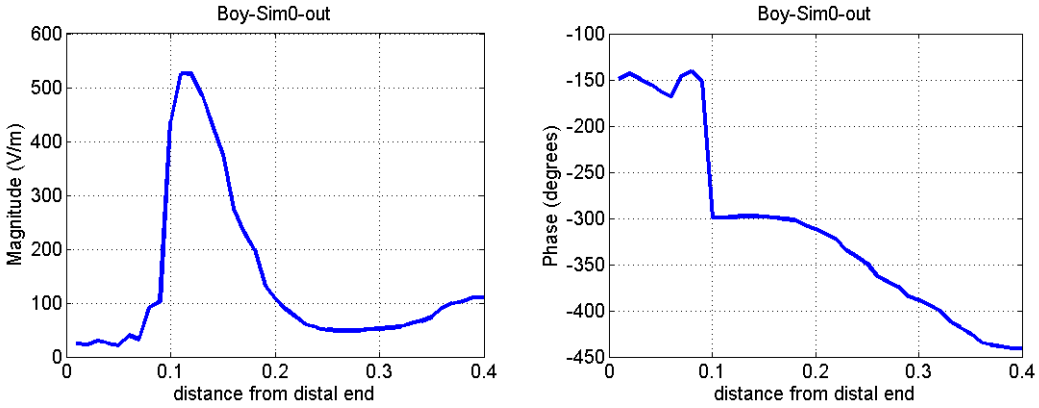

(a) (b)

Fig. 4–12 Tangential incident field (a) magnitude and (b) phase along the lead path all out of the boy left chest.

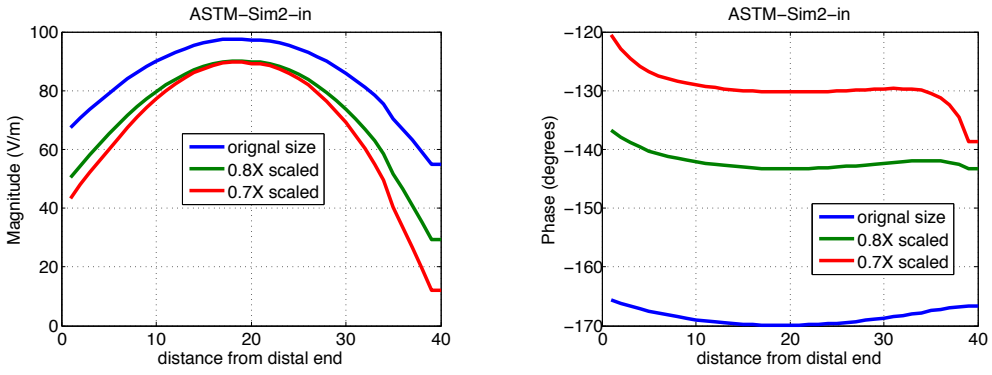

(a) (b)

Fig. 4–13 Tangential incident field (a) magnitude and (b) phase along the lead path all in the ASTM phantom with different sizes.

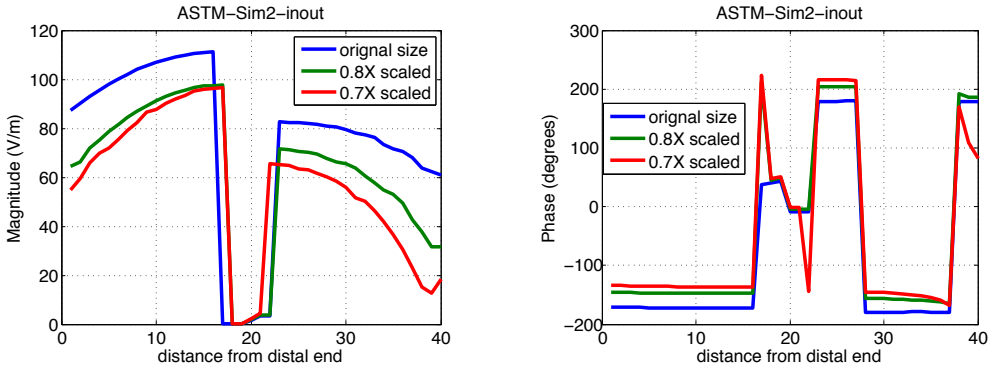

(a) (b)

Fig. 4–14 Tangential incident field (a) magnitude and (b) phase along the lead path partially in and partially out of the ASTM phantom with different sizes.

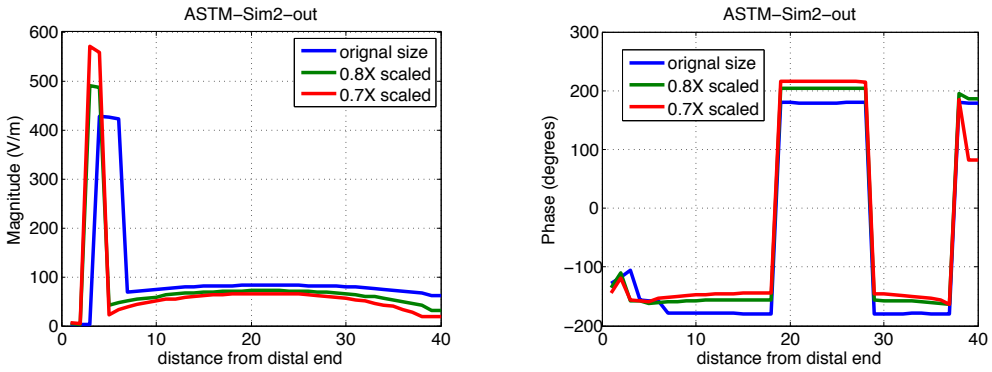

(a) (b)

Fig. 4–15 Tangential incident field (a) magnitude and (b) phase along the lead all out of the ASTM phantom with different sizes.

The tangential incident electrical field consistently displays complex variation with the human body model due to its inhomogeneity. Meanwhile, variation of the incident fields in the phantom model is much simpler. In the ASTM phantom, the smaller the volume of the phantom is, the weaker the incident field is. Because the total mass of the phantom decreases as the volume is scaled smaller, the total input power of the MRI RF coil is lower because the all the input power is normalized so that the one gram average SAR is 2W/Kg. However, in the human body, although the boy has a significantly lower total mass than the adult male, the incident field along the path here is much larger than it is in the adult male. This is due to the inhomogeneous tissue in the

human body. Apparently, the lead in the boy body passes through some tissue with very high permittivity.

4.3 Temperature Rise Results and Discussion

The temperature rise at the lead distal end is calculated using equation (11), and the results are shown in Table 4-1, Table 4-2 and Table 4-3.

Table 4-1 Temperature rise in adult male model.

Configuration	In	Partial in partial out	Out
Temperature rise (°C)	0.1116	0.3034	3.1905

Table 4-2 Temperature rise in boy model.

Configuration	In	Partial in partial out	Out
Temperature rise (°C)	0.6827	0.3435	2.3988

Table 4-3 Temperature rise in ASTM phantom model.

Configuration	In			Partial in partial out			Out		
Scaling factor	1	0.8	0.7	1	0.8	0.7	1	0.8	0.7
Temperature rise (°C)	0.4425	0.3128	0.2636	0.3289	0.2313	0.2023	2.7902	1.8701	1.5820

All the out lead paths always have the highest temperature rise due to a large transfer function value and the relative slowly variation of both the transfer function and the incident field. The boy has a higher temperature rise than the adult male on the "partially in partially out" path and the "in" path. However, the result reverses on the "out" path. For the ASTM phantom, temperature rise is always lower with smaller phantom volume for all three penetration-statuses.

This test along is not sufficient to determine a correlation between temperature rise and the body model. However, several conclusions can be drawn based on this test. First, the transfer function of the lead in the air usually varies slowly along the entire lead

due to the relatively long wavelength of the 64 MHz signal. Furthermore, the volume of the body/phantom model typically has a positive correlation with total incident field since the incident power is normalized to the 2 w/Kg. However the value of certain incident field is highly path dependent. Finally, the phase cancellation plays an important role in determining the final temperature rise.

Chapter 5 Conclusions and Future Work

5.1 Conclusions

As discussed in the introduction, it is computationally prohibitive to perform a complete lead, phantom/human subjects, and RF coil simulation all together even with state-of-the-art electromagnetic modeling tools. In this thesis, a novel approach decouples the simulation/measurement of the lead characteristics from the human/phantom simulation. In this procedure, the characteristic behaviors of the pacemaker leads are carefully examined using either simulation or measurement methods. Such information can be combined with conventional human/phantom simulation results to estimate induced electric field for various lead trajectories. This is a practical technology that allows device manufactures to accurately estimate the induced electrical field from the lead along any possible trajectory inside the human subject. This knowledge will lead to significant advancement in the MRI labeling area.

Several simple examples and many practical lead examples have been used to demonstrate the efficiency and accuracy of the proposed approach. All transfer functions were validated by directly measured/simulated induced voltage or induced electrical fields. The results indicate strong agreements between predicted results and measured/simulated results. The result of the human body model simulation shows that the characteristics of an implanted lead and the incident electric field generated by the RF coil have a significant impact on implanted lead heating or induced voltage between different lead electrodes.

Compared with other results and methods [9]-[28], by applying the reciprocity approach developed in this thesis, for the first time, people can achieve such highly accurate predicted results for practical clinical leads. This method is also efficient enough to generate a transfer function in a short time period. This is an economical approach because electrical probes generating localized field are not required, and because of the stability of the method and measurement setting other expensive mechanical machine are not necessary.

5.2 Future Work

The framework of transfer function measurement and use of the transfer function to predict the pacemaker/defibrillator-induced voltage/heating has been completed. However, three areas in this subject need further research.

First, the direct measurement of the induced voltage or heating could be better designed. On one hand, the lead trajectory is chosen in straight, L and U shapes similar to the path shape when implanted in the patient body. However, the incident field is totally different along those paths compared with the field on the same path inside the human body. Although these paths are sufficient for the transfer function validation, the direct measurement results cannot predict the true induced voltage when the device is implanted. Therefore, better lead trajectories should be defined. Along these lead trajectories, we can obtain either more similar incident fields as in the human body, or obtain the worst incident fields so that the induced voltage/heating can be seen as the upper bound of the possible value. On the other hand, the phase information of the direct measurement is not accurate enough. This information is needed for the fast transfer

function estimation. Also it can be treated as another quantity to validate the measured transfer function in addition to the magnitude.

Second, the uncertainty plays a very important role in determining the pass/fail criterion of the test. At present, we assume the uncertainty of the whole measurement is constituted by independent individual uncertainty of each step of the measurement. The total combined uncertainty is calculated from

$$U_c = \sqrt{\sum_{i=1}^{m} c_i^2 \cdot u_i^2} \,, \tag{29}$$

where U_c is the total uncertainty, c_i is the weight of each individual uncertainty and u_i is the individual uncertainty. There are two major problems with this estimation. 1) Many individual uncertainties of the measurement are not independent. 2) It is very difficult to extract the weight c_i of each individual uncertainty. In practical experiments, it is difficult to adjust only one component, while keeping everything else fixed. Due to these two problems, the combined uncertainty is over estimated and inaccurate. A more efficient approach and uncertainty model needs to be developed.

Finally, a series of lead design ideas could be proposed and tested based on the measured transfer function. Since the transfer function is equivalent to the total current distribution along the lead when an excitation is added on the concerned location, a special lead design to break the current distribution can possibly reduce the total energy coupled to the device lead and then reduce the induced voltage or heating effect. In addition, a carefully designed shield may also dramatically reduce the EMC problem of the lead.

References

[1] "2007 MRI benchmark report from IMV medical"[online]. Available: http://www.imvinfo.com/index.aspx?sec=mri&sub=dis&itemid=200023.

[2] J. R. Gimbel and E. Kanal, "Can patients with implanted pacemakers safely undergo magnetic resonance imaging?" *Journal of the American College of Cardiology*, vol. 43, no. 7, pp. 1325-1327, April 2004.

[3] J. R. Gimbel, "The safety of MRI scanning of pacemakers and ICDs: what are the critical elements of safe scanning? Ask me again at 10 000." *Europace*, vol. 12, no. 7, pp 915-917, July 2010.

[4] J. R. Gimbel, "The AHA Scientific statement of MRI in patients with devices: neat, but incomplete. Unwise and unsupported," *Pacing and Clinical Electrophysiology*, vol 31, no. 6, pp. 649-651, June 2008.

[5] J. R. Gimbel, S. M. Bailey, P. J. Tchou, P. M. Ruggieri, B. L. Wilkoff, "Strategies for the safe magnetic resonance imaging of pacemaker-dependent patients," *Pacing and Clinical Electrophysiology*, vol 28, no. 10, pp. 1041-1046, October 2005.

[6] W. Irnich, "Risks to pacemaker patients undergoing magnetic resonance imaging examinations." *Europace*, vol. 12, no. 7, pp. 918-920, July 2010.

[7] M. Fiek, T. Remp, C. Reithmann, and G. Steinbeck, "Complete loss of ICD programmability after magnetic resonance imaging," *Pacing Clin Electrophysiol*, vol. 27, no. 7, pp. 1002-1004, July 2004.

[8] T. Azuma, K. Sasaki, K. Kawabata, A. Osada, H. Itagaki, K. Komura, T. Takahashi, K. Ishida, Y. Satoh, and S. Umemura, "MRI-Compatible Ultrasonic Probe for Minimally Invasive Therapy," *IEEE Ultrasonics Symposium*, Munich, Germany, October 2002, vol. 2, pp.1465-1468.

[9] S. Pisa, G. Calcagnini, M. Cavagnaro, E. Piuzzi, E. Mattei, and P. Bernardi, "A study of the interaction between implanted pacemakers and the radio frequency field produced by magnetic resonance imaging apparatus," *IEEE Trans. Electromag. Compat*, vol. 50, no. 1, pp. 35-42, February 2008.

[10] S. Pisa, P. Bernardi, M. Cavagnaro, and E. Piuzzi, "Power absorption and temperature elevation produced by magnetic resonance apparatus in the thorax of patients with implanted pacemakers," *IEEE Trans. Electromag. Compat*, vol. 52, no. 1, pp. 32-40, February 2010.

[11] S. Feng, R. Qiang, W. Kainz, D. R. Jackson, and J. Chen, "Efficient Evaluation of MRI-Induced Electric Fields in the Vicinity of Implantable Lead," *Texas Symposium on Wireless and Microwave Circuits and Systems (WMCS)*, Waco, TX, USA, April 2013.

[12] A Roguin, M. M. Zviman, G. R. Meininger, E. R. Rodrigues, T. M. Dickfeld, D. A. Bluemke, A. Lardo, R. D. Berger, H. Calkins, and H. R. Halperin, "Modern pacemaker and implantable cardioverter/defibrillator systems can be magnetic resonance imaging safe: in vitro and in vivo assessment of safety and function at 1.5 T," *Circulation*, vol. 110, no. 5, pp. 475-482, August 2004.

[13] C.-K. Chou, J. A. McDougal, and K. W. Chan, "RF heating of implanted spinal fusion stimulator during magnetic resonance imaging," *IEEE Trans. on Biomedical Engineering,* vol. 44, no. 5, pp. 367-373, May 1997.

[14] E. Matttei, M. Triventi, G. Calcagnini, F. Censi, W. Kainz, G. Mendoza, H. I. Bassen, and P. Bartolini, "Complexity of MRI induced heating on metallic leads: Experimental measurements of 374 configurations," *Biomedical Engineering Online,* November 2008. [Online]. Available: http://www.biomedical- engineering-online.com/content/7/1/11.

[15] J. A. Nyenhuis, S.-M. Park, R. Kamondetdacha, A. Amjad, F. G. Shellock, and A. R. Rezai, "MRI and Implanted Medical Devices: Basic Interactions With an Emphasis on Heating," *IEEE Transactions on Device and Materials Reliability*, vol. 5, no. 3, pp. 467-480, September 2005.

[16] E. Neufeld, S. Khn, G. Szekely, and N. Kuster, "Measurement, simula- tion and uncertainty assessment of implant heating during MRI," *Physics in Medicine and Biology*, vol. 54, no. 13, pp. 4151-4169, July 2009.

[17] M. G. Zanchi, R. Venook, J. M. Pauly, and G. C. Scott, "An Optically Coupled System for Quantitative Monitoring of MRI-Induced RF Currents Into Long Conductors," *IEEE Trans. on Medical Imaging*, vol. 29, no. 1, pp. 169-178, January 2010.

[18] S.-M. Park, R. Kamondetdacha, and J. A. Nyenhuis, "Calculation of MRI-Induced Heating of an Implanted Medical Lead Wire With an Electric Field Transfer

Function," *Journal of Magnetic Resonance Imaging*, vol. 26, no. 5, pp. 1278-1285, November 2007.

[19] E.Mattei, M.Triventi, G. Calcagnini, F. Censi, and P. Bartolini, "MRI in Patients with Implanted Devices: A Numerical Model for the Evaluation of Lead Heating," *Computers in Cardiology*, Valencia, Spain, September 2006, vol. 33, pp. 809-812.

[20] J. Nadobny, M. Szimtenings, D. Diehl, E. Stetter, G. Brinker, and P. Wust, "Evaluation of MR-Induced Hot Spots for Different Temporal SAR Modes Using a Time-Dependent Finite Difference Method With Explicit Temperature Gradient Treatment," *IEEE Trans. on Biomedical Engineering*, vol. 54, no. 10, pp. 1837-1850, October 2007.

[21] U. D. Nguyen, J. S. Brown, I. A. Chang, J. Krycia, and M. S. Mirotznik, "Numerical evaluation of heating of the human head due to magnetic resonance imaging," *IEEE Trans. on Biomedical Engineering*, vol. 51, no. 8, pp. 1301-1309, August 2004.

[22] L. Angelone, J. Ahveninen, J. W. Belliveau, and G. Bonmassar, "Analysis of specific absorption rate (SAR) at 3T MRI with variable Deep Brain Stimulation (DBS) lead resistivity," *IEEE Transactions of Medical Imaging*, vol. 29, no. 4, pp. 1029-1038, April 2010.

[23] T. S. Ibrahim, "Ultrahigh-field MRI whole-slice and localized RF field excitations using the same RF transmit array," *IEEE Trans. on Medical Imaging*, vol. 25, no. 10, pp. 1341-1347, October 2006.

[24] E. Mattei, M. Triventi, G. Calcagnini, F. Censi, W. Kainz, H. I. Bassen, and P. Bartolini, "Temperature and SAR measurement errors in the evaluation of metallic linear structures heating during MRI using fluoroptic probes," *Physics in Medicine and Biology*, vol. 52, no. 6, pp. 1633-1646, February 2007.

[25] E. Mattei, G. Calcagnini, F. Censi, M. Triventi, and P. Bartolini, "Numerical model for estimating RF-induced heating on a pacemaker implant during MRI. Experimental validation," *IEEE Trans. on Biomedical Engineering*, vol. 57, no. 8, pp. 2045-2052, August 2010.

[26] T. Sommer, C. Vahlhaus, G. Lauck, A. von Smekal, M. Reinke, U. Hofer, W. Block, F. Trber, C. Schneider, J. Gieseke, W. Jung, and H. Schild, "MR Imaging and cardiac pacemakers: In vitro evaluation and in vivo studies in 51 patients at 0.5 T," *Radiology*, vol. 215, no. 3, pp. 869-879, June 2000.

[27] P. Vernickel, V. Schulz, S. Weiss, and B. Gleich, "A safe transmission line for MRI," *IEEE Trans. on Biomedical Engineering*, vol. 52, no. 6, pp. 1094-1102, June 2005.

[28] C. J. Yeung, R. C. Susil, and E. Atalar, "RF safety of wires in inter- ventional MRI: Using a safety index," *Magnetic Resonance in Medicine*, vol. 47, no. 1, pp. 187-193, January 2002.

[29] A. Christ, W. Kainz, E. G. Hahn, K. Honegger, M. Zefferer, E. Neufeld, W. Rascher, R. Janka, W. Bautz, J. Chen, B. Kiefer, P. Schmitt, H.-P. Hollenbach, J. Shen, M. Oberle, D. Szczerba, A. Kam, J. W. Guag, and N. Kuster, "The Virtual

Familydevelopment of surface-based anatomical models of two adults and two children for dosimetric simulations," *Physics in Medicine and Biology*, vol. 55, no. 2, pp. N23-N38, 2010.

[30] A. Balanis, *Advanced Engineering Electromagnetics*, New York: John Wiley & Sons Inc, 1989.

[31] J.-P. Berenger, "A Huygens Subgridding for the FDTD Method," *IEEE Trans. on Antenna and Propagation*, vol. 54, no. 12, pp. 3797-3804, December 2006.

[32] R. Luechinger, V. A. Zeijlemaker, E. M. Pedersen, P. Mortensen, E. Falk, F. Duru, R. Candinas, and P. Boesiger, "In vivo heating of pacemaker leads during Magnetic Resonance Imaging," *European Heart Journal*, vol. 26, no. 4, pp. 376-383, November 2005.

[33] Pennes HH, "Analysis of tissue and arterial blood temperatures in the resting human forearm," *J Appl Physiol* 1948;1:93-122.

[34] *Standard Test Method for Measurement of Radio Frequency Induced Heating On or Near Passive Implants During Magnetic Resonance Imaging*, ASTM F2182 - 11a.